



Finite Element Model Updating for Material Model Calibration: A Review and Guide to Practice

Bin Chen¹ · Bojan Starman^{2,3} · Miroslav Halilović² · Lars A. Berglund¹ · Sam Coppieters³

Received: 31 July 2024 / Accepted: 17 October 2024
© The Author(s) 2024

Abstract

Finite element model updating (FEMU) is an advanced inverse parameter identification method capable of identifying multiple parameters in a material model through one or a few well-designed material tests. The method has become more mature thanks to the widespread use of full-field measurement techniques, such as digital image correlation. Proper application of FEMU requires extensive expertise. This paper offers a review of FEMU and a guide to practice. It also presents FEMU-DIC, an open-source software package. We conclude by discussing the challenges and opportunities in this field with the intent of inspiring future research.

Abbreviations

FEA	Finite element analysis
FEM	Finite element method
VFM	Virtual field method
DIC	Digital image correlation
IDIC	Integrated DIC
IDVC	Integrated digital volume correlation
2D-DIC	Two-dimensional digital image correlation
Stereo-DIC	Stereo digital image correlation
DVC	Digital volume correlation
FE-DIC	Finite element based global digital image correlation
MF-DIC	Meshfree digital image correlation
PMMA	Polymethylmethacrylate
CEGM	Constitutive equation gap method
CTE	Coefficient of thermal expansion
ROI	Region of interest
POI	Point of interest
PSO	Particle swarm optimization
GA	Genetic algorithm

LM	Levenberg–Marquart
GN	Gauss–Newton
SQP	Sequential Quadratic Programming
BFGS	Broyden–Fletcher–Goldfarb–Shanno
AI	Artificial intelligence
SENB	Single edge-notched beam
CZM	Cohesive zone model
WST	Wedge splitting test
BEM	Boundary element method
NM	Nelder–Mead
NOD	Notch opening displacement
SSD	Sum of square difference
IR	Infrared
SNR	Signal-to-noise ratio
ANN	Artificial neural network
MT	Material testing
FEMU	Finite element model updating
FEMU-F	FEMU that uses force-based cost function
FEMU-FN	FEMU that uses normalized force-based cost function
FEMU-U	FEMU using the cost function based on displacement field
FEMU-UN	FEMU using the cost function based on normalized displacement field
FEMU- ϵ	FEMU using the cost function based on strain field
FEMU- ϵ N	FEMU using the cost function based on normalized strain field
FEMU-UF	FEMU using the weighted cost function that combines displacement field and force information

✉ Bin Chen
binchen@kth.se

¹ Wallenberg Wood Science Center, Department of Fiber and Polymer Technology, KTH Royal Institute of Technology, 10044 Stockholm, Sweden

² Faculty of Mechanical Engineering, University of Ljubljana, Ljubljana, Slovenia

³ Eloo Lab, Department of Materials Engineering, KU Leuven Ghent Campus, Gebroeders De Smetstraat 1, 9000 Ghent, Belgium

FEMU- ϵ F	FEMU using the weighted cost function that combines strain field and force information	Std()	Standard deviation operation
		max()	Find the maximum value
		Mean()	Mean value operation
FEMU-UFN	FEMU using the weighted cost function that combines normalized displacement field and normalized force information	ϵ	Strain
		\mathbf{p}	Unknown material parameter vector
		k	Subscript of the parameter index in parameter vector
FEMU- ϵ FN	FEMU using the weighted cost function that combines normalized strain field and normalized force information	p_k	k -th model parameter
		ω_F	Weight to control the importance of force information in cost function
FEMU-FR	FEMU that uses force-based cost function with parameter regularization term	ω_{f_k}	Weight to control the importance of regularization term f_k in cost function
FEMU-UR	FEMU using the cost function based on displacement field with parameter regularization term	$\lambda_{\min}, \lambda_{\max}$	Smallest and largest eigenvalue of Hessian matrix, respectively
FEMU-FLN	FEMU using the weighted cost function that combines normalized force and normalized crack length information	M	Number of unknown material parameters
		S_k	First-order Sobol index
		S_{Tk}	Total Sobol index
FEMU-FCN	FEMU using the weighted cost function that combines normalized force and normalized notch opening displacement information	N_F	Calculation point number for force
		N_U	Calculation point number for displacement
		N_T	Number of data point for temperature in ROI
FEMU-UT	FEMU using the weighted cost function that combines displacement field and temperature field information	ω_T	Weight to control the importance of temperature information in cost function
		ω_U	Weight to control the importance of displacement information in cost function
FEMU-UFT	FEMU using the weighted cost function that combines displacement field, temperature field, and force information	ξ	Normalization term in the sensitivity matrix
SEM	Scanning electron microscope	ζ_k	Scalar indicator for sensitivity
DT	Digital twin	\mathbf{H}	Hessian matrix
fps	Frame per second	γ_Q	Collinearity of the parameter sensitivity
List of Symbols (from Section 5)		q	Size of a subset of the parameter space
N_S	Number of load steps	$\tilde{\mathbf{J}}_q$	Sensitivity matrix of the subset of the parameter with size of q
t	Subscript indicating load step	S_k	First order Sobol indices
EXP	Superscript denoting data from experimental measurement	S_{Tk}	Total Sobol indices
FEA	Superscript denoting data from numerical simulation	j	Superscript indicating the index of iteration number
NORM	Superscript denoting normalization term	γ	The step size for gradient descent method
F	Reaction force	Δ	Increment of a parameter in optimization
σ_F	Standard deviation of force	∇	Differentiation operator
ω	Weight in the cost function	\mathbf{J}	Jacobian matrix
σ_{NOD}	Standard deviation of DIC-measured displacement	\mathbf{I}	Identity matrix
L	Crack length	λ	Damping factor in LM algorithm
m	Subscript indicating the index of notch opening displacement data	l	Subscript denoting the index of the individual contribution in the cost function
N_L	Number of notch opening displacement data	δ	Machine precision
N_D	Number of strain or displacement data point in ROI	$\Delta \mathbf{p}_k$	All-zero parameter vector with k -th value being a small perturbation
i	Subscript for the point index in ROI	κ	Condition number
u	Displacement	χ	Cost function
		χ_l	Individual contribution in cost function

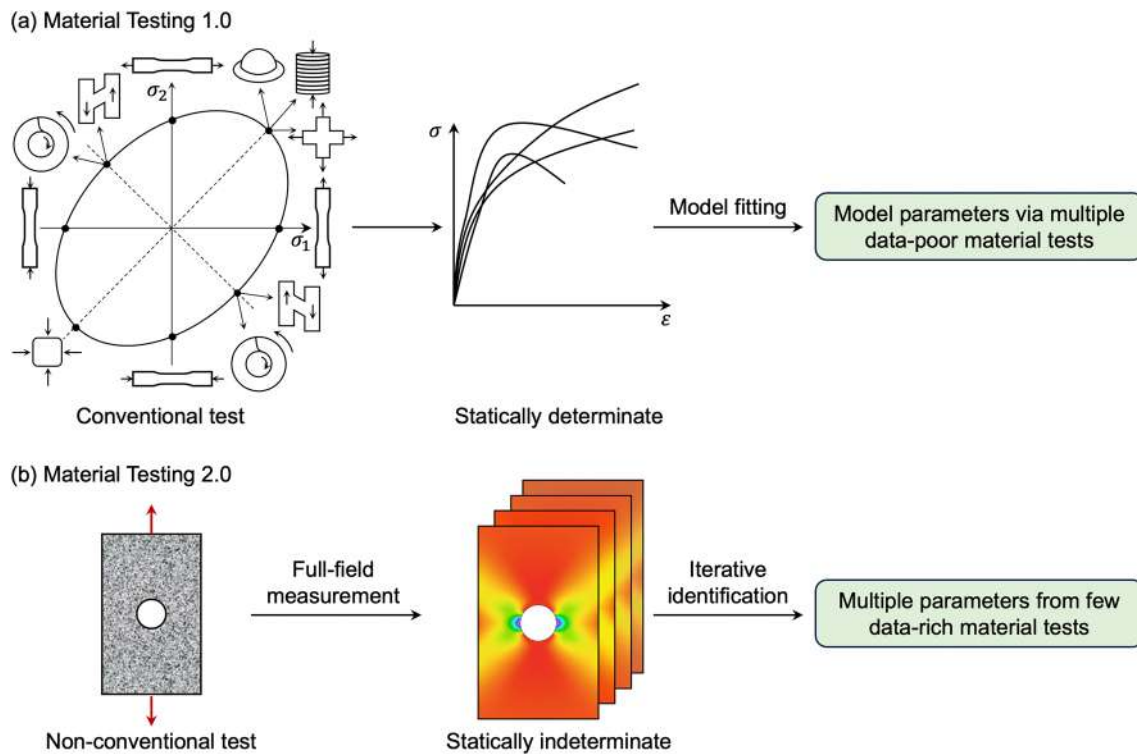


Fig. 1 Comparison between material testing 1.0 and material testing 2.0

V	Variance
E	Expectation

1 Introduction

The possibilities offered by stress analysis through numerical methods [1] have fundamentally changed workflows in engineering design, material development, and mechanics research. The predictive accuracy of engineering simulation is highly dependent on the accuracy of the adopted material model (or constitutive model) [2]. Hence, a major task is to identify parameters in a material model, which can be an elastic, hyperelastic, elasto-plastic, plastic, or fracture material model. The parameters of a material model need to be calibrated against experimental data [3]. The material model calibration is a typical inverse problem in experimental solid mechanics. The calibration process employs an inverse method that involves minimizing of the discrepancy between the experimental data and the analytical/numerical prediction by the material model. Pierron and Grédiac [4] classified the material parameter calibration techniques into 'Material Testing 1.0' (MT1.0) and 'Material Testing 2.0' (MT2.0) based on whether full-field measurement is used.

MT1.0 encompasses the traditional ways to calibrate the material models. Figure 1a illustrates the MT1.0 approach

in the scenario of calibrating an anisotropic yield function to characterize the plastic behavior of sheet metal [5]. MT1.0 generally calibrates the material models without full-field measurement information. It assumes a specific quasi-homogeneous strain and/or stress state in the sample. Thus, the strain can be measured by a strain gauge or an extensometer [6], while the stress state can be directly computed from the experimentally measured load. One or a few material model parameters can be estimated by fitting the material model to the obtained stress–strain curves.

Each MT1.0 test is designed to identify a very limited number of constitutive parameters under specific conditions, such as an uniaxial tensile or simple shear test. In MT1.0, the inverse problems for the calibration of advanced material models are often statically determinate. MT1.0 experiments are straightforward, accurate and standardized. However, multiple tests are required to fully calibrate advanced material models that involve a large number of unknown model parameters. In this regard, MT1.0 is often perceived as the “*poor relative of computational mechanics*” [7].

Although MT1.0 remains extremely important for validating novel theories and material models, MT2.0 [4, 8] is emerging as a key approach in the development of digital tools for efficient material model calibration. MT2.0 is an alternative strategy in which the standard material test is substituted by a single complex experiment, thereby

reducing the extensive experimental demands of MT1.0. It (see Fig. 1b) exposes the material to a variety of stress states simultaneously. Full-field measurement of the heterogeneous physical responses (such as displacement, strain, temperature) offers the possibility to identify all parameters in very few tests. In such scenarios, an iterative inverse method based on full-field measurement information is required. An example of that is the calibration of an advanced plasticity model. In MT1.0, 17 tests at different stress states are needed to accurately calibrate the Yld2000-2d yield function following the state-of-the-art methods [9]. In MT2.0, the same yield function can be calibrated from just two experiments [10] that involve multiple stress states in each well-designed test. Another example is the calibration of heterogeneous materials such as welds [11]. MT1.0 calibrates only an averaged behavior, while MT2.0 can, in principle, identify spatially varied properties through one single test. Currently, MT2.0 methods are confined to research laboratories, for the most part, although further development could lead to their implementation in industry.

Several MT2.0 methods based on heterogeneous kinematic fields have been proposed. The following is a non-exhaustive list of the most successful ones: Finite Element Model Updating (FEMU), Virtual Field Method (VFM) [7, 12, 13], Constitutive Equation Gap Method (CEGM) [14], equilibrium gap method [15] and modified constitutive relation error method [16, 17]. Numerous studies [18–20] have explored and analyzed these methods in detail. The present review focuses only on FEMU due to its comparably straightforward implementation, high versatility, and the widely available finite element analysis (FEA) software.

FEMU is a parameter identification method that iteratively updates the material parameters in a finite element model by minimizing the discrepancy between experimental measurement and numerical simulation. Figure 2 shows an overview of a basic FEMU framework. The process starts by conducting a complex mechanical experiment in a laboratory. The physical responses of the specimen, such as strain and temperature fields, are measured during the test. Afterwards, the same test is numerically simulated

Fig. 2 Principle of classical FEMU

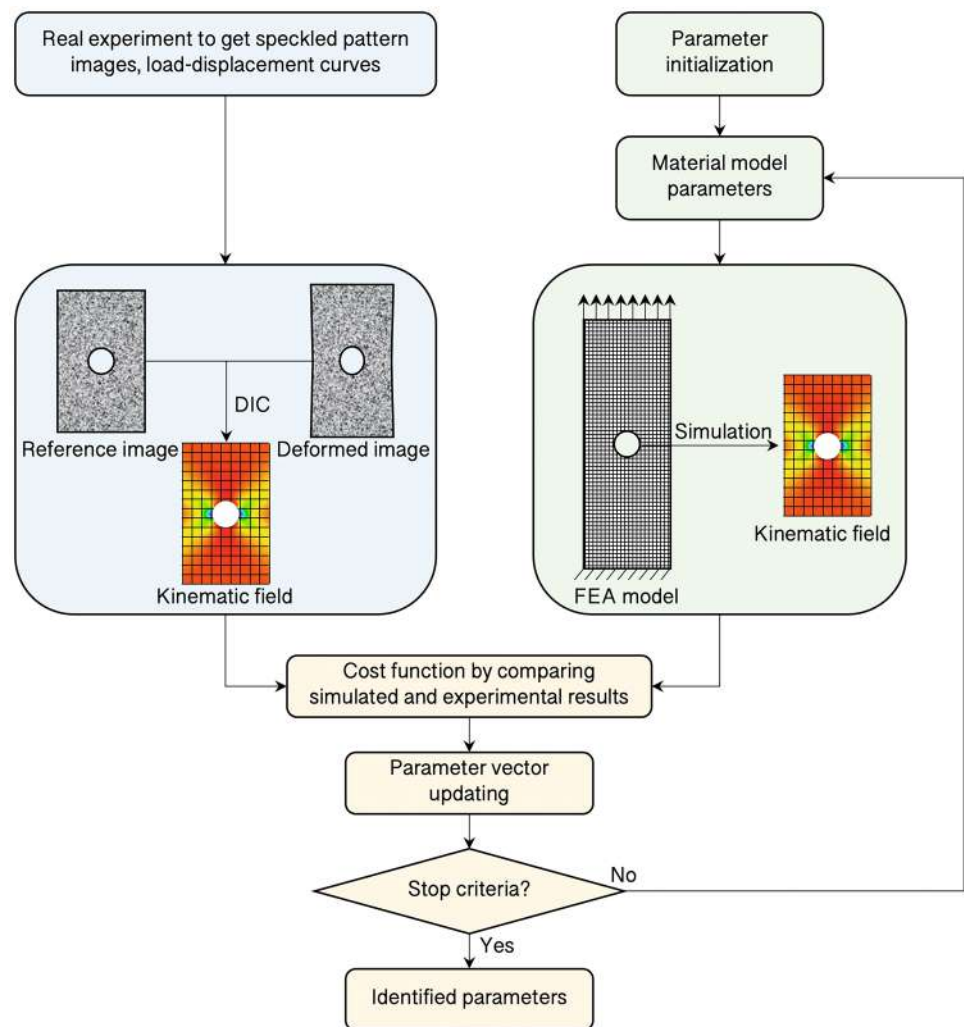
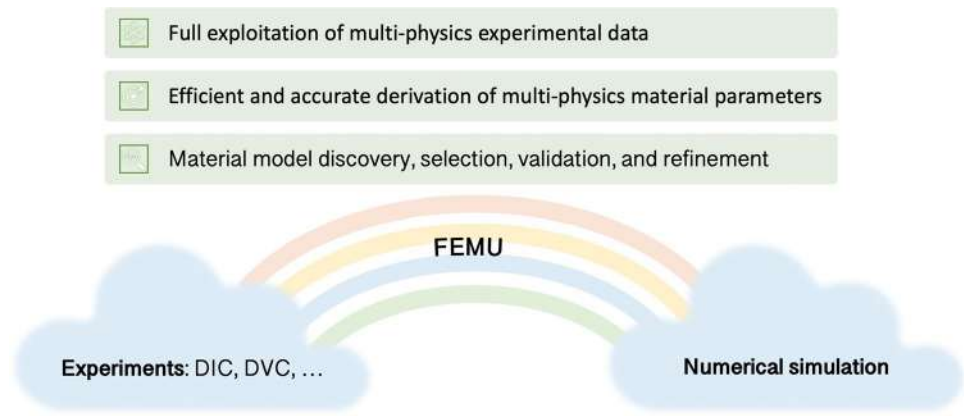


Fig. 3 FEMU bridging experiments and numerical simulation

using a suitable material model and initial material model parameters. The material model parameters in the numerical simulation are optimized by iteratively minimizing the discrepancy between the experimentally measured physical responses and their simulated counterparts. FEMU is primarily used to identify in-plane material parameters from thin samples by assuming plane stress condition. It is also applicable to identify 3D material properties if rich out-of-plane or 3D internal strain field information is available. Such displacement or strain information could be obtained by multi-view digital image correlation (DIC) or digital volume correlation (DVC).

FEMU is widely used in several research areas, such as geotechnical engineering, structural applications, and constitutive material parameters identification. In geotechnical engineering, FEMU has been used widely but without using the same terminology [21–26]. The geomaterial parameters are calibrated by minimizing the difference between the experimental and simulated value of stresses, strains, void ratio, excess pore pressure, etc. In structural applications [27], FEMU identifies the structural parameters using the physical responses such as natural frequencies [28–30], mode shapes [31], displacements [32], strains [33]. In such areas, FEMU generally identifies the parameters of materials or structures without using full-field measurement information [34]. This review focuses primarily on FEMU using full-field physical responses in the scenario of constitutive material parameters identification.

FEMU can function as a bridge between numerical simulation and experiments (Fig. 3). Deep integration of experiments and simulation is one of the goals in solid mechanics community. FEMU can contribute primarily in the following three aspects by making full use of the ability from experiments and numerical simulation.

- Full exploitation of multi-physics experimental data: heterogeneous physical responses, such as strain fields and temperature fields, offer an abundance of experimental data. By fully exploiting the rich data in FEMU

we improve the capability and reliability in calibrating multiple parameters in a given material model.

- Efficient and accurate derivation of multi-physics material parameters: FEMU can efficiently and accurately identify material parameters in diverse physical models, such as elastic, plastic and thermomechanical models. The material model could be both a physical model and a phenomenological material model. Here, the efficiency refers to the reduction in the amount of experimental measurements required.
- Material model discovery [35], selection [2, 36], and validation [37]: we can evaluate the difference between the experiments and the simulated responses based on the identified parameters. This difference helps us assessing the selected model and therefore discover, select and validate material models.

1.1 Application Scope of FEMU

This review starts with an overview of the range of applications, scenarios, or areas where FEMU can be effectively applied. We conducted a comprehensive review focusing on the application of FEMU across several material families, including metals, composites, polymers, biomaterials and ceramics. The associated material models are primarily divided into plasticity, elasticity, hyperelasticity, viscoelasticity and fracture. The other material models have been excluded from the analysis due to being sparsely represented in the current FEMU studies. We collected around 200 FEMU publications and found that in more than 100 of them, the material families and the material models adopted are clearly reported. We reviewed these publications and compiled statistics on the problems investigated using FEMU. Figure 4 presents the publication ratio (the number of publications in a category divided by the total number of publications) with respect to different materials and mechanical properties.

Metals, such as steel [38–46], nodular graphite cast iron [47], aluminum and its alloys [36, 48, 49] and titanium

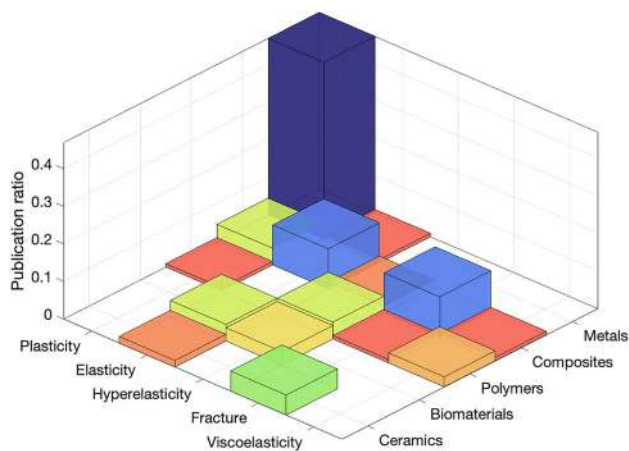


Fig. 4 Publication ratio of different materials and problems studied by FEMU, a statistical result from 113 papers. Publication ratio is the number of publications in one category divided by the total number of publications

[50], account for almost half of the materials studied using FEMU. This can probably be attributed to the widespread use of metals in engineering design. They are predominantly modelled using phenomenological material models that are widely available in commercial FEA solvers. For metals, FEMU focuses primarily on the identification of the plastic material behavior. The reason is that these plastic properties are described by complex material models with multiple parameters. This task is very suitable for FEMU while being highly experimentally intensive for MT1.0. Additionally, plastic deformation typically leads to large strains, which yields a favorable signal-to-noise ratio in DIC measurements.

Composite materials, such as carbon/epoxy composite [51], 3D woven composite [52], glass/epoxy laminate [53–55], concrete [56, 57], transparent wood [58] and allignocellulose composites [59], are the second most studied materials for FEMU. Their behavior is mostly orthotropic elastic, and their failure is less governed by plastic deformation. The interest is therefore in the identification of the four orthotropic elastic parameters and some fracture model parameters. In the case of polymers, FEMU is primarily used to investigate the behaviors of hyperelasticity and viscoelasticity, with notable studies conducted on materials like high impact polystyrene [60], polymethylmethacrylate (PMMA) [61], and rubber [62–64]. In biomaterials (biological materials), such as human skin [65], muscle [66, 67] and wood [68, 69], the most common mechanics descriptions are elasticity and hyperelasticity. Ceramics [70–72] are generally brittle, and thus the fracture properties are of fundamental importance.

Figure 5 shows the evolution in the number of publications from 2006 to 2022. Metallic materials and their plastic behavior are the main focus of FEMU applications. However, the identification of orthotropic elastic, hyperelastic, and fracture properties in advanced composites, biomaterials, ceramics, and polymers is gaining in significance.

1.2 Historical Context of FEMU

To the best of the authors' knowledge, the FEMU approach for identifying the material model parameters can be traced back to 1971 [73]. It has since seen half a century of development and use. This section will review the significant milestones in the development of FEMU, see Fig. 6,

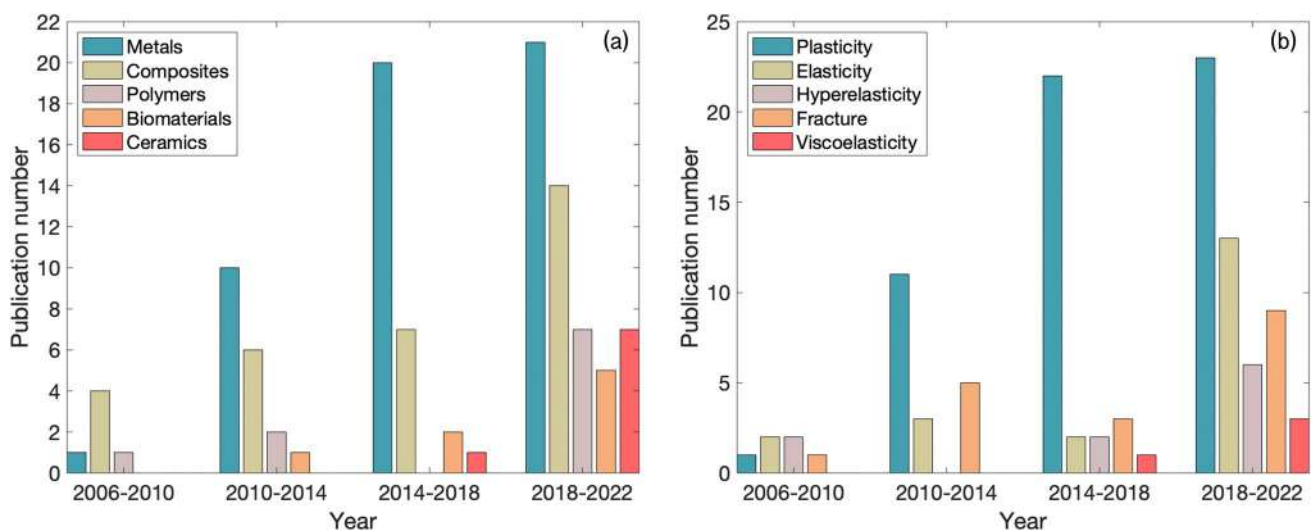


Fig. 5 Evolution in the number of publications on **a** different materials and **b** problems being investigated using FEMU between 2006 and 2022, a statistical result from over 100 papers

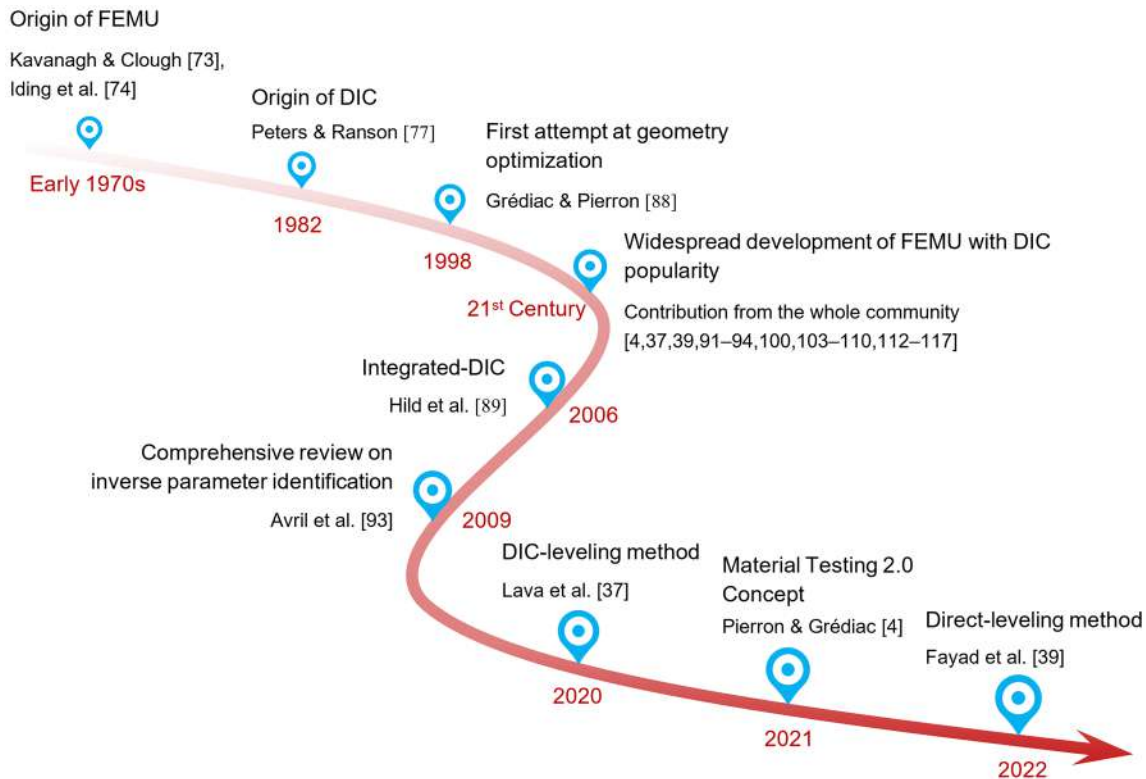


Fig. 6 Milestones in FEMU development history

serving as a brief historical perspective on the evolution of the technique.

In the pioneering work by Kavanagh and Clough in 1971 [73], they inversely identified the mechanical properties of elastic solids using a FEMU approach, though the terminology FEMU was not used in their work. Iding et al. [74] identified the parameters in the stress constitutive function of nonlinear elastic solids using FEMU in 1994. Due to the difficulty of measuring full-field physical response, FEMU remained a niche research area until the 1990s [75, 76].

In the early 1980s, Peters, Ranson, Sutton and others at the University of South Carolina [77–81] laid the foundational groundwork for Digital Image Correlation (DIC). DIC [77, 82, 83] together with other full-field measurement techniques such as Moiré Interferometry [84] and the grid method [85], have developed rapidly in the last decades. These full-field measurement techniques, especially DIC, began to be used widely in the 21st Century. The popularity of these full-field measurement techniques has greatly promoted the spread of FEMU. The earliest FEMU approaches using full-field kinematic data were reported by Mahnken and Stein [86] in 1996 and Meuwissen et al. in 1998 [87].

Sample design is one of the core topics in FEMU. Grédiac and Pierron [88] are the pioneers in optimizing specimen geometry to enhance the accuracy of parameter identification. Their primary focus was to develop the VFM. However,

their research is also important within the context of FEMU, since specimen design is a fundamental building block for both methods. Their contribution highlighted the importance of geometry design for accurate parameter identification in MT2.0.

Several researchers have aimed to improve the fundamental FEMU strategies. In 2006, Hild et al. [89, 90] proposed the first paper on Integrated-DIC (IDIC). IDIC provided a different perspective on FEMU by deeply integrating the full-field DIC measurement with FEMU. Such an endeavor represents an innovation in the fundamental FEMU strategy. Wide application of IDIC [91] demonstrated the importance of developing FEMU through fundamental strategy refinement. Lava et al. [37] proposed the DIC-leveling method in 2020, based on their work of creating synthetically deformed images [92] in 2009. Fayad et al. proposed the direct leveling method [39] very recently. These strategies mitigate the errors due to the difference in calculation method between FEA and DIC.

Numerous reviews have contributed to understanding FEMU from different perspectives. In 2008, Avril et al. [93] published an overview of inverse mechanical parameter identification methods based on full-field measurements. In 2009, Lecompte et al. [94] made the first thorough comparison between the FEMU approach and the standard testing approach for the calibration of an anisotropic yield function.

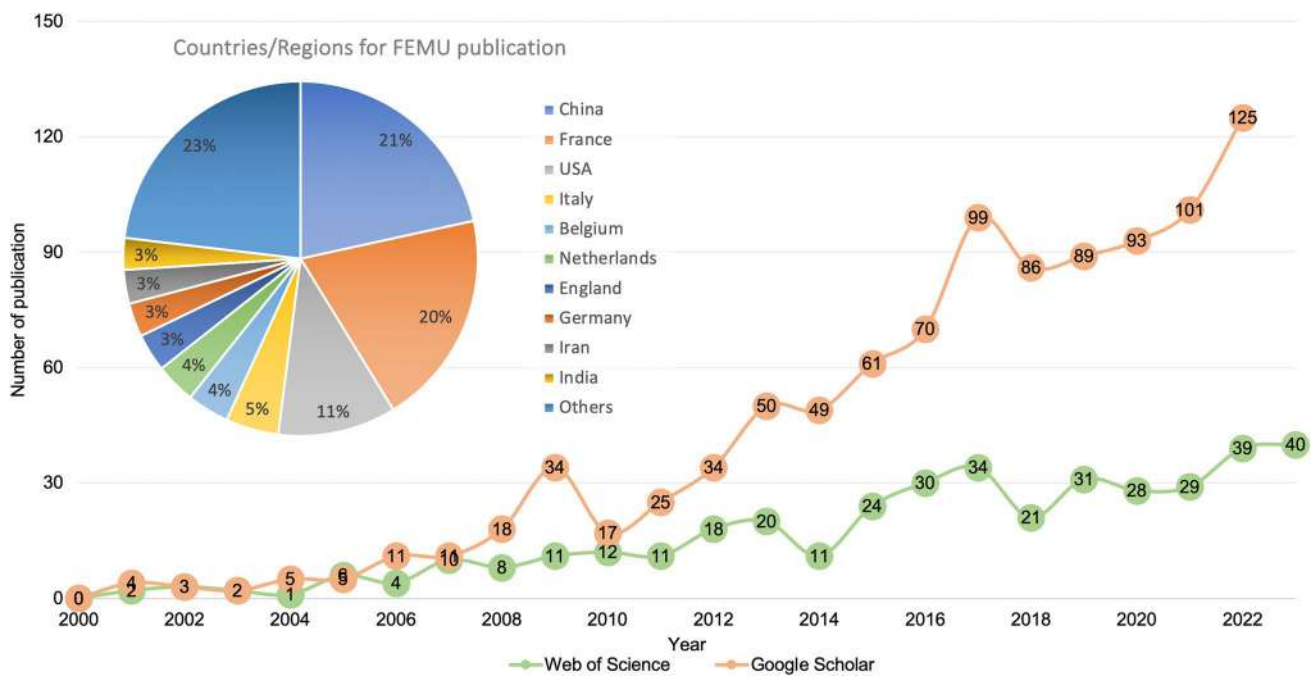


Fig. 7 Number and countries of publications for FEMU studies in constitutive parameters identification. The data is from searches using conservative key words

Markiewicz et al. [95], Hild et al. [96], and Prates et al. [97] have also reviewed major inverse identification methods based on full-field measurements. Pierron and Grédiac [4] focused on test design advancements in Material Testing 2.0. Bruno [98] examined various optical methods and inverse identification approaches for mechanical characterization of composite materials. Neggers et al. [99] reviewed the advance of DIC and FEMU, and discussed the gains and challenges related to the big data in these techniques. Mahnken [100] published a review paper on the inverse identification of constitutive equations. Markiewicz et al. [95] overviewed the calibration of constitutive behaviour and damage models using the normalized direct approach, FEMU and VFM. Andrade-Campos et al. [101] reviewed the inverse method in metal forming. Very recently, Römer [102] provided a holistic view to highlight the connections between the different inverse methods.

Several other important works also contributed to FEMU in different aspects. In 2012, Güner et al. [103] published the first FEMU paper applying the method to the Yld2000-2d yield function [104] and reported on the non-uniqueness problem. Rose and Menzel [105] reported the first FEMU study using kinematic and thermal fields. Also of interest are the progress on topology optimization for specimen design [106], identifiability analysis [107–109], and non-deterministic [110] and hybrid FEMU approaches [111]. Around the same period, several PhD studies [112–114] were directed towards the development of FEMU strategies. PhD studies on uncertainty

quantification [115], specimen design [116], multi-view DIC FEMU [117], etc. were conducted in the following years. The concept of Material Testing 2.0 [8], proposed by Pierron and Grédiac in 2021 [4], described the value of full-field heterogeneous information for inverse parameter identification.

Figure 7 shows the increase in the number of publications on the topic of using FEMU for material model parameter identification. The publication counts are obtained from Google Scholar¹ and Web of Science² starting from the year 2000. The keywords³ are selected so as to exclude literature on structural dynamics and damage monitoring. The keywords cannot cover all literature in this topic since additional

¹ https://scholar.google.com/scholar?q=%22finite+element+model+updating%22+OR+%22finite+element+updating%22+OR+%22FEM+updating%22+OR+%22integrated+digital+image+correlation%22+-%22health+monitoring%22+-%22damage+detection%22+-%22vibration%22+-%22dynamic%22+-%22dynamics%22&hl=en&as_sdt=0%2C5&as_vis=1&as_ylo=&as_yhi=

² <https://www.webofscience.com/wos/woscc/summary/528f28f0-812e-4b1a-9dc8-9bd9d538e80e-9e3169ab/relevance/1>.

³ For Web of Science, the keywords are {ALL=("finite element model updating" OR "finite element updating" OR "FEM updating" OR "integrated digital image correlation") NOT ALL=("health monitoring" OR "damage detection" OR "vibration" OR "dynamic" OR "dynamics")}. For Google Scholar, the keywords are {"finite element model updating" OR "finite element updating" OR "FEM updating" OR "integrated digital image correlation" -"health monitoring" -"damage detection" -"vibration" -"dynamic" -"dynamics"}. The statistics are updated to May 30, 2024.

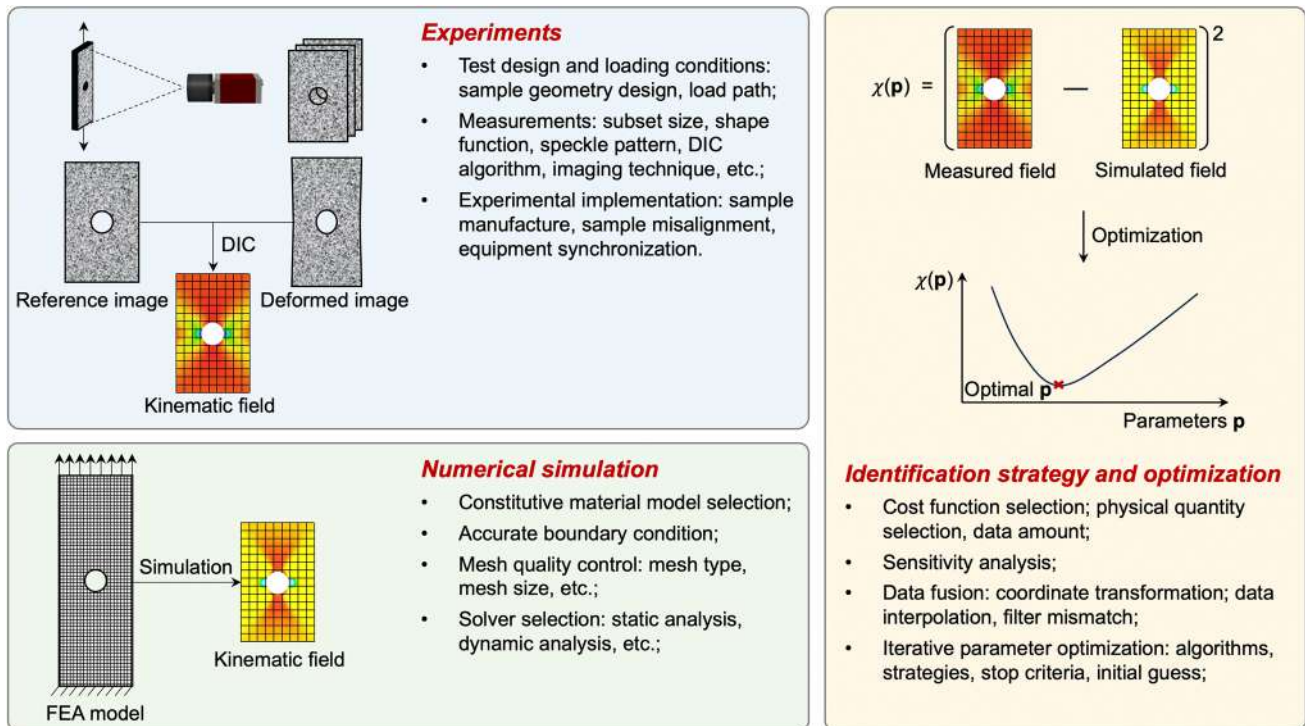


Fig. 8 Three pillars of FEMU. The kinematic fields measured by DIC are supposed to be the inputs

terms, such as inverse identification, may also be related to FEMU. The countries (according to Web of Science) with most contributions to FEMU include China, France and USA—see the inset in Fig. 7. In addition to research papers, the release of user-friendly open-source software [118–120] can reduce the barrier of entry for new practitioners in the field of FEMU.

1.3 Three Pillars of FEMU and Their Implementation Challenges

The basic principle of FEMU is intuitive, as inferred from Fig. 2. FEMU involves three primary pillars (Fig. 8): experiments, numerical simulation, and identification strategies and optimization methods. The technical implementation of a robust FEMU method involves multiple distinct steps in each of these three pillars. The steps, while straightforward, can be implemented in various ways. Given the long and complex characterization chain, the performance of FEMU depends on the effectiveness of each step in the process. Before defining the objectives of this paper, we analyzed the key implementation steps and the associated implementation challenges in this section.

1.3.1 Experiments

- *Test design and loading conditions:* FEMU relies on a sufficiently data-rich experiment. The specimen shape and loading conditions need to be designed in such a way that the material behavior sought rises above the noise floor of the adopted measurement system. For instance, robustly identifying the shear modulus of an orthotropic material requires inducing substantial shear stress states in the tested sample. By carefully designing the sample geometry, we can better activate the shear stress. With FEMU strategies having attained a state of maturity, test design for MT2.0 has emerged as one of the primary bottlenecks [4].
- *Measurement techniques:* The experimental data is the input of FEMU. It is a critical aspect affecting the accuracy and reliability of the outputs, which, in FEMU, are the identified parameters. The effectiveness of FEMU is heavily dependent on the appropriate and skillful application of measurement techniques. Initiatives such as the International Digital Image Correlation society's (iDICs) good practices guide for DIC [121] are making a significant and positive impact on the advancement of MT2.0.
- *Experimental implementation:* The test must be executed with high precision. It is essential that the manufacturing of the sample is exact and closely mirrors its numerical counterpart. The fixtures for the sample should be stable

[122] and aligned. Accurate synchronization between the test machine and the measurement instrument(s) is required. The experimental setup should be designed to facilitate the understanding and extraction of boundary conditions. Experimental implementation are crucial in minimizing both systematic and random errors.

1.3.2 Numerical Simulation

- *Material model selection*: A properly selected material model is a prerequisite for the use of FEMU. Proper selection of the material model is a challenging task highly relying on expertise. Identifying the isotropic elastic model parameters of an orthotropic elastic material, for instance, is not meaningful. Simultaneously identifying multiple parameters in some complex material models using FEMU can be challenging. It might be difficult to guarantee a low uncertainty level and uniqueness for the parameters in a complex model. Such difficulty requires low coupling among the material parameters. Decoupling the experimental and modelling errors in FEMU is also notably challenging.
- *Accurate boundary conditions*: The boundary conditions used in the FE model represent a crucial aspect of FEMU. Correctly imposing these boundary conditions is a challenging part of setting up a reliable FEMU procedure. Seemingly correct assumptions on boundary condition can often lead to significant systematic errors. For example, accurately modeling the load transfer between specimen and grips is very difficult.
- *Computational efficiency*: FEMU iteratively determines the most appropriate material parameters and can thus be computationally demanding. The primary computational bottleneck is the FEA, which is used repeatedly to generate the physical responses. It is therefore crucial to develop an efficient FE model that maintains the accuracy of the simulation. This demands good practice in FE modelling skills, including effective meshing and choosing the most efficient solution procedure for the given problem. In addition to setting up the FE model, the computational effort in FEMU comes also from reading results from the simulation, modifying material parameters, and launching new simulations.

1.3.3 Identification Strategies and Optimization Methods

- *Cost function construction*: The cost function, also known as objective function, loss function, or error function, has a significant impact on the FEMU process. Identifiability problems often arise when the cost function lacks sensitivity to the desired material model parameters. Typically, the cost function is constructed by integrating the differences between numerical simula-

tions and experimental data, which may include various physical responses such as displacement fields, strain fields, thermal fields, forces, etc. It is essential to properly combine the data in the cost function in a way that, for instance, neutralizes the impact of the magnitude of the used physical quantities.

- *Sensitivity analysis*: Sensitivity analysis is a critical but frequently overlooked step in FEMU. It aims to evaluate the sensitivity of the loss function with respect to each parameter. This step can help predict identifiability prior to testing and assess the identification results after the tests, as well as contribute to a better identification by evaluating and optimizing the cost function and test design. In principle, FEMU can run without this step, but the identified parameters may have high uncertainty as a result.
- *Data fusion*: The data points used in the cost function necessitate consistent handling. A primary task in the implementation is identifying corresponding data points in the experimental and numerical datasets [123]. This often involves interpolating data from one set to the other. In addition to matching data points, experimental data frequently needs smoothing to eliminate noise before physical quantities, such as strain fields, are calculated. Calculating the strain field from displacement data, for example, requires a specific numerical procedure. This involves choosing an appropriate strain tensor and applying a consistent process to both the numerical and experimental data, ensuring the resulting strain fields are comparable.
- *Iterative parameter optimization*: FEMU entails solving an optimization problem to find the global optimal solution for a set of constitutive material parameters. This optimization problem is in most cases highly non-convex, with potentially multiple local optima. The gradient-based optimization methods generally converge fast but require a good initial guess for the constitutive parameters. The derivative-free-based methods are more reliable to find global optima but have much lower efficiency. An effective algorithm should offer a large convergence radius to circumvent local optima, while also providing rapid convergence to ensure efficiency. The initial guess of material parameters should therefore be well-informed, or 'educated.' Additionally, the choice of convergence criteria and optimization strategy is crucial.

In addition to these three pillars, uncertainty quantification of FEMU is also critical. FEMU typically yields material model parameters derived from processing a specific experimental dataset. However, calculating the confidence intervals of these identified parameters is not part of the standard output of the FEMU process. Repeating experiments and identifications can provide insights into

uncertainty, but this significantly increases the experimental workload. Research is necessary to establish a standard procedure for determining uncertainty in FEMU.

1.4 Objectives

FEMU faces challenges in computational efficiency, uncertainty quantification, and overall robustness, despite its potential in the calibration of various material models with limited number of tests. While the basic concept of FEMU is straightforward, good practice requires a certain level of expertise to handle these challenges. The implementation steps (Fig. 8) of FEMU are far more involved than in MT1.0, which results in a highly user dependent performance. A notable obstacle to its broader adoption is the lack of education in the use of FEMU.

This paper aims to fill this gap by offering a thorough overview of the crucial components of FEMU and a clear guide on implementation practices, as well as by presenting FEMU-DIC,⁴ the first open-source code that integrates FEMU and DIC. Additionally, it outlines future research directions, encouraging further exploration and enhancement of FEMU in tackling emerging challenges in solid mechanics. Our target audience includes researchers and engineers in experimental solid mechanics and engineering simulation professionals engaged in material model calibration.

2 FEMU Frameworks

The fundamental part of this technique is the FEMU framework. Various FEMU frameworks provide different perspectives on the technique, leading to multiple branches of FEMU. This review mainly discusses three FEMU frameworks (see Table 1): the classical FEMU method, leveling-based FEMU and Integrated DIC. The different FEMU frameworks have unique features in terms of efficiency, accuracy and simplicity.

2.1 Classical FEMU Method

Classical FEMU [120] (see Fig. 2) is the most widely adopted FEMU strategy, thanks to the intuitive principles. In the classical FEMU method, the test is carefully designed in terms of both sample geometry and loading path. The test design guidelines strive to ensure that rich full-field heterogeneous kinematic data can be extracted from the sample surface. The kinematic fields on the sample surface are then measured through DIC. This involves applying a random speckle pattern [124] to the surface of the manufactured sample. A set of images of the sample surface before and

during loading process are captured with one or more cameras. Processing the image sets with a DIC algorithm yields the heterogeneous kinematic fields on the sample surface.

The mechanical test is then numerically simulated using FEA. The sample geometry must match that of the real test; it is therefore advisable to verify the manufacturing accuracy. The boundary condition can be obtained either from the load cell or from the displacement maps measured by DIC. A material model is selected based on user experience that is capable of adequately describing the behavior of the examined material. Initial guesses of the unknown parameters are provided for the material model. The kinematic fields of the sample are computed using FEA based on these initial material model parameters.

A cost function is constructed as the sum of square differences (SSD) between the numerically calculated kinematic fields and the experimentally measured counterparts. If the given model parameters yield a significant discrepancy between the simulated and measured kinematic fields, the cost function value is relatively large. Using an optimization algorithm, the material model parameters in the numerical simulation can be updated by iteratively minimizing the cost function. When the simulation results are sufficiently close to the real test results, the updated parameters in the numerical simulation can serve as the desired material model parameters of the examined material.

The major advantage of classical FEMU is its conceptual simplicity. There are, however, some sources of potentially significant errors. One of the main concerns is the potential inconsistency in the kinematic field calculation between DIC and FEA. The inconsistencies includes the shape function difference, subset filter effect in DIC, strain calculation method difference, strain filter window size deviation, data point misalignment between FEA and DIC, etc. These inconsistencies lead to different degrees of smoothness on the kinematic fields. The errors associated with inconsistencies in the kinematic fields may propagate into the final parameter identification.

2.2 Leveling-Based FEMU

Some ‘leveling-based FEMU’ methods have been proposed to reduce the inconsistency between FEA and DIC, and consequently, improve the identification accuracy. The terminology ‘leveling’ here denotes equalizing some steps in FEA and DIC. This section focuses on two leveling-based FEMU methods: the direct-leveling method and the DIC-leveling method. In the direct-leveling method, the same strain calculation method are applied to the displacement and strain fields in both FEA and DIC. In the DIC-leveling method, virtual speckle pattern images are generated from the simulated displacement fields. The displacement and strain fields can therefore be calculated using the same parameters.

⁴ <https://github.com/BinChenOPEN/FEMU-DIC>.

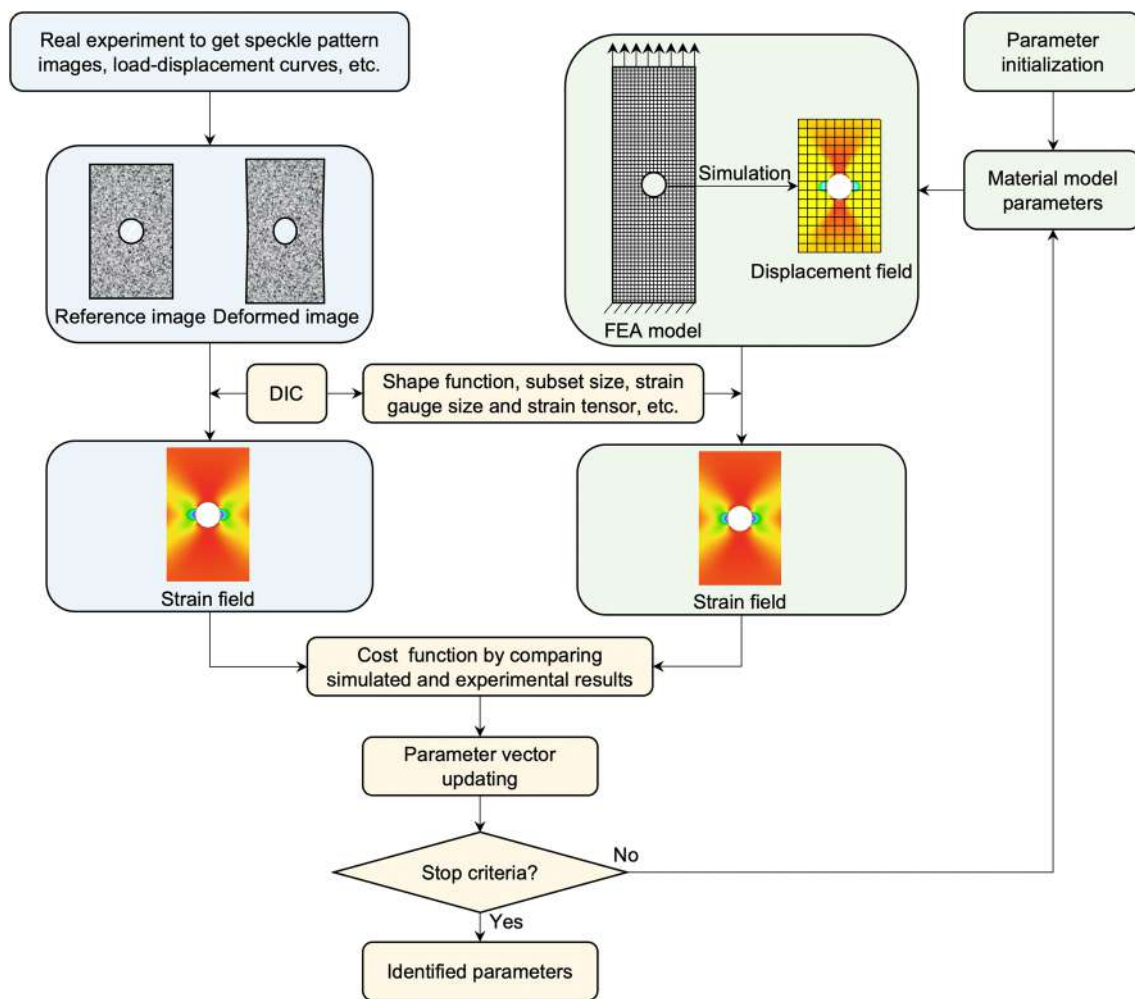


Fig. 9 Direct-leveling FEMU strategy

2.2.1 Direct-Leveling Method

The so-called direct-leveling method (see Fig. 9) is a simple way to minimize inconsistency issues. Denys et al. [41] and later Zhang [125] used the direct-leveling method to eliminate the variation in the strain calculation method (and thus the strain tensor). In their method, the leveling proceeds in two steps: tensor-leveling, and strain-leveling. Tensor-leveling means that the strain tensor is the same in FEA and DIC. Strain-leveling involves calculating the strain using the same method and virtual strain gauge size. The researchers first interpolated the FEA displacement data to the DIC data points, and then used the strain window method [126] to calculate the strain fields. The strain tensor and strain window used for FEA and DIC are the same. The processed strain field from FEA and the strain measured by DIC can then be directly compared for parameter identification.

Fayad et al. [39] proposed to include three steps of leveling: subset-leveling, tensor-leveling, and strain-leveling. In

the additional step of subset-leveling, the displacement fields from FEA are filtered using the same subset size and shape function as used in DIC. However, the subset-leveling on the displacement fields calculated by FEA may not fully match the subset filtering in DIC due to the difference in sampling density. For instance, if the subset can only cover a single calculation point, the subset-leveling cannot be activated in direct-leveling method.

2.2.2 DIC-Leveling Method

The DIC-leveling approach [37, 127] can adequately address most of the issues due to inconsistencies between DIC and FEA results, leading to better identification accuracy. The basic principle is shown in Fig. 10. First, the displacement maps are simulated by FEA using a set of material model parameters as the initial guess. The displacement maps are imposed onto the reference image to generate a set of synthetically deformed images. This is implemented using a

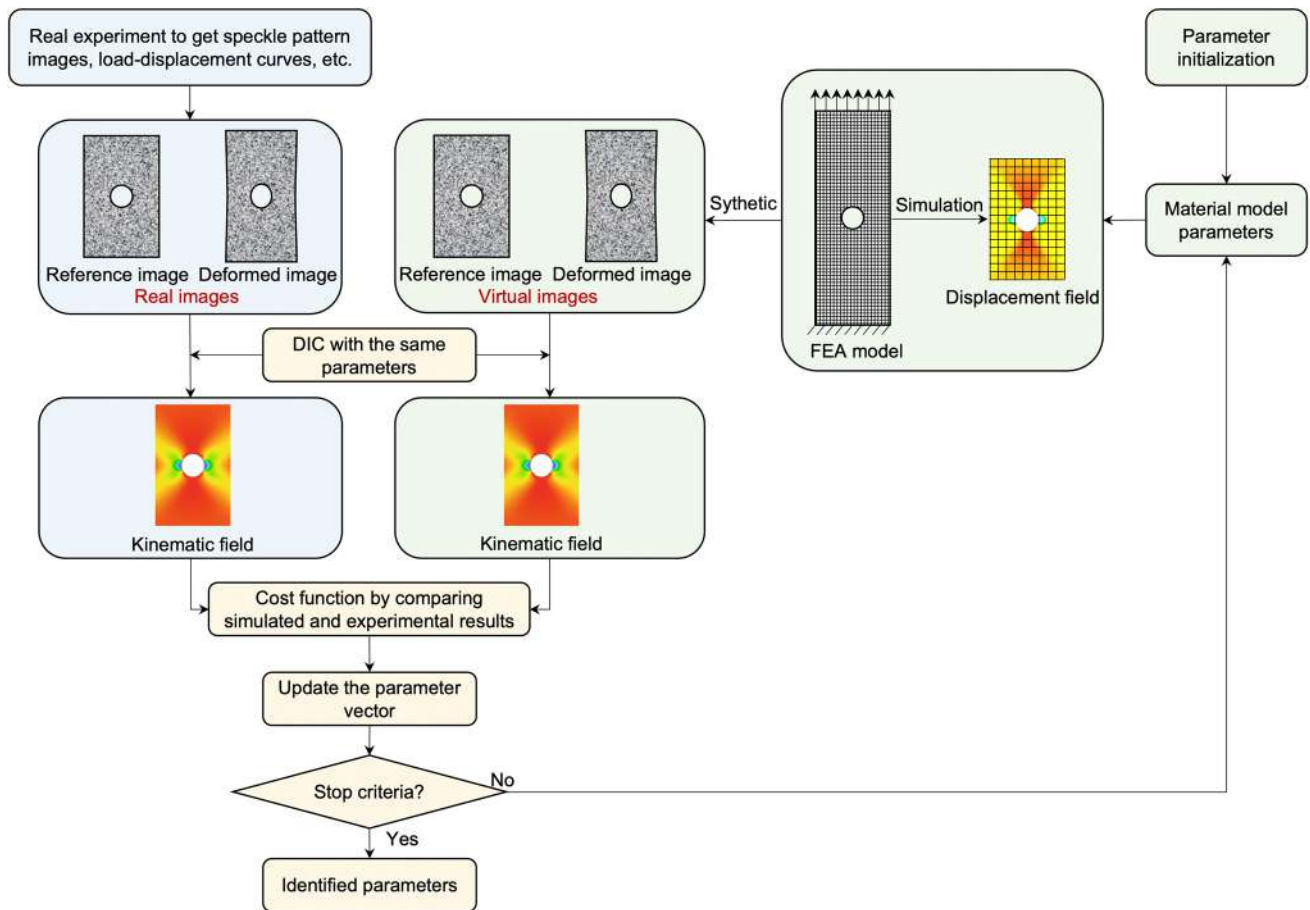


Fig. 10 DIC-leveling FEMU strategy

FEA-based synthetic image deformation procedure [92]. Consequently, two image sets, the virtual image set and the real image set, can be obtained. DIC software then matches the two image sets using the same DIC settings, meaning the same DIC engine and the same user-defined parameters, such as subset size, strain tensor, strain calculation algorithm, shape function, etc. The same region of interest (ROI) and calculation points are selected for the two image sets, naturally satisfying the requirement of the same data point locations and the same strain calculation settings.

By minimizing the error map between the kinematic fields obtained from the virtual and the real image sets, the optimal material model parameters can be iteratively estimated. In this method, a set of virtual images need to be regenerated from the displacement fields calculated by FEA in each iteration. This requires considerable computational resources.

The DIC-leveling method can be traced back to the work of Lava et al. [92]. Their work focuses on systematic errors in DIC for large heterogeneous deformation measurement, not in the context of FEMU. They synthetically generated deformed speckle pattern images using the large

heterogeneous displacement fields calculated from FEA. The displacement fields between the synthetic speckle pattern images were then extracted by DIC and compared with the ground truths from FEA. This unique approach enables us to evaluate the accuracy of the DIC algorithm. The same method was extended to 3D cases by Guildenbecher [128] to compare the results of a numerical simulation to the experimental results for a dynamic problem. The DIC-leveling approach was generalized to FEMU by Lava et al. [37]. It can level the FEA data, so that it preserves the same filtering and spatial resolution as that in the DIC measurement results. This technique has been applied to identify the orthotropic elastic properties of wood [68] and the parameters in Swift's hardening law for a notched specimen design [46].

2.3 Integrated DIC

Integrated DIC (IDIC) [19, 36, 91, 129–134] is an alternative FEMU method. It can be regarded as an extension of the classical FEMU. The method was also meant to improve the identification accuracy. It is proposed based on the basic

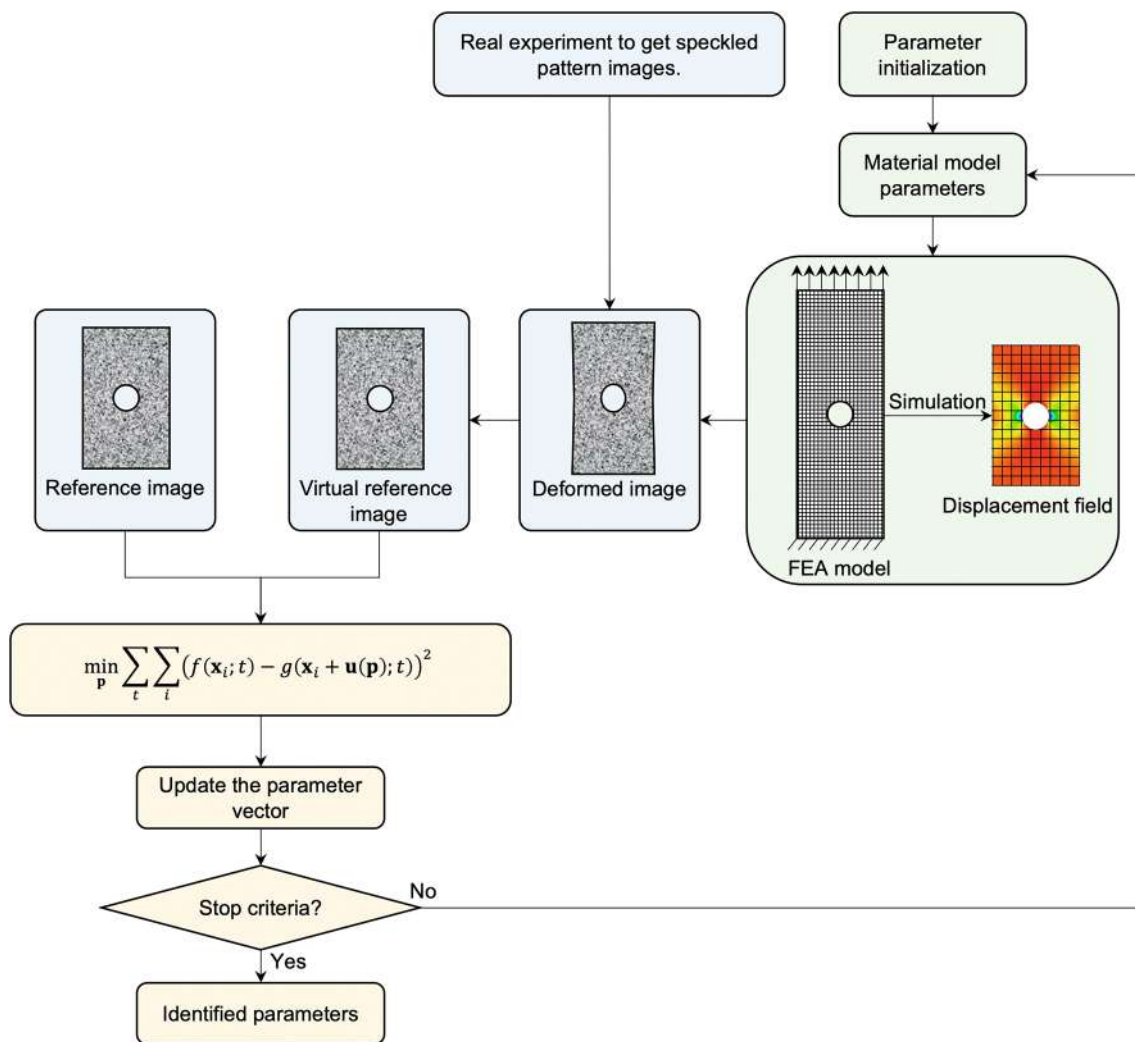


Fig. 11 IDIC strategy

philosophy that the constitutive parameters are of interest instead of the kinematic fields. Once the identification is complete, the kinematic fields are the intermediate data, which are not necessarily measured. IDIC reconciles DIC and FEA by eliminating the step of calculating displacement from the speckle pattern images. In IDIC, the parameters are identified by constructing a cost function directly from the speckle pattern images instead of the kinematic fields (Fig. 11). The displacement maps obtained in FEA are imposed onto the deformed image to generate a virtual reference image. The parameters can be iteratively estimated by minimizing the intensity difference between the virtually generated image and the real image using the cost function below,

$$\chi(\mathbf{p}) = \sum_t \sum_i (f(\mathbf{x}_i; t) - g(\mathbf{x}_i + \mathbf{u}(\mathbf{p}); t))^2 \quad (1)$$

where f and g are the intensity of the reference and deformed image, respectively; $\mathbf{u}(\mathbf{p})$ is the displacement field calculated by FEA with a parameter vector \mathbf{p} ; \mathbf{x}_i is the image coordinate; i and t designate the image pixel index and the load step, respectively. IDIC is a one-step method for identifying all the parameters in a single iterative procedure. The two former methods, by contrast, are two-step approaches that require kinematic field measurement, followed by iterative parameter identification from the kinematic fields.

Direct application of IDIC to identify the elastic–plastic model with only Dirichlet boundary conditions may not be robust. The elastic moduli have a very small influence on the displacement field. External loads should be included in the cost function for more accurate identification, leading to a modified integrated mechanical image correlation [135]. In the cases where large deformations and rotations cause parts of the sample to rotate in or out-of-view, or when the speckle pattern degrades due to large

Table 1 Comparison among different FEMU strategies

FEMU methods	Advantages	Disadvantages
Classical FEMU [120]	Intuitive principle Easy to use with commercial software	Less accurate due to the inconsistency between simulation and experiment Less robust
DIC-leveling method [37, 46, 68, 92, 128]	Accurate, since it partially avoids inconsistency between simulation and experiment	Computationally expensive to generate virtual images in every iteration
Direct-leveling method [39, 107]	Accurate, since it partially avoids inconsistency between simulation and experiment More efficient than DIC-leveling method	Less accurate than the DIC-leveling method
Integrated DIC [19, 36, 91, 129–132]	Robust to image noise Simple implementation One-step procedure to directly estimate the parameters from the speckle pattern images	Sensitive to unexpected rigid-body motion

or complex deformations, IDIC is not applicable anymore. In such cases, the projection images of the contour lines of the test specimens could be used, leading to mechanical shape correlation, a novel IDIC based technique used for parameter identification [136]. Similar to IDIC, Hild et al. [137] proposed an integrated digital volume correlation (IDVC) based on a set of 3D tomography images. To improve the efficiency, Jailin et al. [138] developed an integrated Projection-based DVC. The method is based on Projection-based DVC [139, 140], which works with a few radiographs instead of reconstructed 3D volumes. A similar concept of IDIC has also proven effective for fringe patterns [141]. It involves determining the material model parameters by directly comparing simulated and experimentally measured fringe patterns [141].

IDIC has been adopted to identify orthotropic elastic model [142], elastoplastic model [143], micromechanical constitutive model [144, 145], cohesive zone model [131], phase-field fracture model [146] and residual stress [147, 148]. Except for being used in mechanics, IDIC can also correct the lens distortion in computer vision applications [149–151]. The method uses a known numerical pattern and a picture of the same pattern printed on a plate. The distortion parameters are iteratively estimated by comparing the numerical pattern and the image using IDIC concept. Vermeij and Hoefnagels [152] also adapted the IDIC framework into high-resolution Electron Backscatter Diffraction [153]. Shi et al. used IDIC procedure to determine the crystal orientation and pattern center [154] and elastic strain [155] by comparing experimental and simulated electron diffraction patterns.

A comparative work by Ruybalid et al. [130] shows that the classical FEMU and IDIC are equally robust with respect to poor initial guesses for parameters. Image interpolation has significant effect on both FEMU and IDIC [156]. Under the assumption of small noise level, the weighted FEMU and integrated DIC have the same covariances of the identified parameters [157]. They are also equally sensitive to errors

made in the finite element model. Compared with the classical FEMU methods, IDIC is (i) less sensitive to image noise, (ii) less laborious, and (iii) more reliable due to the fewer sources of potential error. These advantages are especially pronounced in tests with small displacements, large amounts of image noise, specimen misalignment with the loading direction, and/or complex kinematics [130]. However, IDIC is inherently very sensitive to the rigid-body motion of the sample, which can hardly be avoided in real-world experiments. A comparison of different FEMU strategies is shown in Table 1.

3 Material Models

In FEMU, the material model selected should be a good match for the experimental results. At the same time, it should also be concise (have a limited number of unknown material model parameters) to ensure simplicity and improved identifiability. Numerous material models, such as elastic, hyperelastic, plastic, fracture and thermomechanical models have been proposed to describe the mechanical properties or, more generally, behaviors of different materials.

Here, we briefly review some typical material models that are most widespread in the FEMU community. However, we are not aiming to cover the extensive material models, such as viscoelastic [158], hypoplastic [159] and dynamic [160] models, that have been identified by FEMU. Omissions should not be seen as implying that certain models are less important or impractical. For simplicity, the specimens are supposed to be subjected to plane stress state condition unless otherwise stated. Considering the range of material models covered in this section, it is important to highlight that the symbols employed across various constitutive equations introduced in this chapter are not unique. They are not aligned with the List of Symbols.

Table 2 Reference for isotropic and orthotropic elastic model calibration using FEMU

Reference	Year	Models	Materials	Sample tests
[54]	2007	Orthotropic	Glass epoxy composite	Iosipescu test
[134]	2010	Isotropic	E-glass fiber/vinylester composite	Biaxial tensile test of Cruciform geometries
[65]	2013	Orthotropic	Human skin	In vivo tensile test
[164]	2013	Orthotropic	3D Woven Composite	Three-point bending test
[165]	2018	Orthotropic	Carbon fiber-reinforced plastic	Plate specimen bent under a point load
[51]	2019	Orthotropic	Carbon/epoxy composites	Compression test of an open-hole sample
[53]	2021	Orthotropic	Carbon fiber reinforced polymer composite	Three-point bending test
[59]	2022	Orthotropic	All-lignocellulose composites	Tensile test of strip sample
[68]	2022	Orthotropic	Pinus pinaster wood	Compression tests with on-axis and off-axis specimens
[142]	2023	Orthotropic	Carbon fiber-reinforced polymer	Tension and compression tests of open-hole sample

3.1 Linear Elastic Models

For the sake of simplicity, the elastic models introduced here are mainly linear elastic models. The models include the isotropic and orthotropic elastic models. These models generally permit robust, accurate and efficient identification using FEMU. In some cases, such as holocellulose fiber paper [161], the material may not be homogeneous [107], so a heterogeneous distribution of elastic parameters is more practical and accurate. However, accurate description of the heterogeneous material requires a much larger number of constitutive parameters. Identification of heterogeneous parameter distribution is consequently still a challenging task. A summary of some typical references on the topic of identification of linear elastic models using FEMU is given in Table 2.

3.1.1 Isotropic Elastic Model

The isotropic elastic model is a commonly used material model described by only two independent parameters: the elastic modulus E and Poisson's ratio ν . The constitutive equation is:

$$\begin{bmatrix} \varepsilon_{xx} \\ \varepsilon_{yy} \\ 2\varepsilon_{xy} \end{bmatrix} = \frac{1}{E} \begin{bmatrix} 1 & -\nu & 0 \\ -\nu & 1 & 0 \\ 0 & 0 & 2(1+\nu) \end{bmatrix} \begin{bmatrix} \sigma_{xx} \\ \sigma_{yy} \\ \sigma_{xy} \end{bmatrix} \quad (2)$$

where σ_{xx} , σ_{yy} , and σ_{xy} are the stress components along x and y directions and shear stress, respectively. ε_{xx} , ε_{yy} , and ε_{xy} are the strains along x and y directions and shear strain, respectively.

The two material model parameters can be easily estimated through a classical uniaxial tensile or compression test. In the context of FEMU, the isotropic elastic parameters are rarely the sole targets of calibration [134]. Instead, these parameters are determined as a part of a more complicated

task, such as the identification of elasto-plastic [162] or fracture parameters. This does not mean that calibrating isotropic elastic parameters with FEMU is necessarily overkill. Even in a classical uniaxial tensile test, a perfectly homogeneous strain distribution in the sample is hard to achieve, and FEMU can take any heterogeneity into consideration. FEMU can also track the evolution of isotropic elastic modulus, leading to the identification of damage parameters [163].

3.1.2 Orthotropic Elastic Model

Identification of orthotropic elastic parameters using FEMU [164, 165] is a major task in experimental mechanics. Rolled steels, fiber-reinforced composites [54], wood-based materials (e.g., wood [68], bamboo, and their derivatives [166]), etc., are typical orthotropic materials. The elastic response of these materials is governed by the following orthotropic elastic constitutive equation:

$$\begin{bmatrix} \varepsilon_{xx} \\ \varepsilon_{yy} \\ 2\varepsilon_{xy} \end{bmatrix} = \begin{bmatrix} \frac{1}{E_x} & -\frac{\nu_{yx}}{E_y} & 0 \\ -\frac{\nu_{xy}}{E_x} & \frac{1}{E_y} & 0 \\ 0 & 0 & \frac{1}{G_{xy}} \end{bmatrix} \begin{bmatrix} \sigma_{xx} \\ \sigma_{yy} \\ \sigma_{xy} \end{bmatrix} \quad (3)$$

where E_x , E_y , G_{xy} are the elastic moduli along x and y directions and shear modulus, respectively. ν_{xy} and ν_{yx} are the Poisson's ratio under the constraint of $\frac{\nu_{xy}}{E_x} = \frac{\nu_{yx}}{E_y}$. These parameters can generally be effectively and robustly identified using FEMU.

3.1.3 Elastic Models for Heterogeneous Materials

Most mechanical models are intended to describe homogeneous materials with a uniform distribution of elastic parameters. By contrast, some composites, such as wood [167], bamboo and wood composites [168], have significantly

Table 3 Reference for hyperelastic model calibration using FEMU

Reference	Year	Models	Materials	Sample tests
[64]	2006	Mooney-Rivlin	Silica-filled silicone rubber	Tear test
[66, 67]	2014	Neo-Hookean	Thigh muscles	In-vivo compression tests
[173]	2018	Neo-Hookean	Multi-material silicon members	Uniaxial tensile test
[178]	2019	Neo-Hookean	Silicone rubber material	Indentation
[60]	2020	Mooney-Rivlin	High impact polystyrene	Uniaxial tensile test
[119]	2021	Gent	Caucasian skin	Uniaxial tensile test
[62]	2021	Mooney-Rivlin and Yeoh	Rubber	Equibiaxial tensile test
[118]	2023	Neo-Hookean, Mooney-Rivlin, and Ogden	Human lower limbs	In-vivo macro-indentation

heterogeneous property distribution due to either the intended material design or as a result of the inherent characteristics of the material. The rich heterogeneous strain information measured on the sample surface may enable the identification of the heterogeneous parameter distribution. In this task, the model itself remains simple, but the material model parameters may vary spatially and/or temporally. The simplest way to evaluate the parameter distribution on the sample is to divide the whole specimen into several material zones, with homogeneous material properties within each zone. The elastic parameter distribution [169] has been identified for several heterogeneous materials. Sutton et al. [170] and Andrade-Campos et al. [11] identified the local material behavior variation in the weld region of a metal. Tucci et al. [171] calibrated the plastic model parameters as a function of the distance from the welding centerline.

3.2 Hyperelastic Models

Hyperelastic materials, such as rubbers [62] and some biological tissues, are materials exhibiting significant nonlinearity. For these materials, conducting standard experiments yielding a perfectly homogeneous stress state is a challenge. FEMU has also been extensively applied (a summary of references is given in Table 3) to characterize the hyperelastic properties (see some typical hyperelastic models in Ref. [172]), since FEMU can reduce the errors from non-uniform strain states in strain–stress curves fitting. Three hyperelastic models, the Mooney–Rivlin model [118], the compressible Neo-Hookean hyperelastic model [173] and the Gent hyperelastic model [119], that have seen widespread application of FEMU are briefly reviewed. While some other feasible hyperelastic models, such as the Ogden model [174] and the Yeoh model [175, 176], are not detailed here.

Neo-Hookean hyperelastic model: this model [177] is one of the simplest hyperelastic model. It is expressed as

$$W = C_1(I_1 - 3) \quad (4)$$

where C_1 is the hyperelastic parameters. I_1 is the first principal invariants of the right Cauchy-Green deformation tensor; W denotes the strain energy density. The in-vivo muscle tissues [66, 67], silicone rubber material [178], and multi-material member [173] were modeled using the Neo-Hookean hyperelastic model with their parameters calibrated using FEMU.

Mooney–Rivlin model: it is a phenomenological model. It is more general than Neo-Hookean hyperelastic model by considering additional nonlinearity in material response. The Mooney–Rivlin model has the constitutive equation [172] of

$$W = C_1(I_1 - 3) + C_2(I_2 - 3) \quad (5)$$

where C_1, C_2 are the two unknown model parameters that are the target of calibration; I_1, I_2 are the first and second principal invariants of the right Cauchy-Green deformation tensor. The model and its variations have been employed to describe the hyperelastic behaviour of high impact polystyrene [60], latex membrane [179], silicon-rubber [64] and a human lower limbs [118], with the model parameters being identified by FEMU.

Gent hyperelastic model: it is a phenomenological model proposed by Gent [180]. FEMU is also a good way to calibrate the Gent hyperelastic model [119]. This model [formulated by 2 parameters for a compressible Gent hyperelastic model, see Eq. (6)] [181] has been adopted to describe the hyperelastic properties of skin tissue [119]. This model is more complex than the former two hyperelastic models by capturing the limiting chain extensibility phenomena, which is a characteristic of skin behavior when being stretched [119].

$$W = -\frac{\mu}{2} J_m \ln\left(1 - \frac{I_1 - 3}{J_m}\right) \quad (6)$$

Table 4 Reference for plastic model parameters identification using FEMU

Reference	Year	Models (yielding/hardening)	Materials	Sample tests
[87]	1998	Von Mises and Hill48/Linear	Aluminum A1200	Uniaxial tensile test on an asymmetrically notched sample
[207]	2008	Hill48/Swift	Sheet metal DC06	Biaxial tensile test on a perforated cruciform specimen
[94]	2009	Hill48/Swift	Sheet metal DC06	Biaxial tensile test on a cruciform specimen
[45]	2012	Hill48/Swift	Dual-phase steel DP600	Tensile test on a dog-bone sample
[200]	2012	Hill48/Ludwik	Aluminum 2024-T3	Asymmetrically notched tensile sample
[42]	2014	Hill48/Hockett–Sherby	Sheet steel	Biaxial tensile test on multiple cruciform specimens
[192]	2015	Yld2004-18p/Mixed isotropic-kinematic hardening	DC04 mild steel	Uniaxial and biaxial tension, simple shear, uniaxial tensile tests and bulge test
[38]	2016	Hill48/Swift	Sheet metal DC06	Erichsen bulging test
[143]	2016	Von Mises/linear kinematic	Stainless steel	Biaxial tensile test on a cruciform specimen
[36]	2017	Hill48/Ludwik	Aluminum alloy	Dog-bone tensile sample
[41]	2017	Von Mises/p-model	X70 grade steel	Tensile test on a curved specimen
[44, 204]	2017	Hill48/p-model	High strength steel S690QL	Thick tensile sample perforated on the front and thickness surfaces
[11]	2018	Von Mises/Swift	Welded aluminum blanks	Tensile tests
[198]	2018	Von Mises/p-model	High strength steel S690QL	Tensile test on a thick notched sample
[193]	2019	Yld2004-18p/Voce with linear term	DC04mild steel	Tensile test on a specifically designed butterfly sample
[133]	2019	Hill48/Ludwik	Aluminum Alloy 2219	Dog-bone sample
[187]	2019	Yld2000-2D/Voce	7B04 aluminum alloy sheet	Punch test on a specifically designed sample
[188]	2020	Yld2000-2D/Swift	Aluminum alloy and steel	Tensile test on a group of specifically designed samples
[210]	2021	Hill48/ Bilinear	Aluminum alloy 2124-T851	Tensile test on a dog-bone sample
[107]	2022	Yld2000-2D/Swift	Sheet steel SPCE	Tensile test on a specifically designed notched sample
[186]	2022	Yld2000-2D/Swift	Sheet steel SPCE	Tensile test on a specifically designed notched sample
[46]	2023	Yld2000-2D/Swift	Dual-phase steel DP600	Tensile test on specifically designed interior-notched samples

where μ and J_m are the two unknown material model parameters.

3.3 Plasticity Models

The calibration of multiple-parameter plasticity models is one of the most important objectives in the FEMU community. The phenomenological plasticity models are generally described by two major ingredients: the yield criterion and the hardening law. The yield criterion sets the conditions that the plastic deformation initiates. The hardening law describes how the yield surface evolves as the specimen undergoes plastic deformation. A summary of some publications on the identification of different plasticity models using FEMU is shown in Table 4. More information on the calibration of advanced plasticity models for sheet metals can be found in a review by Rossi [182].

3.3.1 Yield criteria:

Here we succinctly review the identification of two typical yield criteria, the Hill48 yield criterion [183] and the Yld2000-2D yield criterion [104].

Hill48 anisotropic yield criterion is a very typical anisotropic yield criterion, particularly for sheet metal anisotropic behaviour modeling. Under plane stress conditions, it can be written as

$$\sigma_{\text{eq}}^2 = H(\sigma_{11} - \sigma_{22})^2 + F\sigma_{22}^2 + G\sigma_{11}^2 + 2N\sigma_{12}^2 \quad (7)$$

where σ_{eq} refers to the equivalent stress and σ_{ij} is the Cauchy stress tensor component. For simplicity, the strain hardening behavior is generally represented by the true stress–strain curve obtained through an uniaxial tensile test along the rolling direction, leading to the constraint of $G + H = 1$ and thus three independent parameters [18].

Conventionally, the three parameters are calibrated by uniaxial tensile tests of the samples along 0° , 45° and 90° to the rolling direction. With FEMU, they can be estimated from a single test. This model has been applied to calibrate

the plasticity of several materials, e.g., anisotropic steel sheet [9, 38, 184, 185], aluminum alloy [103], etc.

Yld2000-2D yield criterion was proposed by Barlat et al. [104] in 2002. It has the advantage of additionally considering the equibiaxial stress state. The model is formulated as

$$2\sigma_{\text{eq}}^m = \left| X'_1 + X'_2 \right|^m + \left| 2X''_2 + X''_1 \right|^m + \left| 2X''_1 + X''_2 \right|^m \quad (8)$$

where m is a material coefficient (generally set to 6 or 8) based on the metal microstructure (derived from crystal plasticity models). It can also be determined through laborious experimental work [9]. X'_i and X''_i are the eigenvalues of stress tensors \mathbf{X}' and \mathbf{X}'' , which are obtained as

$$\begin{cases} \mathbf{X}' = \mathbf{L}'\boldsymbol{\sigma} \\ \mathbf{X}'' = \mathbf{L}''\boldsymbol{\sigma} \end{cases} \quad (9)$$

where $\boldsymbol{\sigma}$ is the Cauchy stress tensor. The tensors \mathbf{L}' and \mathbf{L}'' are written as

$$\mathbf{L}' = \frac{1}{3} \begin{pmatrix} 2a_1 & -a_1 & 0 \\ -a_2 & 2a_2 & 0 \\ 0 & 0 & 3a_7 \end{pmatrix}, \mathbf{L}'' = \frac{1}{9} \begin{pmatrix} -2a_3 + 2a_4 + 8a_5 - 2a_6 & a_3 - 4a_4 - 4a_5 + 4a_6 & 0 \\ 4a_3 - 4a_4 - 4a_5 + a_6 & -2a_3 + 8a_4 + 2a_5 - 2a_6 & 0 \\ 0 & 0 & 9a_8 \end{pmatrix} \quad (10)$$

This model has 8 independent parameters a_{1-8} that need to be calibrated. This yield criterion has proven to be a competitive alternative to the Hill48 criterion for calibrating the plastic property of anisotropic metals [107, 162, 186–188].

Some other criteria, such as the Bron and Besson yield function [189] and the non-quadrat Yld2004-18p yield criterion [190–193], to name just a few, are also feasible and identified with FEMU. For clarity purposes, they are not detailed here.

3.3.1.1 Hardening Laws Three typical hardening laws are briefly introduced here. They are the Swift's hardening law [194, 195] and Voce's hardening rule [196, 197] for small hardening, and the p-model hardening law [198] that combines the former two classical models for describing pre- and post-necking hardening. Other alternatives, such as the linear kinematic hardening law [143], the non-linear Hockett–Sherby hardening function [42] and the Ludwik hardening law [133, 199, 200], are not presented here, although they have also been extensively investigated in FEMU. While the most widely used hardening laws are quite simple, to the point where it might seem unnecessary to calibrate them inversely from heterogeneous tests, FEMU is not just a meaningless complication of this identification task. Compared to classical tests, FEMU can improve the parameter identification accuracy by accounting for the plastic anisotropy. Furthermore, it allows the identification of the material parameters beyond the onset of diffuse necking [201].

Swift's hardening law is one of the most used phenomenological hardening laws describing the evolution of flow stress in sheet metal forming. It is expressed as

$$\sigma_{\text{eq}} = K \left(\varepsilon_0 + \varepsilon_{\text{eq}}^{\text{pl}} \right)^n \quad (11)$$

where K , ε_0 , and n are the three unknown model parameters. Swift's law can only describe a monotonically increasing strain hardening behavior.

Voce's hardening law is the other widely used hardening law, which allows for strain hardening saturation. It is written as

$$\sigma_{\text{eq}} = \sigma_0 + K \left(1 - e^{-n\varepsilon_{\text{eq}}^{\text{pl}}} \right) \quad (12)$$

where σ_0 is the unknown yield stress; K and n are the other hardening parameters. The two hardening laws described above are only effective in the pre-necking region, however.

Their performance in the post-necking region is questionable [202].

p-model is a model proposed by Coppieters and Kuwbara [203] to better describe the post-necking behavior [204] and is written as

$$\sigma_{\text{eq}} = \begin{cases} K \left(\varepsilon_0 + \varepsilon_{\text{eq}}^{\text{pl}} \right)^n, & \varepsilon_{\text{eq}}^{\text{pl}} < \varepsilon_{\text{max}} \\ K \left(\varepsilon_0 + \varepsilon_{\text{max}} \right)^n + \frac{Kn(\varepsilon_0 + \varepsilon_{\text{max}})^{n-1}}{p} \left[1 - e^{-p(\varepsilon_{\text{eq}}^{\text{pl}} - \varepsilon_{\text{max}})} \right], & \varepsilon_{\text{eq}}^{\text{pl}} > \varepsilon_{\text{max}} \end{cases} \quad (13)$$

where p is the so-called post-necking hardening parameter and ε_{max} is the maximum uniform strain. There are 5 unknown parameters involved in this model.

The aforementioned hardening laws have very few unknown parameters. FEMU can efficiently identify all parameters in the Swift's hardening law [44–46, 205–207], Voce's hardening law [42, 187, 196], and p-model [41, 203] using just one or a few tests.

Note that the stress–strain curves of plastic materials are generally quite complicated. Existing models struggle to fit the real hardening behavior, particularly in the post-necking region. A simple way to alleviate this issue is to describe strain hardening behavior with a high-resolution multi-linear hardening model [198, 208–210]. Real hardening behavior has been approximated using a piecewise linear function followed by a smoothing operation based on area conservation [198]. The piecewise linear function requires many more parameters to ensure sufficient accuracy than the previously

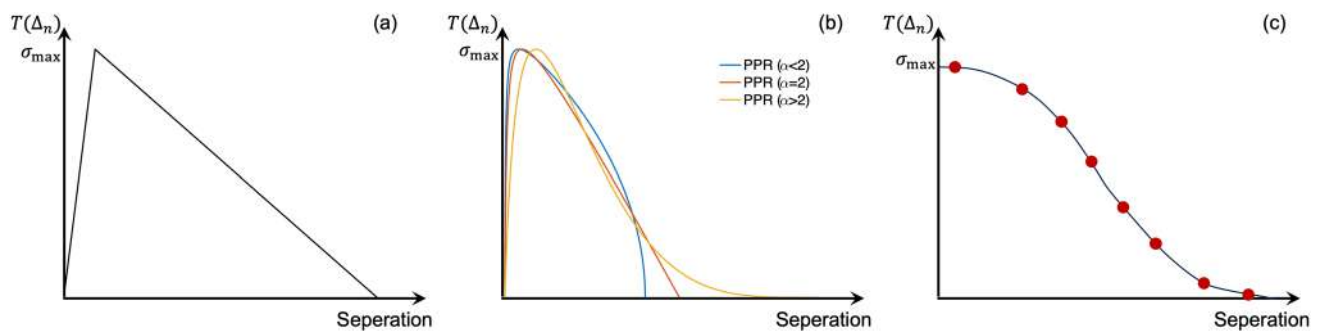


Fig. 12 The traction–separation curves in **a** bilinear CZM, **b** PPR CZM and **c** CZM interpolated from a set of scattered points

mentioned hardening law. In general, it is more computationally expensive for FEMU.

3.4 Fracture Models

There are many ways to model a fracture process zone or crack growth. We can resort to the cohesive zone model (CZM) [211, 212], the phase-field method [213], Extended-finite element method (FEM) [214], and the linear elastic fracture mechanics model. CZM focuses mainly on crack propagation with a distinct fracture process zone behind the crack tip, e.g., delamination of brittle composite materials. To model with CZM, a known crack path is required. The phase-field method is a more versatile method capable of modeling various materials without the crack path information in advance. Linear elastic fracture mechanics (LEFM) is another simple and conventional approach to determine the fracture properties, e.g., the critical stress intensity factor (fracture toughness). The main assumption of LEFM is that plastic deformation in the near crack tip region is negligible, suitable for homogeneous brittle materials [19]. Except for these models, the interface model [215] that can describe the response of joint can also be effectively calibrated by FEMU [216].

CZM is one of the most frequently investigated fracture models in FEMU [217], particularly in the study of (quasi-) brittle materials (e.g., ceramics, brittle composites), thanks to the advantages it offers in terms of good description of the physical phenomena and the physically meaningful parameters [218].

There are different traction–separation curves in CZM, such as the classical bilinear traction–separation [219, 220] (see the traction–separation curve in Fig. 12a) and the Park-Paulino-Roesler (PPR, Fig. 12b) traction–separation [221], have been developed. The traction–separation relation in CZMs can be identified through two different strategies: a parameter optimization method and a shape optimization method. In the parameter optimization method, the traction–separation curve in CZM is described by a limited

number of shape parameters (Fig. 12a and b). In the shape optimization method, the traction–separation curve is not governed by an explicit formula. Instead, it is fitted to a group of scattered points (Fig. 12c).

The classical bilinear model (Fig. 12a) can be described by only three parameters: initial stiffness, maximal traction and maximal separation (or fracture energy). This model has been used and identified in the study of various materials, such as porcine aorta [222] and transparent wood [58].

The shape of the traction–separation curve in bilinear CZM can be changed using a potential-based model such as PPR. The PPR model has enhanced flexibility but more complexity to model the traction–separation relationship. It includes 4 independent parameters. A schematic diagram of the traction–separation curves of this model is shown in Fig. 12b. The identification of PPR model of various materials has been thoroughly investigated by a group of researchers from Brazil and France. In their studies, wedge splitting tests (WSTs) were generally conducted to evaluate the cohesive properties of mortar [56] or refractories [70, 71, 223–225]. The effectiveness of FEMU to identify the PPR model was evaluated through a sensitivity analysis by resorting to the so-called Sobol sensitivity indexes [220].

The shape optimization method (Fig. 12c) does not rely on prior assumptions on the shape of the traction–separation relation [61, 217, 226]. A set of scattered points in the traction–separation domain can be obtained through FEMU. The traction–separation relation is then interpolated from these points using spline interpolation (see Fig. 12c). In this way, a more complex traction–separation curve is obtained. Such freedom with respect to the traction–separation curve offers the possibility to characterize new materials without prior knowledge of the fracture properties. This strategy has been used to study the fracture properties of a ductile adhesive, Devcon Plastic Welder II, and a quasi-brittle plastic, G-10/FR4 Garolite [217]. In these tasks, the parameters were identified through four-point bending tests on single edge-notched beam (SENB).

3.5 Thermomechanical Models

In many scientific or industrial applications, the mechanical behavior of a material or structure will be strongly affected by coupled temperature and mechanical loading. In such cases, it becomes necessary to identify the thermomechanical parameters of the materials [227].

One of the simplest thermomechanical models is an elastic model coupled with the coefficient of thermal expansion (CTE) [228]. In such a model, in addition to the elastic deformation, the heat loading will also induce deformation. Dong et al. [229] identified the thermo-mechanical parameters (two isotropic elastic parameters plus one isotropic CTE) of the Ni-based superalloy GH4169 at 20 to 700 °C. Zhao et al. [129] identified the parameters (three orthotropic elastic parameters and two orthotropic CTEs) in an orthotropic thermo-mechanical material model for nickel-based single crystal superalloys from 600 to 1000 °C based on a modified IDIC method.

Rose and Menzel [105] proposed and identified a thermo-mechanically coupled plasticity model with 15 unknown parameters. This model includes the thermal conductivity, heat capacity, thermal expansion, isotropic elastic parameters, hardening and Hill parameters in the identification process. The authors further extended this model to allow a thermo-mechanically consistent scaling of the dissipation with an additional material parameter, i.e., the dissipation factor [230]. The thermomechanical model was calibrated for an aluminum alloy. The uniaxial tensile tests on dog-bone samples of the aluminum alloy were carried out at room temperature. Their deformation fields were measured by a DIC system, while the temperature field was captured by an infrared (IR) camera. The parameters in these models were then identified using FEMU from the measured deformation and temperature fields.

Gao et al. [231] identified a temperature-dependent elastic–viscoelastic behavior model using FEMU. This model involves 7 unknown parameters. In their work, the DIC-measured displacement on the boundary and the temperature field from IR camera were used as the boundary condition instead of being included in the cost function. As these models are rather complicated, the readers are referred to [105, 230, 231] for a detailed model description. Jailin et al. [227] and Campello et al. [232] calibrated a creep law weakly coupled to the phase transformation of Zircaloy-4 using FEMU. The creep behavior modeled by a thermo-mechanical model was also identified for an environmental barrier coating [233].

3.6 Summary of Material Models in FEMU

Table 5 summarizes some typical material models being extensively used in FEMU. Large systematic errors in FEMU sometimes stem from inaccuracies in the constitutive

equations. There is currently no systematic way to select a best-fit material model. Instead, the most appropriate material model at hand is selected based on expertise. The model should be selected on a physical basis to describe a particular aspect of material behavior (elasticity, plasticity, fracture, etc.). A wrongly selected material model could lead to substantial systematic errors or random errors in the identified parameters [68].

A material model involving a large set of parameters may be a good fit for complicated material behavior. As pointed out by Kolymbas [234], introducing overly complex material models poses several challenges. It hampers their practical application, diminishes computational efficiency, limits the adoption by research groups to only their proprietary models, reduces physical interpretability, complicates calibration and validation, and raises the likelihood of overfitting the material response. Additionally, complex models typically involve a large number of parameters, which can complicate the identification process. Thirdly, since FEMU identifies phenomenological models, it remains uncertain whether such models can fully capture all the underlying mechanisms.

Material models should match the physical meaning well and describe the material response within a decent user-defined error margin. Every material model has a certain range of application. To reduce systematic error, application of the material model should avoid extrapolation. Different research groups are addressing this model selection problem by developing strategies both to evaluate the existing material model [2, 235] and to revise material modelling approaches to make them more universally applicable [236].

A general recommendation regarding material selection is to favor simplicity, but not to the point of oversimplification. The current advancement of AI technology also holds potential for discovering new material models [237]. It is essential to understand that a calibrated model will be accurate under the specific conditions for which it was calibrated. Therefore, it is advisable to design non-conventional experiments to mirror the processes that will be simulated later on, for instance, a forming process.

4 Test Design

To ensure good identifiability and robust identification, the impact of each sought parameter needs to be “fully activated” in the measured heterogeneous deformation fields. Otherwise, the corresponding parameter may be difficult to robustly identify through FEMU. A rich strain state in a highly heterogeneous strain field, can generally be expected to permit simultaneous identification of multiple parameters. The sample geometry may have more impact on the identified parameters than the displacement noise and the

Table 5 Summary of typical material models used in FEMU studies

Model	Constitute equation	Parameter number
<i>Elastic models</i>		
Isotropic elastic model	$\begin{bmatrix} \varepsilon_{xx} \\ \varepsilon_{yy} \\ 2\varepsilon_{xy} \end{bmatrix} = \frac{1}{E} \begin{bmatrix} 1 & -\nu & 0 \\ -\nu & 1 & 0 \\ 0 & 0 & 2(1+\nu) \end{bmatrix} \begin{bmatrix} \sigma_{xx} \\ \sigma_{yy} \\ \sigma_{xy} \end{bmatrix}$	2
Orthotropic elastic model	$\begin{bmatrix} \varepsilon_{xx} \\ \varepsilon_{yy} \\ 2\varepsilon_{xy} \end{bmatrix} = \begin{bmatrix} \frac{1}{E_x} & -\frac{\nu_{yx}}{E_x} & 0 \\ -\frac{\nu_{xy}}{E_y} & \frac{1}{E_y} & 0 \\ 0 & 0 & \frac{1}{G_{xy}} \end{bmatrix} \begin{bmatrix} \sigma_{xx} \\ \sigma_{yy} \\ \sigma_{xy} \end{bmatrix}$	4
Neo-Hookean hyperelastic model	$W = C_1(I_1 - 3)$	1
Gent hyperelastic model	$W = -\frac{\mu}{2} J_m \ln\left(1 - \frac{I_1 - 3}{J_m}\right)$	2
Mooney Rivlin hyperelastic model	$W = C_1(I_1 - 3) + C_2(I_2 - 3)$	2
<i>Plastic models</i>		
Hill48 yield criterion	$\sigma_{eq}^2 = H(\sigma_{11} - \sigma_{22})^2 + F\sigma_{22}^2 + G\sigma_{11}^2 + 2N\sigma_{12}^2$	3
Yld2000-2d yield criterion	$2\sigma_{eq}^m = X'_1 + X'_2 ^m + 2X''_2 + X'_1 ^m + 2X''_1 + X'_2 ^m$, see details in Eqs. (8–10)	8
Swift's hardening law	$\sigma_{eq} = K(\varepsilon_0 + \varepsilon_{eq}^{pl})^n$	3
Voce's hardening law	$\sigma_{eq} = \sigma_0 + K(1 - e^{-n\varepsilon_{eq}^{pl}})$	3
p-model	$\sigma_{eq} = \begin{cases} K(\varepsilon_0 + \varepsilon_{eq}^{pl})^n, & \varepsilon_{eq}^{pl} < \varepsilon_{max} \\ K(\varepsilon_0 + \varepsilon_{max})^n + \frac{Kn(\varepsilon_0 + \varepsilon_{max})^{n-1}}{p} \left[1 - e^{-p(\varepsilon_{eq}^{pl} - \varepsilon_{max})}\right], & \varepsilon_{eq}^{pl} > \varepsilon_{max} \end{cases}$	5

selected area of displacement field [238]. It is thus necessary to carefully design the sample geometry and load paths for the examined material and material model—an important topic that makes up the very core of the FEMU technique and has been discussed in some review papers [4, 239].

The strategies for sample geometry design roughly fall into two major categories: (i) heuristic-based design; (ii) optimization-based design. The heuristic-based design generates geometries according to certain practical rules. This requires extensive expertise. In most cases, the tests are not optimal. It is, in theory, more reliable to consider test design as an optimization task, which leads to optimization-based design. In optimization-based designs, the test is parametrized by way of a set of modifiable parameters. Optimal tests for robust parameter identification are developed through iterative updating by optimizing certain qualitative or quantitative criteria. Note that test design shares the same role and importance in FEMU and VFM. Therefore, this section also covers some typical tests designed for VFM. These designs could be directly transferred to FEMU tasks.

4.1 Heuristic-Based Design

In the early development stage of FEMU, the samples are generally designed based on some guidelines instead of through a process of optimization. They are mostly designed by adding geometric features, such as holes or notches, to introduce richer strain states. These samples, while not optimal, still work well in the corresponding applications. According to the test configuration, these samples could be classified into uniaxial and biaxial tensile test samples, and other samples, such as three-/four-point bending samples, fracture test samples, Iosipescu test samples, etc.

4.1.1 Uniaxial Tensile/Compression Test

Uniaxial tensile/compression tests are still the most popular tests in inverse parameter identification tasks. This is mainly attributed to the wide availability of uniaxial tensile testing machines and the simplicity of test implementation. Dozens of sample geometries designed through a heuristic approach have been reported in the literature. A summary of these sample geometries and their applications is given in Fig. 13.

4.1.1.1 Classical Geometries The most straightforward geometries are the classical samples used in conventional mechanical tests. Jungstedt et al. [59] used FEMU to determine all four independent elastic constants of orthotropic all-lignocellulose composites from a single 45° off-axis strip sample (Fig. 13a) via a uniaxial tensile experiment. Henriques et al. [68] identified the orthotropic elastic parameters of wood [46] through a 60° off-axis uniaxial compression test. The four parameters are activated simultaneously in a single test, although their identifiability may not be optimal.

Rose and Menzel [105] identified the thermo-mechanically coupled material model of aluminum alloy AW6016 using the classical heterogeneous dog-bone-shaped sample (Fig. 13b). Shortening the gauge area can effectively increase the strain heterogeneity for inverse identification in the gauge region. Zhang et al. [201] used a standard dog-bone sample to extract the post-necking hardening behavior from the diffuse necking in thick high strength steel. Belhabib et al. [240] also used this heterogeneous tensile test sample to calibrate the elastoplastic material model parameters of dual-phase steel. FEA shows that this test is a good compromise between the following three criteria: (i) large heterogeneity of the strain in the gauge area, (ii) large strain-path diversity and (iii) good sensitivity of the strain field to the material parameters [240].

The dog-bone samples with arcuate notches (Fig. 13c) also have good strain heterogeneity. Conde [205] used such a sample to identify the three parameters in the Swift hardening law of DP600 steel. Although the results of the identification are notably dependent on the initial guess of the parameters, these are still adequately calibrated through the tests. Similar sample geometry was also adopted by Jacquet et al. [241] to characterize the parameters in elasto-viscoplastic material model. Güner et al. [103] used this geometry to calibrate the planar plastic anisotropy of sheet metals, where the flexible Yld2000-2D yield condition is used in the plasticity model.

The dog-bone geometry evolves into an hourglass sample (Fig. 13d) if the neck region is thin. This hourglass geometry can produce strain fields under uniaxial tensile test that are more heavily heterogeneous [39]. It will, however, lose some effective ROI on the sample surface. This sample geometry has served as the benchmark to explore the influence of user-defined DIC parameters on the identification of isotropic elastoplastic material model parameters [39].

4.1.1.2 Perforated Geometries Adding hole(s) to the uniaxial tensile test samples is an effective strategy to enhance the strain heterogeneity. The perforated strip sample (Fig. 13e) has been used as the benchmark sample geometry when investigating the influence of different cost functions [242] in FEMU. Seon et al. [51] used this geometry to identify the orthotropic elastic parameters of advanced polymeric

composites. The calibrated parameters are in line with the ones measured through standard tensile tests in literature. The well identified elastic parameters further enabled the determination of the maximum interlaminar tensile strength from a 2D plane stress static FE analysis. Wang et al. [38] used this sample to identify the plastic anisotropy of DC06 based on the Hill48 yield criterion. Compared with Erichsen test, this test revealed obvious identifiability differences for different parameters. They found that F and H are more reliably identified with the Erichsen specimen, while N is more reliably identified with the perforated specimen. The dog-bone sample could also be modified with an open-hole (Fig. 13f) for FEMU. This geometry has been used to identify the elasto-plastic material properties of aluminum [48].

The aforementioned are sheet samples, which could be further generalized to a thick offset double perforated specimen [44] (Fig. 13g). The six parameters in the 3D Hill48 yield surface of S690QL high strength steel can be identified by measuring the strain distribution on the front and thickness surface simultaneously using a multi-view DIC system. The identification revealed that S690QL has negligible plastic anisotropy. The thick sample can provide more information for FEMU if the strain fields on different surfaces are properly measured.

4.1.1.3 Notched Geometries The notched geometries are the ones adopted by the pioneers in FEMU community [86, 87]. In 1996, Mahnken and Stein used a single-side notched sample (Fig. 13h) to identify the exponential hardening model of a mild steel specimen [86].

The geometry with two asymmetric notches (Fig. 13i) was used in the other pioneering works [50, 87] of FEMU and VFM [243]. This non-standard shear-like geometry results in inhomogeneous stress- and strain-fields. It was used to determine the yield stresses of aluminum plates in the isotropic Von Mises and the orthotropic Hill yield criterion. It was also adopted to calibrate the anisotropic elastic plastic parameters of pure titanium material. A similar geometry was adopted by Meraghni et al. [244] to identify the fatigue damage model parameters for short glass fiber reinforced polyamide (PA6-GF30). Comparison tests validated that this non-standard shear-like geometry can produce better identification results than the perforated geometries and the standard strip geometry. This is mainly the result of the more significant strain heterogeneities [50].

Similar geometry with double semicircular notches (Fig. 13j) was investigated by Gajewski et al. [242]. They demonstrated that FEMU using this asymmetrical geometry is quite suitable for plasticity parameter identification. Rossi and Pierron [245] used a uniaxial tensile specimen (Fig. 13k) with a symmetric circular-arc notch on each side. This sample was used to identify the plastic behavior of thick metal specimens (316L stainless steel) using VFM.

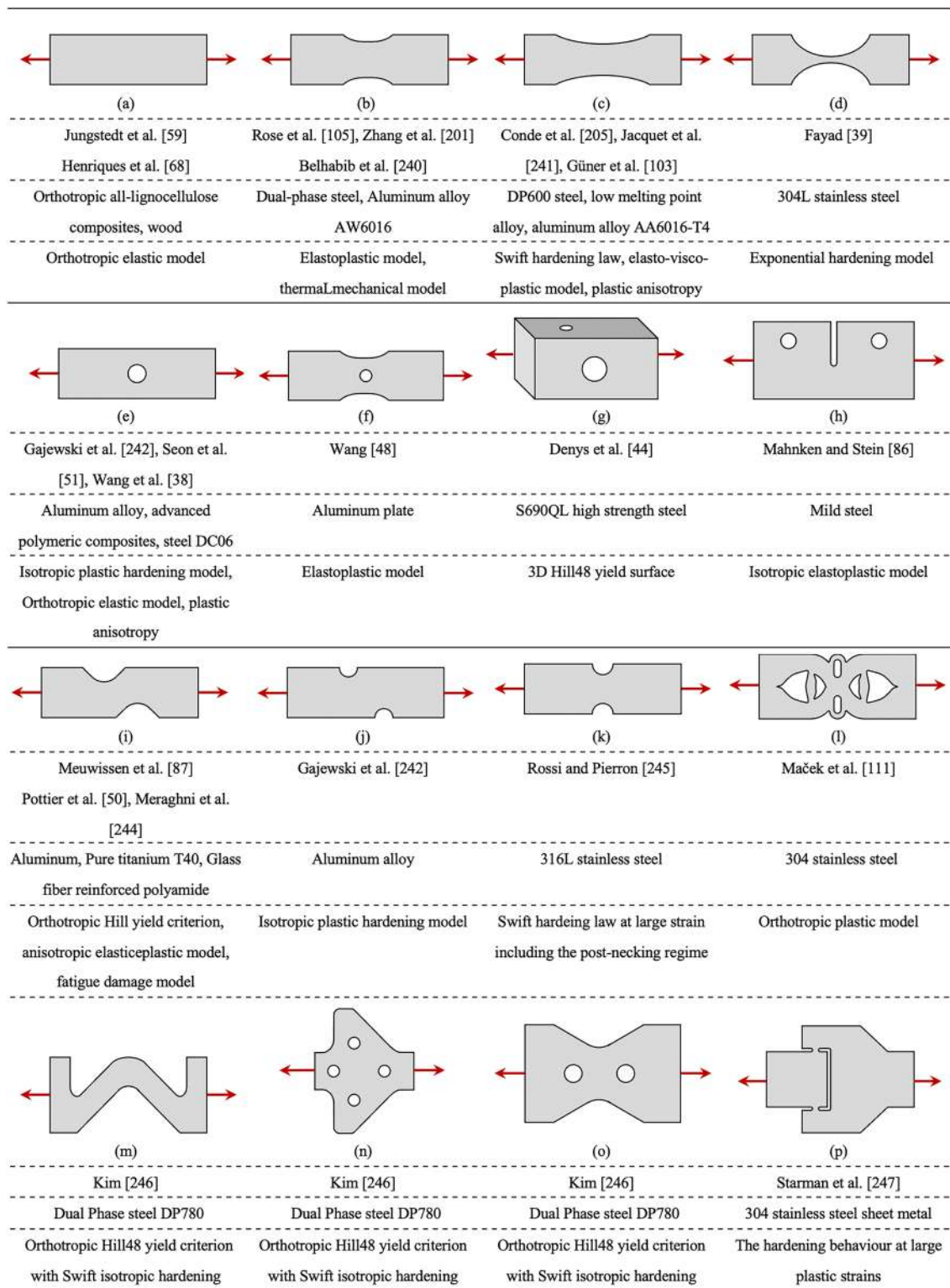


Fig. 13 Uniaxial tensile test samples designed by heuristic. The geometries shown here are schematic diagrams which do not preserve dimension information

The plasticity behavior at large strains, including the post-necking regime, was calibrated. The displacement fields on both surfaces of the specimen were measured simultaneously using two stereo-DIC systems. The heterogeneous volume displacement field inside the specimen was roughly estimated to describe the strain localization in the necking region for Swift law calibration.

4.1.1.4 Unconventionally Designed Geometries Besides the above, some unconventional geometries, such as “symmetric-face-shaped” [111] (Fig. 13l) and “ Σ -shaped” geometry [246] (Fig. 13m) are reported in literature. At first glance, these geometries look complicated. However, they yield highly heterogeneous strain states and can therefore facilitate rather robust identification of the parameters for inverse identification.

The “symmetric-face-shaped” geometry was designed under the criteria of (i) a pronounced biaxial stress state at the center of the specimen and (ii) small stress or strain concentration [111]. This test enabled accurate identification of the anisotropic plastic parameters in the advanced YLD2000-2d model.

Four typical geometries (Fig. 13c, m, n, o) were studied by Kim et al. [246] to calibrate the parameters in the orthotropic Hill48 yield criterion with Swift isotropic hardening law, though with VFM instead of FEMU. It was found that the geometry in Fig. 13m can produce highly heterogeneous stress states. This geometry enabled successful identification of the anisotropic plastic parameters. The geometry in Fig. 13n tends to buckle in the experiment. The geometry in Fig. 13o is interesting since it exhibits biaxial stress states in the central area between the two holes. The geometry in Fig. 13c, however, failed to permit simultaneous identification of all the anisotropic plastic parameters.

Starman et al. [247] proposed a new shear specimen (Fig. 13p) in a tensile test. It was used for the characterization of hardening at large plastic strains beyond necking initiation. This geometry can promote a shear response in two symmetrically located shear regions.

4.1.2 Biaxial Tensile Test

Applications like sheet metal forming are generally performed under multi-axial strain paths with significant heterogeneous deformation [195]. To better approximate the real-world loading scenarios for more robust parameter identification, in-plane biaxial tensile tests that yield complex strain paths are widely employed. Sheet specimens with cruciform geometries, perforated cruciform geometries, and three-branch geometry have been proposed for parameter identification. The typical biaxial tensile tests designed by heuristic are reviewed and summarized in Fig. 14. All these samples are loaded on all their arms simultaneously.

4.1.2.1 Cruciform Geometries The cruciform geometry is currently the most popular biaxial tensile test sample in use for parameter identification. Tomičević et al. [47] proposed a cruciform geometry (Fig. 14a) to identify the elastic and nonlinear plastic parameters of graphite cast iron. The geometry they designed resembles a Maltese cross thinned in the center, allowing crack initiation in the center. The sample was loaded under different biaxial loading paths: “proportional” in-plane biaxial loading and “disproportionate” in-plane biaxial loading.

In comparison, flat sheet samples permit easier application, since they can be manufactured directly by laser cutting. Avril et al. [93] tested flat Maltese cross samples (Fig. 14a) of a composite consisting of a vinyl ester matrix reinforced with E-glass fiber in an equibiaxial manner. Different inverse identification methods were compared using this biaxial tensile test. A comparison of the identified elastic moduli and Poisson’s ratios permits the evaluation of the identification performance.

Zhang et al. [248] adopted a slightly different cruciform geometry (Fig. 14b). This sample was used to identify the parameters in the Bron and Besson anisotropic yield model of various materials, including aluminum alloy series 5000 [183], aluminum alloy AA5086 and dual phase steel DP980 sheets [189]. A comparison study [162] revealed that properly adjusting the radius of the fillets on this sample can significantly reduce parameter identification error by enhancing the strain heterogeneity.

In addition to the symmetric geometry, Schmaltz and Willner [42] investigated a centrosymmetric geometry (Fig. 14c). This sample was used to identify the anisotropic elasto-plastic model parameters of sheet steel. This geometry also produces a compressive stress in the biaxial tensile test. It does not, however, produce reasonable results in terms of the hardening curve identification. This could be due to the large concentrated tensile load on the thin cross sections where the radii of the slits are located [42].

4.1.2.2 Perforated Cruciform Geometries Adding an open hole in the middle of cruciform geometries can further enhance the strain heterogeneity. The perforated cruciform geometries usually have fillets in the corners to reduce strain concentrations. These fillets may have different shapes and dimensions, leading to performance variation in terms of inverse identification.

The geometry shown in Fig. 14d is a widely adopted design. Lecompte et al. [94], Cooreman et al. [207], Coppieters et al. [249] and Garbowski et al. [250] adopted this design to calibrate the parameters within an orthotropic elastoplastic-hardening model of metal (DC06 steel [207]) or paper [250].

Martins et al. [162] proposed a perforated cruciform geometry with invaginated round fillets (Fig. 14e). This

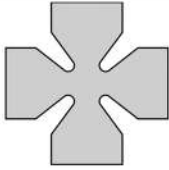
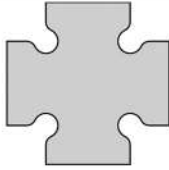
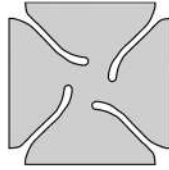
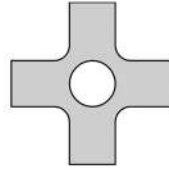
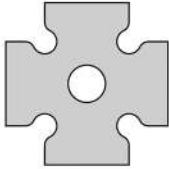
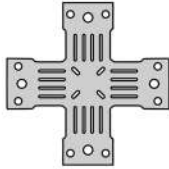
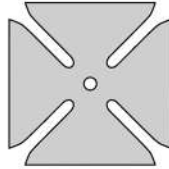
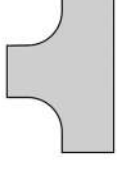
			
(a)	(b)	(c)	(d)
Avril et al. [93], Tomičević et al. [47]	Zhang et al. [189,248]	Schmaltz and Willner [42]	Cooreman et al. [207], Lecompte et al. [94], Coppieeters et al. [249], Garbowski et al. [250]
Fiber reinforced composite, Graphite cast iron	Aluminum alloy, dual phase steel	Sheet steel	Metal, paper
Elastic model, elastic and nonlinear plastic models	Anisotropic yield model	Anisotropic elasto-plastic model	Orthotropic elastoplastic- hardening model
			
(e)	(f)	(g)	(h)
Martins [162]	Teaca et al. [251]	Schmaltz and Willner [42]	Guélon. [253]
Aluminum alloy	Steel and aluminum sheets	Sheet steel	Rubber
Elastoplastic-hardening model	Plastic model	Anisotropic elasto-plastic model	Mooney hyperelastic model

Fig. 14 Biaxial test samples designed by heuristic. All samples are loaded along the branches. The geometries shown here are schematic diagrams which do not preserve dimension information. All the samples are stretched along all arms simultaneously

geometry has been used to calibrate the classical Hill48 yield criterion and Swift's hardening law. Their work compared the same geometry with and without an open hole in the middle. The perforated cruciform geometry leads to wider dispersion of strain and stress states. Consequently, it can lead to improved parameter identification accuracy [162].

Teaca et al. [251] proposed a non-standard cruciform specimen perforated at multiple locations (Fig. 14f). This design can provide a wide range of strain-paths and a high sensitivity to material anisotropy. It was used to calibrate an 8-parameter anisotropic yield function [252]. Schmaltz and Willner [42] also proposed a perforated cruciform geometry, see Fig. 14g. The authors claimed that this geometry helps achieve a better convergence when compared to three other geometries, including the same geometry without the open-hole and the one shown in Fig. 14c.

4.1.2.3 Three-Branch Geometry The three-branch geometry [253] (Fig. 14h) is not that commonly used. Instead, it was designed to apply biaxial loads by using a uniaxial tensile machine. Uniaxial tensile machines are much more

accessible than the biaxial tensile machines. Therefore, the test can be easily conducted. To this end, they designed a new tensile apparatus which is fixed to one of the two columns on the tensile machine. This apparatus can clamp and load the horizontal branch with a measurable displacement. The parameters in a Mooney hyperelastic model [254] of a carbon black filled natural rubber material were identified using VFM.

4.1.3 Other Tests

In addition to the commonly used uniaxial and biaxial tensile tests, there are others that produce complex strain states and are often feasible for inverse identification. The other tests, such as three-point/four-point bending tests, fracture tests, ring sample and Brazilian disk compression tests, Iosipescu tests and out-of-plane tests have also been explored by FEMU researchers. A summary of these tests is shown in Fig. 15.


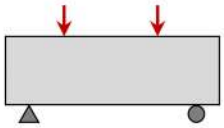
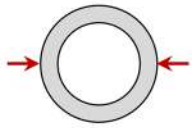
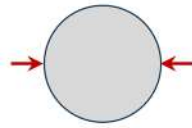
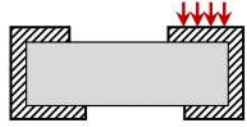
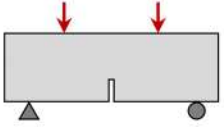
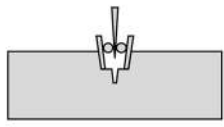

			
(a)	(b)	(c)	(d)
He et al. [255], Nsengiyumva and Kim [158], Gras et al. [164]	Gao et al. [256], Liu et al. [257]	Liu et al. [258]	Avril et al. [93]
Composites, polyetheretherketone, layer-to-layer interlocked woven composite	Bamboo, graphite material	Graphite	Polycarbonate
Elastic modulus, viscoelastic parameters, out-of-plane shear modulus	Radial elastic modulus distribution, damage evolution parameters	Heterogeneous elastic parameters	Isotropic elastic parameters
			
(e)	(f)	(g)	(h)
Avril et al. [93], Nigamaa and Subramanian [259]	Shen et al. [217,226]	Vargas et al. [19,71,224]	Pottier et al. [264], Souto et al. [265]
Glass-epoxy unidirectional composite	Polymethylmethacrylate	Refractory	Sheet metal
Four in-plane elastic constants	CZM	CZM	Orthotropic elastoplastic model

Fig. 15 Other samples designed by heuristic: **a** three-point bending test, **b** four-point bending test, **c** ring sample compression test, **d** Brazilian disk compression test, **e** Iosipescu test, **f** four-point bending

test of notched SENB specimen, **g** wedge-splitting tests and **h** out-of-plane punching test. The geometries shown here are schematic diagrams which do not preserve dimension information

4.1.3.1 Three-/Four-Point Bending Tests These tests are generally used for the identification of orthotropic elastic or viscoelastic parameters in a FEMU scenario, likely due to the simple sample preparation and test implementation. He et al. [255] conducted a short beam three-point bending test (Fig. 15a) to calibrate the elastic modulus, Poisson's ratio and nonlinear shear stress–strain relations of highly anisotropic composites. Their research revealed that the longitudinal Young's modulus identification is more sensitive to measurement noise in this test. Nsengiyumva and Kim [158] performed a three-point bending test to calibrate the homogenous elastic parameters of polyetheretherketone and viscoelastic parameters of a fine aggregate matrix with a bituminous binder. Similar test also helped Gras et al. [164] to characterize the out-of-plane shear modulus of a layer-to-layer interlocked woven composite. The four-point bending test (Fig. 15b) can reduce the stress localization in the sample center close to the load pin compared to the three-point bending test. The strain field can therefore be measured more robustly in this region. Gao et al. [256] and Liu et al. [257] used this test in their work. Their aim was to determine the radial elastic modulus distribution of bamboo and the damage evolution parameters (related to elastic modulus evolution) of a graphite material, respectively. The

four-point bending test has minimized shear stress, however, and is thus not a good candidate for shear modulus identification.

4.1.3.2 Ring Sample and Brazilian Disk Compression Tests The ring sample compression test and the Brazilian test are simple and established in experimental solid mechanics. Both tests can yield informative strain states for robust anisotropic parameter identification. Liu et al. [258] compressed a ring sample (Fig. 15c) to identify the heterogeneous parameter distribution in a graphite material. They evaluated material damage under complex stress states via this test. The Brazilian test has an interesting extra feature, namely the existence of a closed-form solution for displacement calculation. It could be beneficial for improving the efficiency of parameter identification. Avril et al. [93] also employed the Brazilian test (Fig. 15d) on a polycarbonate sample to benchmark different inverse identification techniques.

4.1.3.3 Iosipescu Test The Iosipescu test (Fig. 15e) is highly suitable for activating the shear strain response on the sample surface. It is a common test for inverse parameter identification, especially for orthotropic materials, e.g.,

composites. Avril et al. [93] used this test to compare the performance of FEMU, VFM and CEGM. The four in-plane elastic constants of orthotropic materials [93, 259], for instance a glass–epoxy unidirectional composite material, can all be robustly identified. This test performs better than the three-point bending test for the calibration of the out-of-plane shear modulus of a layer-to-layer interlocked woven composite [164]. This can be attributed to the higher stress heterogeneity in Iosipescu test.

4.1.3.4 Fracture Tests Calibrating the fracture mechanics parameters is a major task in the characterization of brittle or quasi-brittle materials. Four-point bending tests of a notched SENB specimen and wedge-splitting tests have been widely used. Shen et al. [217, 226] used CZM to simulate the fracture of PMMA. The CZM parameters were determined using FEMU via a four-point bending test of SENB (Fig. 15f). The WST (Fig. 15g) adopted by Vargas [19, 71, 224] ensures stable crack propagation in fracture tests by decreasing the elastic energy stored in testing machine, since the opening (mode I) load is applied by a wedge and a pair of cylinders. This test was used to identify the CZM parameters for a class C, anti-erosive commercial refractory.

4.1.3.5 Indentation Tests Indentation tests are commonly used to study the mechanical properties of a material by pressing an indenter tip into the sample surface. The indentation tests employed in inverse parameter identification tasks can use various indenter tips, such as the spherical indenter tip [175], the Berkovich indenter tip [260, 261], and the Vickers micro-indenter [262]. Chen et al. [175] identified the hyperelastic parameters of silicone rubber from the load-depth data in a macroindentation test using FEMU. Sun et al. [262] used microindentation to calibrate the heterogeneous elastoplastic property distribution near the weld line region.

Barick et al. [260] and Gebhardt et al. [261] carried out a nanoindentation test instead. Barick et al. [260] identified the four-parameter viscoelastic law with constant Poisson's ratio for polypropylene using the load-depth curve information. Gebhardt et al. [261] made use of the strain fields measured by DIC to identify the elastic and plastic model parameters for ferrite. Satošek et al. [263] used ball indentation to inversely identify the out-of-plane shear parameters of the Yld2004-18p yield function.

4.1.3.6 Out-of-Plane Tests The out-of-plane tests can potentially better mimic the strain states occurring in an actual metal forming process, though at the cost of more sophisticated test implementation. It must be noted that plane stress conditions generally still prevail in out-of-plane tests. Pottier et al. [264] proposed a typical out-of-plane test (Fig. 15h) to calibrate an elastoplastic material model. A

hemispherical punch imposed out-of-plane displacement in the middle of the specimen. The specimen exhibits significantly heterogeneous strain paths, including tensile, shear and expansion behaviors. The deep-drawing experiment was compared with the numerical simulation based on the identified parameters. The results confirmed that out-of-plane tests can calibrate the parameters with better accuracy than in-plane tests. Souto et al. [265] reevaluated this test to assess a geometry design indicator for inverse parameter identification.

4.2 Optimization-Based Design

In optimization-based design methods, optimal tests are designed by iteratively optimizing certain qualitative or quantitative criteria. Different qualitative or quantitative optimization indicators lead to various optimization-based designs. The test can be designed based on stress and strain states, sensitivity analysis or the simulated full identification workflow.

Maximizing an indicator based on stress and strain heterogeneity is a simple and straightforward way to design a test. However, it is not directly related to parameter identification performance. Sensitivity analysis can help in designing a test with good parameter identifiability. By simulating the full identification workflow, the errors in all steps, including DIC matching, can be adequately accounted for. A test design with good parameter identification accuracy can thus be obtained. Figure 16 presents a summary of the major methods of optimization-based test design.

4.2.1 Design Based on Stress and/or Strain States

This type of test is generally designed based on the stress and/or strain distribution on the sample surface. FEA can simulate stress and strain maps, given the model and the model parameters. The designs should satisfy several criteria related to the stress and/or strain states. The most important criterion is a high stress and/or strain state heterogeneity. In this review, we classify those design approaches into trial-test design based on qualitative criteria, iterative optimization-based design using performance indicators, and topology-optimization-based design. The major design criteria and the designed tests are reviewed hereafter.

4.2.1.1 Trial-Test Design Based on Qualitative Criteria The most straightforward way designs the sample geometry through simulated trial tests using some qualitative criteria.

Jones et al. [266, 267] proposed a 'D'-shaped geometry (Fig. 16) for a uniaxial tensile test. The design procedure starts from engineering experience. The geometry is then manually refined based on FEA results using the following criteria:


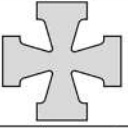


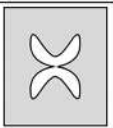
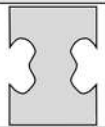
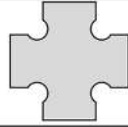
Criteria	Classification	Geometry	Reference
■ Design based on stress and strain states: tests with heterogeneous strain and stress distribution			
Qualitative criteria	Trial-test design		Jones et al. [266]
Qualitative criteria	Trial-test design		Prates, et al. [195,206]
Minimize $C = \frac{(\bar{\epsilon}_y - \bar{\epsilon}_x)^2}{(\bar{\epsilon}_y + \bar{\epsilon}_x)} + \frac{(\bar{\epsilon}_x - \bar{\epsilon}_y)^2}{(\bar{\epsilon}_x + \bar{\epsilon}_y)} + \frac{(\bar{\epsilon}_y - \bar{\epsilon}_z)^2}{(\bar{\epsilon}_y + \bar{\epsilon}_z)}$	General iterative optimization-based design		Grédiac et al. [88,268]
Maximize $I_T = W_{r1} \frac{\text{Mean}(\text{Std}(\frac{\epsilon_z}{\epsilon_1}))}{W_{a1}} + W_{r2} \frac{(\frac{\epsilon_z}{\epsilon_1})_R}{W_{a2}}$ $+ W_{r3} \frac{\text{Mean}(\text{Std}(\epsilon^P))}{W_{a3}} + W_{r4} \frac{\bar{\epsilon}_{\max}^P}{W_{a4}} + W_{r5} \frac{AV_{\text{pp}}}{W_{a5}}$	General iterative optimization-based design		Aquino et al. [193,270] Martins et al. [185] Andrade-Campos et al. [191] Souto, et al. [190,269]
	General iterative optimization-based design		Conde et al. [46,205,271]
	General iterative optimization-based design		Zhang et al. [186]
Maximize $I_T = W_{r1} \frac{\text{Std}(TF)}{W_{a1}} + W_{r2} \frac{(TF)_R}{W_{a2}}$ $+ W_{r3} \frac{\text{Std}(\epsilon^P)}{W_{a3}} + W_{r4} \frac{\bar{\epsilon}_{\max}^P}{W_{a4}} + W_{r5} \frac{AV_{\text{pp}}}{W_{a5}}$	General iterative optimization-based design	Comparison of existing geometries	Thoby et al. [106]
Cost functions based on stress-strain state	Topology-optimization-based design	Several complicated geometries	Almeida et al. [273] Barroqueiro et al. [274] Gonçalves et al. [275,276]
■ Design based on sensitivity analysis: tests with good parameter identifiability			
Maximize the smallest sensitivities to all parameters	General iterative optimization-based design	An embedded wood-based panel	Bos et al. [278] Magorou et al. [279]
Minimizing the covariance matrix of the identified material parameters due to acquisition noise	General iterative optimization-based design		Bertin et al. [40]
■ Design based on simulated full identification workflow: tests with small parameter identification error			
Minimize $I_T = \frac{1}{N_e} \sum_i^{N_e} \sqrt{\sum_k^M \omega_k \left(1 - \frac{p_k^{(i)}}{p_k^{(0)}}\right)^2}$	General iterative optimization-based design	Iosipescu test, see Fig. 15 (e)	Rossi and Pierron [281]
Minimize $I_T = \frac{1}{M} \sum_k^M \left(\left 1 - \frac{p_k}{p_k^{(0)}}\right + 2 \frac{\sigma_{p_k}}{p_k^{(0)}} \right)$	General iterative optimization-based design	Short off-axis tensile test, short off-axis open-hole tensile test, Brazilian disc and off-axis unnotched Iosipescu test	Gu and Pierron [282]

Fig. 16 Optimization-based sample designs. The geometry shown here are the schematic diagrams which do not preserve dimension information

- (i) Maximizing the stress heterogeneity.
- (ii) Maximizing the range of strain rates.
- (iii) Minimizing the large gradients in stress or strain near sample edges.
- (iv) Restricting the geometry to be planar while preventing buckling.

Prates et al. [195, 206] designed a cruciform specimen (Fig. 16) based on the following rules:

- (i) Maximizing the coverage of strain paths that occur in real-world applications.
- (ii) Maximizing the strain level in the center of the specimen.
- (iii) Minimizing the stress concentration in the fillet region.
- (iv) Yielding a smooth gradient of the ratio between the maximum and minimum principal strains on the specimen arms.

These tests are expected to perform better than the heuristic-based designs, although the optimization is not fully automatic. This is attributed to, firstly, the more detailed design criteria. Additionally, tests with different geometry parameters are tried and compared following these rules.

4.2.1.2 Iterative Optimization-Based Design Using Performance Indicators In the iterative optimization-based design method, the geometry is designed by iteratively refining a set of shape parameters. Usually, a quantitative identification performance indicator is formulated as the cost function for geometry optimization.

The first attempt to optimize the sample geometry with iterative parameters optimization is from Grédiac et al. [88, 268] in the late 1990s. They designed a ‘T-shape’ specimen (Fig. 16) submitted to both tension and bending loading. The horizontal short beam on this ‘T-shape’ specimen is mainly subjected to bending load. It can activate the horizontal Young’s modulus and the in-plane shear modulus. The vertical bar on the ‘T-shape’ sample is used to impose a tensile load for longitudinal modulus activation. This ‘T-shape’ geometry is governed by four independent dimensional parameters (lengths and widths of the horizontal and vertical bars). The optimal geometry can be found by searching in the four-parameter space to minimize the following cost function.

$$C = \frac{(\bar{\epsilon}_y - \bar{\epsilon}_x)^2}{(\bar{\epsilon}_x + \bar{\epsilon}_y)} + \frac{(\bar{\epsilon}_x - \bar{\epsilon}_s)^2}{(\bar{\epsilon}_x + \bar{\epsilon}_s)} + \frac{(\bar{\epsilon}_y - \bar{\epsilon}_s)^2}{(\bar{\epsilon}_y + \bar{\epsilon}_s)} \tag{14}$$

This cost function is related to strain heterogeneity, where $\bar{\epsilon}_x$, $\bar{\epsilon}_y$, $\bar{\epsilon}_s$ are the averages of the horizontal strain ϵ_x , vertical strain ϵ_y and shear strain ϵ_s in area 1, 2, 3 (Fig. 16),

respectively. This optimized ‘T-shape’ geometry was used for the identification of the four in-plane elastic parameters of orthotropic composite plates using VFM. The identified material model parameters showed good accuracy with acceptable deviation from the reference value.

The aforementioned indicator is proposed specifically for designing ‘T-shape’ specimens. It may not be versatile enough to be useful for the other tests. A desirable indicator should facilitate fair evaluation in various kinds of tests and materials. In the scenario of sheet metal parameters identification, one of the most successful applications of FEMU, Souto et al. [265] proposed to design the sample geometry by considering the following criteria:

- (i) Favoring tests that cover a larger range of strain states with a minor number of gaps.
- (ii) Promoting tests with significant deformation heterogeneity.
- (iii) Increasing the maximum strain achieved for the most important strain states.
- (iv) Preferring large average strain values.
- (v) Continuously evaluating the indicator up to rupture.
- (vi) Promoting the uniqueness of the identification results.

Taking these considerations into account, they proposed a new indicator to distinguish, rate and rank different mechanical tests, see Eq. (15):

$$I_T = W_{r1} \frac{\text{Mean}\left(\text{Std}\left(\frac{\epsilon_2}{\epsilon_1}\right)\right)}{W_{a1}} + W_{r2} \frac{\left(\frac{\epsilon_2}{\epsilon_1}\right)_R}{W_{a2}} + W_{r3} \frac{\text{Mean}\left(\text{Std}\left(\epsilon^{-p}\right)\right)}{W_{a3}} + W_{r4} \frac{\epsilon_{\max}^{-p}}{W_{a4}} + W_{r5} \frac{AV_{\epsilon}^{-p}}{W_{a5}} \tag{15}$$

Each term in this indicator denotes a constraint for the geometry optimization. This indicator is explained as follows:

- (i) $\text{Std}\left(\frac{\epsilon_2}{\epsilon_1}\right)$: strain state range variation of the test, where ϵ_1 and ϵ_2 are the major and minor principal strain, respectively.
- (ii) $\left(\frac{\epsilon_2}{\epsilon_1}\right)_R = \left(\frac{\epsilon_2}{\epsilon_1}\right)_{\max} - \left(\frac{\epsilon_2}{\epsilon_1}\right)_{\min}$: the strain state range of the mechanical test.
- (iii) $\text{Std}\left(\epsilon^{-p}\right)$: non-homogeneity of the strain field during test, evaluated as the variation of the equivalent plastic strain $\bar{\epsilon}^p$.
- (iv) $\bar{\epsilon}_{\max}^p = \frac{\bar{\epsilon}_{\text{test}}^p + \bar{\epsilon}_{\text{tens}}^p + \bar{\epsilon}_{\text{shear}}^p + \bar{\epsilon}_{\text{biaxial}}^p + \bar{\epsilon}_{\text{comp}}^p + \bar{\epsilon}_{\text{plane}}^p}{6}$: the maximum strain, which is calculated as the average of the maximum plastic strain $\bar{\epsilon}^p$ at different strain states (the test,

uniaxial tension, pure shear, equibiaxial tension, uniaxial compression, plane strain tension).

- (v) Av_{ϵ}^{-p} : the average deformation in the test, which indicates the global level of deformation imposed during the test.

where ‘Mean()’ is the average operator and ‘Std()’ the standard deviation operator. The weighting factors W_{a1-a5} represent the maximum possible value of each term. They could be selected as 1, 4, 0.25, 0.8 and 0.4, respectively [190]. The relative weighting factors W_{r1-r5} are specified according to the importance of each term in the indicator. One possible set of values is given as 0.13, 0.02, 0.24, 0.35, 0.25 [190].

This indicator serves as the foundation for optimal test selection and design in a series of research advancements. The same group proposed two different optimization approaches for designing heterogeneous mechanical tests on virtual thin metallic sheets (described by an Yld2004-18p yield criterion combined with a mixed isotropic-kinematic hardening law) with the aid of this indicator [190]. The first approach is a one-step procedure. It is used to design both a symmetric specimen shape (parameterized by 7 control points) and a biaxial loading path using rigid tools. The second approach is a sequential incremental technique in which the specimen geometry and the load paths are designed by considering local displacements (at 7 points, different from the first approach). In the second approach, the following aspects are sequentially designed: (i) initial specimen shape, (ii) boundary conditions by means of local displacements and (iii) a complex loading path. Two geometries were optimized with the two different methods. The indicator suggests that the test with the complex loading path can provide richer strain information than the one with only a biaxial loading path.

Due to the simplicity of the boundary condition, the first approach was also adopted to optimize the geometry and boundary in an uniaxial tensile test [269]. The design started from an initial circular geometry. The optimization procedure iteratively reached a butterfly-shape uniaxial tensile sample (Fig. 16). The effectiveness of the designed test was validated in a real experiment. It identified the material model parameters of mild steel DC04 material. The material is described by the non-quadratic Yld2004-18p yield criterion combined with a mixed isotropic-kinematic hardening law [193, 270]. The designed test was also used for calibrating the post-necking hardening behavior of sheet metal DC05. An anisotropic model composed of the Hill48 yield criterion and Swift’s hardening law [185] was assumed for the material.

Apart for this complicated test, uniaxial tensile strip samples with interior or exterior notches were also designed based on this indicator. Conde et al. [46, 205, 271] obtained different interior-notched samples (Fig. 16) by applying

various geometry constraints, such as the aspect ratio of the sample, a varying initial interior notch, and a combination of the optimal geometries. Zhang et al. [186], instead, proposed a uniaxial tensile sample with a notch on each edge (Fig. 16) using the same indicator to iteratively maximize the strain heterogeneity.

The indicator could be slightly modified to analyze the stress states by including the triaxiality factor.

$$I_T = W_{r1} \frac{\text{Std}(TF)}{W_{a1}} + W_{r2} \frac{(TF)_R}{W_{a2}} + W_{r3} \frac{\text{Std}(\epsilon^{-p})}{W_{a3}} + W_{r4} \frac{\epsilon_{\max}^{-p}}{W_{a4}} + W_{r5} \frac{Av_{\epsilon}^{-p}}{W_{a5}} \quad (16)$$

where $TF = \sigma_H / \sigma_{eq}$, $(TF)_R = (TF)_{\max} - (TF)_{\min}$ and σ_H is the hydro-static stress. Thoby et al. [106] evaluated four different geometries for anisotropic mechanical behavior identification based on this indicator.

4.2.1.3 Topology-Optimization-Based Design Sigmund, et. al used topology optimization [272] to design the geometry of a specimen subjected to a uniaxial tensile test [273–276]. The objective is to find a specimen shape that offers a broad heterogeneous strain and stress state. They investigated different cost functions (traditional stiffness-based cost functions, along with multi-objective approaches mixing mechanical stability) and different optimization strategies to design specimens with high levels of heterogeneity. Topology optimization can provide a large design space and is very powerful in the structural optimization field. The team designed several complicated geometries. The technique, however, may impose a prohibitive computational burden and can sometimes generate unmanufacturable geometries.

4.2.2 Design Based on Sensitivity Analysis

Sample design strategies based on high strain and/or stress heterogeneity are useful for simultaneously identifying multiple parameters. However, since the stress and strain are intermediate variables in parameter identification, it is attractive to move one step forward by considering the sensitivity of the displacement or strain fields to each unknown parameter [277].

The earliest attempts at designing geometry by using sensitivity analysis are probably from Bos et al. [278] and Magorou et al. [279]. They aimed to simultaneously identify the elastic and viscoelastic mechanical characteristics (bending/torsion) of an embedded wood-based panel. To guarantee a good identification result, the bending frame size, the embedding positions, and the positions and the intensities of the applied stresses are optimized. In their work, the indicator related to the relative sensitivity of the displacement field to each parameter p_k is defined as

$$S_{p_k} = \left\| \frac{du}{dp_k} \right\|_2 / \left\| \frac{u}{p_k} \right\|_2 \quad (17)$$

where $\|\cdot\|_2$ is the Euclidean norm operator. When multiple parameters are identified, an increased identifiability of one parameter may lead to a decrease in the identifiability of the other one. It is therefore necessary to choose a fair standard as the cost function. A good way is to iteratively optimize the geometry by maximizing the smallest sensitivities to all parameters via FEA.

This concept is emphasized by Bertin et al. [40]. They further considered the DIC measurement uncertainty and the force uncertainty. The covariance matrix (equal to the inverse of the Hessian matrix) of the identified parameters due to image noise and force noise can be calculated. The geometry is then optimized by seeking the largest level of the smallest eigenvalue of the Hessian matrix. With this technique, the authors designed a cruciform specimen geometry (Fig. 16) with four fillets in the corners. The sensitivity-based cost function can also be combined with topology optimization under volume fraction constraints [280] or non-invasive computer-aided design (CAD) inspired optimization strategy [280] for test design.

4.2.3 Design Based on Simulated Full Identification

In FEMU, particularly classical FEMU, the DIC parameter settings, such as the subset size, the shape function, and the virtual strain gauge size, etc., significantly affect identification accuracy. The test design strategies mentioned previously do not take these error sources into account.

The design approach, which is based on full identification, has favorable accuracy. It involves first calculating the displacement maps using FEA with a set of predefined material model parameters. The displacement maps enable the generation of a set of virtual speckle or grid pattern images. FEMU can identify the material model parameters from these virtual images. The errors between the identified parameters and the predefined material model parameters can indicate the quality of the test design.

Rossi and Pierron [281] designed a Iosipescu test (see Fig. 15e) to identify the orthotropic plastic properties of composites. The fiber angle and a geometry parameter are the two design variables for the Iosipescu test. They proposed an indicator I_T based on the identification accuracy to quantitatively assess the test design:

$$I_T = \frac{1}{N_e} \sum_i \sqrt{\sum_k \omega_k \left(1 - \frac{p_k^{(i)}}{p_k^{(0)}} \right)^2} \quad (18)$$

where $p_k^{(0)}$ and $p_k^{(i)}$ are the k -th reference and identified parameter at i -th test; N_e refers to the number of tests; M denotes the number of the material model parameter and ω_k

is the weight used to control the importance of each parameter in test design. Minimization of this indicator yields an optimized test design.

This indicator reflects only the systematic error of the identified parameters. In a further development by Gu and Pierron, both systematic error and random error of the identified parameters [282] were combined into a single indicator, which is written as

$$I_T = \frac{1}{M} \sum_k \left(\left| 1 - \frac{p_k}{p_k^{(0)}} \right| + 2 \frac{\sigma_{p_k}}{p_k^{(0)}} \right) \quad (19)$$

where p_k and σ_{p_k} represent the identified parameter and the standard deviation of the identified parameter from 30 repeated identifications, respectively. This indicator is used to design the test for calibrating all the stiffness components of orthotropic composite materials using VFM. Four different tests were optimized and compared on the basis of this indicator. The four test configurations are short off-axis tensile test (Fig. 13a), short off-axis open-hole tensile test (Fig. 13e), Brazilian disc (Fig. 15d) and off-axis unnotched Iosipescu test (Fig. 15e), with certain design variables. They concluded that the short off-axis open-hole tensile specimen presents the best identification results.

4.3 Discussion on Test Design

The optimal sample geometry is highly dependent on the material, the material model and the material model parameters involved [42]. This entails a chicken-or-egg paradox. To accurately identify unknown material model parameters, the test needs to be designed based on a reliable estimation of the material model parameters, which is difficult prior to their identification. This review cannot offer a recommendation of a universal test design. There are various sound approaches to this dilemma, e.g., designing the test according to the material properties found in the literature or obtained through trial tests, or adopting the optimal test designs for similar materials. Even though, we can still try to design a serviceable test that will ensure adequate (though not optimal) performance for a given material in most scenarios.

Some geometries, while exhibiting high sensitivity to the material parameters in principle, might be impractical. Complex sample geometry may lead to high strain gradients. Measuring strain fields using DIC may result in relatively large errors when the strain gradient is high. Too many open holes in the sample may reduce the size of the effective measurement region. This is especially significant when subset-based DIC is used, where the regions near the ROI boundary are generally not measured. The manufacturing difficulty and accuracy of the designed geometry should also

be considered. We should therefore be wary of choosing an overly complex geometry.

The various material model parameters are not all equally important in a particular application. The most crucial material model parameters are expected to be identified with better accuracy, which necessitates designing the tests in conjunction with the final applications. The test design should match as close as possible to real life conditions to avoid extrapolations and uncontrolled discrepancies in material model calibration [227].

5 Kinematic Fields: Experimental Measurement and Numerical Simulation

Kinematic fields (displacement and strain fields) are the major inputs for FEMU. Robust inverse parameter identification requires rich, accurate and precise kinematic field information, though in certain applications only load–displacement curve is used [283]. In FEMU, the displacement and/or strain fields are usually measured by 2D-DIC [284], stereo-DIC, multi-view DIC, grid method, DVC, etc. These experimentally measured kinematic fields should be compared with the numerically simulated ones. This section provides a brief overview of the major kinematic field measurement techniques used in FEMU. The key issues affecting numerical simulation are also reviewed.

5.1 Experimental Measurements

In the early development stage of FEMU, various full-field measurement techniques were employed, such as DIC, random access video tracking [87], projection Moiré [179], electronic speckle pattern interferometer [285] and grid methods. In the last two decades, DIC techniques have become more accessible, easier-to-use, and more efficient. They are now the de facto standard kinematic field measurement techniques in FEMU. Several open-source DIC software tools (Ncorr [286], DICe [287], py2DICN [288], μ DIC [289], OpenCorr [290], MultiDIC [291], etc.), as well as commercial products (VIC [292], MatchID [293], DaVis [294], ARAMIS [295], DIC Elite [296], Istra4D [297], Cor-reli [298], etc.) are available. They can assist the researchers with strain measurement and, of course, inverse parameter identification.

In this section, multiple full-field deformation measurement techniques will be briefly reviewed along with their applications in FEMU. The focus is on the DIC-based techniques, i.e., 2D-DIC (local DIC, finite element-based global DIC, meshfree DIC), stereo-DIC, multi-view DIC, and digital volume correlation (DVC). Some special DIC techniques that are particularly suited for the identification of more challenging models are also reviewed. The special

DIC techniques reviewed here are high-speed DIC, high-temperature DIC, micro DIC and multi-scale DIC, as well as discontinuous DIC. A summary of the typical DIC-based full-field measurement techniques along with their pros and cons is given in Table 6. Some other non-DIC-based measurement techniques and their usage in FEMU are also briefly reviewed. These non-DIC-based measurement techniques include the grid method, Moiré Interferometry, etc.

For more information about DIC, we refer the readers to the book from Sutton et al., [82], the pioneers of DIC technique. That book covered the principal details of DIC, together with error estimation, applications, and practical considerations. International Digital Image Correlation society (iDICs) also produced a very detailed practice guide for DIC [121] that is a must-have reference for all DIC users.

5.1.1 2D-DIC

Two-dimensional digital image correlation (2D-DIC) [80] is an optical technique for full-field in-plane deformation measurements in planar samples using a single camera, see Fig. 17. The test sample should first have a high-contrast random speckle pattern applied [124], which will serve as the carrier of deformation information. A camera should be fixed to perpendicularly view the whole sample surface. During the loading process, the camera captures a set of high-contrast and low-noise images of the sample surface. Matching the images captured before the deformation to those taken afterwards using an image correlation algorithm yields the full-field displacement fields. The strain fields can then be obtained with some post-processing techniques [126]. In some cases, a further filter can be applied to the measured displacement or strain fields (only when the gradient is small) to reduce the noise. Azzouna et al. [299] shows that the filtering can be beneficial for better parameter identification, while the filtering of the simulated data may not be beneficial. Based on the different algorithms, 2D-DIC can be primarily classified into local DIC, finite element based global DIC (FE-DIC) [300, 301], and the recently proposed meshfree DIC (MF-DIC) [302, 303].

Local DIC [121, 284] (Fig. 17b) is carried out by first selecting a region of interest (ROI, the blue region in Fig. 17b) on the reference image (the image captured before deformation). This is followed by specifying a grid of points of interest (POIs, the red dots in Fig. 17b) in the ROI. Each POI (see the red cross in Fig. 17b) is matched to the deformed image independently solely by using the image intensity information in a small subset surrounding it. The matching of a subset is based on the assumption of image intensity conservation within each subset. The deformation in a small subset, in most cases, is assumed to be continuous. It can be described by a continuous first- or second-order polynomial shape function.

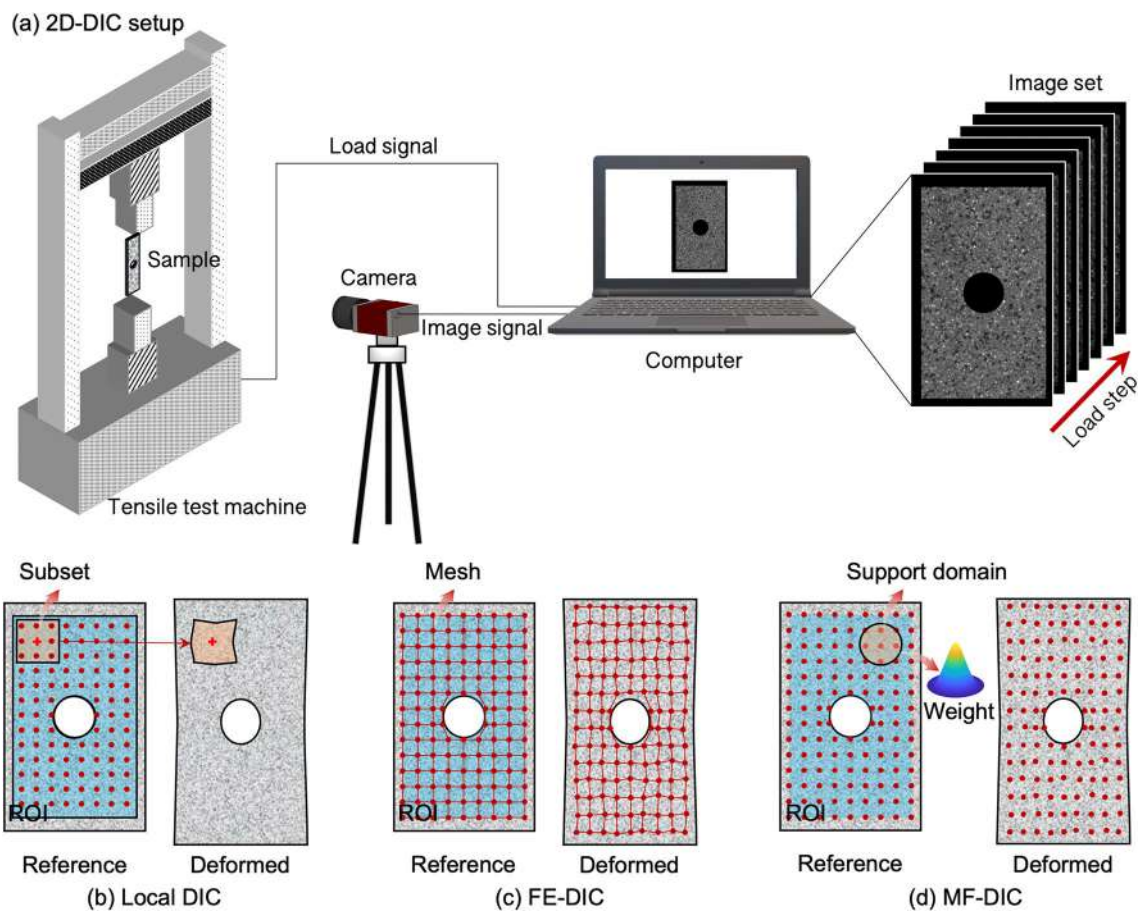


Fig. 17 Schematic diagram of a 2D-DIC. **a** 2D-DIC setup and **b–d** principal diagrams of different DIC algorithms: **b** local DIC, **c** FE-DIC and **d** MF-DIC

Table 6 Comparison of different DIC-based kinematic field measurement techniques

Method	Application scenario	Advantages	Disadvantages
2D-DIC [19, 56, 258, 306]	In-plane surface deformation measurement of planar samples	Easy to use Good accuracy	In-plane measurement of planar sample Huge error from out-of-plane translation
Stereo-DIC [38, 178, 337]	3D surface deformation measurement	3D surface measurement Easy to use Good accuracy	Needs additional camera calibration No through-thickness strain information
Multi-view DIC [44]	Multiple-surface/panoramic/through-thickness measurements of complicated sample surfaces	3D surface measurement Rich information on several surfaces Good accuracy	Expensive Difficult to calibrate
Digital volume correlation [223, 334, 336]	3D internal deformation measurement	Internal 3D measurement Rich information	Highly expensive Requires internal random features Quasi-static measurement Time-consuming Computationally expensive

FE-DIC (Fig. 17c) first generates a mesh (the red mesh) on the reference image. The nodes (the red dots in Fig. 17c) of the mesh are the POIs. All POIs are then matched to the

deformed image simultaneously by utilizing all the image intensity information in the ROI. The deformation within

the ROI is constructed by a shape function from the whole mesh, as in FEA.

MF-DIC [302, 303] (see Fig. 17d) is inspired by the meshfree method [304] in computational mechanics. It starts by generating a set of scattered nodes (the red dots in Fig. 17d) instead of a mesh on the reference image. A C^1 -continuous shape function at any point is constructed from the scattered nodes. Only the nodes in a small support domain (Fig. 17d) surrounding to a point contributes to the shape function construction of this point. In the support domain, the nodes closer to the calculation point have more weight (see the weight shape in Fig. 17d) for constructing the shape function. This is helpful to reduce the systematic error in shape function. The MF-DIC algorithm is a global DIC algorithm with a C^1 -continuous shape function, which means that strain fields can be analytically calculated from the displacement fields.

Local DIC has the advantages of high efficiency and good balance between spatial resolution and measurement resolution [305]. It is the mainstream in both academic research and engineering applications [237]. Next is FE-DIC, with the major benefit that it employs the same mesh generation and shape function construction approach as FEA and can therefore help to bridge the gap between computational mechanics and experimental mechanics. This advantage is especially attractive in the scenario of FEMU. Similarly, MF-DIC benefits from being closely related to the meshfree method in computational mechanics. Additionally, it exhibits an excellent balance between spatial resolution and measurement resolution compared to the state-of-the-art DIC algorithms [303].

2D-DIC is one of the most popular deformation measurement techniques in FEMU [209], reason being that the samples are mostly flat sheet samples subjected to in-plane loading (uniaxial tensile, biaxial tensile, three-/four-point bending, fracture test, etc.). Additionally, 2D-DIC features a good balance between cost, simplicity, efficiency, measurement resolution and spatial resolution. Finally, perpendicular image recording can reduce the effort required to align DIC and FEA data. In most cases and applications, local DIC can be used [92, 158, 256]. FE-DIC can be adopted in general applications [306], in fracture parameters identification [19, 307], and has been used in some studies to avoid information loss near the sample edge [258]. Vargas et al. [56] also used FE-DIC to detect the crack path in a mortar sample by resorting to the correlation residuals. The detected crack path enables better determination of the CZM parameters.

It must be noted that 2D-DIC can only measure in-plane deformation of planar samples. A small out-of-plane movement along thickness direction may lead to considerable in-plane strain error [308]. A highly recommended way to eliminate the strain error from out-of-plane translation is to replace the conventional pinhole camera with a telecentric

lens [308, 309]. An alternative way is to compensate the out-of-plane displacement effect in the cost function in FEMU [310].

5.1.2 Stereo-DIC

Stereo digital image correlation (Stereo-DIC, referred to also as 3D-DIC) [311, 312] is a technique to measure the 3D surface deformation of curved samples. It is based on binocular stereovision [313] and image matching. In this method, the speckled sample surface is simultaneously captured from two different views before and after deformation. The disparity fields between the two views in all states are measured using spatial matching. They are used for 3D surface shape reconstruction [314] after an accurate stereovision calibration [315, 316]. The 3D surface displacement fields are tracked using temporal matching [317] among the images captured by one camera. Local DIC, FE-DIC, and MF-DIC algorithms can all be easily generalized to stereo DIC, with their typical features being preserved.

The stereo-DIC system generally involves two synchronized cameras. A more affordable alternative is the single-camera stereo-DIC system [318]. The single-camera stereo-DIC splits the view of a single camera into two views using some view-splitting setups, such as a four-mirror system [319] or biprism [320]. It therefore provides the disparity required for stereo-DIC measurements. The single-camera stereo-DIC system may sacrifice in spatial resolution and measurement accuracy. However, it benefits in several aspects. First and most importantly, it is cost friendly and easy to implement. It can also avoid the camera synchronization issue [321] in dynamical measurement by using only one high-speed camera.

In most cases, the aim of stereo-DIC application is to provide a more accurate measurement, even when only in-plane deformation is needed [42, 200]. The enriched shape and displacement information along the third dimension is useful, especially in parameter identification tasks that require out-of-plane displacement fields. For instance, Wang et al. [38] proposed a stereo FEMU approach that integrates stereo-DIC into FEA for anisotropic plastic parameters identification from a common 3D Erichsen bulge test. The identified parameters agree well with the parameters fitted from standard uniaxial tensile tests. Pottier [264] identified the orthotropic elastoplastic material parameters from a hemispherical punch test on a specially designed sample geometry. In this task, the out-of-plane displacement field measured by stereo-DIC is the key part of parameter identification. Another parameter identification task that requires stereo-DIC is indentation. It has been used to identify the hyperplastic parameters of rubber [178] and soft tissues [118].

5.1.3 Multi-view DIC

Stereo-DIC can only measure a small part of the sample surface. In some cases, the enriched deformation information at different parts of the sample surface is of interest in inverse parameter identification, in which case, multi-view DIC [322, 323] that involves more than two cameras (or virtual cameras) can be adopted. The multi-view DIC can simultaneously measure several different parts of the sample surface from multiple views. Rossi et al. [245] proposed simultaneously measuring the displacement on the front and back surface of a sheet metal sample using two stereo-DIC systems, respectively. The volume displacement field inside the specimen was reconstructed using interpolation from the displacement field measured on the two surfaces. The volume displacement fields enable more accurate calibration of the hardening parameters of Swift's law. Denys et al. [44] used two stereo-DIC systems to simultaneously measure the deformation on the front and thickness surfaces of a thick sample. Much richer deformation information can be simultaneously obtained in lateral, longitudinal, and through-thickness directions. The 3D anisotropic yield surface of thick S690QL high strength steel specimen can thus be identified with better accuracy.

The most significant limitations of multi-view DIC are the high cost, complex synchronization, and the difficulty of calibrating the multi-camera system. A recent development is the mirror-assisted multi-view DIC technique [324], which brings a cheap, simple and accurate alternative to the standard multi-view DIC. Mirror-assisted multi-view DIC uses only a standard two-camera stereo-DIC system and two mirrors. The implementation complexity and cost are almost the same as a single two-camera stereo-DIC system. This technique can effectively measure panoramic shape, displacement and strain fields in a global coordinate system. It has been used successfully to measure the panoramic shape deformation of cylindrical bar samples [325, 326], in-vivo human arm [327], and cubic wood aerogel [328]. It was also used to measure the dual-surface [329] and through-thickness [330] deformation of sheet samples. We believe it can contribute to the parameter identification by providing an extra through-thickness strain field and volume strain information, in a simple and accessible way.

5.1.4 Digital Volume Correlation

2D-DIC and stereo-DIC provide only the deformation and/or shape information on sample surface. However, the surface deformation may not be fully representative of the sample deformation with significant heterogeneity inside. This limitation is particularly obvious when studying the 3D local interactions of complicated composite materials. An attractive option for mitigating this issue is DVC [331], which

can measure the 3D internal displacement or strain fields. DVC is a direct generalization of 2D-DIC from 2D space to 3D space. It measures the internal 3D kinematic fields by matching the volume images of a sample before and after deformation.

One of the most challenging tasks in DVC is to get high-quality volume images with rich, low-noise, and random contrast distribution. The image contrast, in most cases, is from the random microstructure inside the materials themselves, which might be unsatisfactory in a lot of cases. The volume images could be recorded by X-ray Computed Tomography [331], magnetic resonance imaging [332], etc. The DVC algorithm for volume image registration can be directly extended from 2D-DIC to 3D space. The extra data dimension generally demands much more computational time, which could be effectively accelerated by using parallel computing [333].

DVC measurement is of great value for more accurate inverse parameter identification. It is especially beneficial for the identification of heterogeneous materials. The DVC measurement can contribute in the form of (i) a high-accuracy microstructure model for FEA; (ii) Dirichlet displacement boundary condition for FEA; (iii) the internal deformation information of heterogeneous material.

Vargas et al. [223] proposed to use DVC to track the realistic crack surface inside an alumina castable refractory with mullite-zirconia aggregates in a WST. The crack path is inputted into a PPR CZM model to numerically simulate the mechanical response of the sample. In FEMU, the cost function was constructed from the difference of the numerically simulated kinematic fields and the DVC-measured kinematic fields. By iteratively minimizing the cost function, the cohesive strength and fracture energy in the CZM can be effectively identified. The parameters thus identified have a nonnegligible difference compared to the parameters identified under the assumption of a flat crack surface. This result demonstrated the necessity of accurate internal crack surface detection with DVC.

Hachem et al. [334] used DVC to measure the 3D deformation of a wood sample between wet and dry conditions with the aim of characterizing the microscopic hygro-mechanical property of spruce wood. DVC not only provided the experimental displacement fields in the cost function, but was also used to extract the Dirichlet boundary condition for numerical modeling. Chen [335] identified the non-linear elastic properties of a small graphite specimen by using the 3D displacement fields measured by DVC. The displacement fields measured by DVC are also used in other FEA. Buljac et al. [336] conducted in-situ microscale DVC measurement of a spheroidal graphite cast iron material. The DVC measurement can yield a realistic microstructure model, the Dirichlet boundary condition, and the 3D displacement fields in the cost function of FEMU. The plastic behavior of the

Table 7 High-speed DIC and its applications in FEMU

Reference	Year	Models	Materials	Frame rate (fps)
[341]	2007	Viscoplastic model	Mild steel	100,000
[343]	2014	Plastic behavior	Aluminum plates	25,000
[342]	2019	Elastoplastic model and Contact law	Polymer adhesive joint	–
[122]	2022	Strain rate hardening model	Fiber reinforced polymers	–

ferritic matrix, modeled by Ludwik's law and Von Mises yield criterion, was calibrated via integrated DVC [336]. The ductile damage mechanism can be analyzed through numerical simulation based on the realistic 3D model.

5.1.5 Special DIC

The advanced DIC technologies, combined with specialized photography equipment and/or specifically designed algorithms, can push the limits of DIC to enable more challenging parameter identification tasks. These specialized DIC techniques increase the potential of FEMU to identify more challenging material models. High-speed photography, for instance, enables DIC for dynamic measurements. The ability to produce high-contrast and stable speckle pattern images facilitates the implementation of high-temperature deformation measurement. Microscopic deformation can be measured using in-situ microscopic tests, if high-quality (sharp, high contrast, low noise and with random speckle pattern) microstructure or nanostructure images are captured. Another challenging task is the identification of fracture properties. In this case, the discontinuous deformation fields can be measured by modifying the continuous DIC algorithm. Here we focus mainly on high-speed DIC, high-temperature DIC, micro- multi-scale DIC, and discontinuous DIC. Constitutive parameter identification using these special DIC techniques is also reviewed.

5.1.5.1 High-Speed DIC DIC techniques based on high-speed photography [ranging from tens to millions of frame per second (fps)] can help to capture the transient mechanical response [338, 339]. The challenges of high-speed DIC are mainly the high-cost and difficulty for camera synchronization in stereo-DIC, which could be partially improved by the single-camera stereo-DIC [312]. The other challenge is the large data including thousands to millions of images. Data compression technique can help on saving the data [340].

Kajberg and Wikman [341] calibrated the viscoplastic material parameters of a mild steel at high strain-rates. The dog-bone shaped specimens were exposed to compression loading in a split Hopkinson pressure bar arrangement. The speckle pattern images were recorded by a high-speed camera at a frame rate of 100,000 fps. Louar et al. [122]

identified the strain rate hardening model parameters for in-plane tensile and shear strengths of glass fiber reinforced epoxy from the dynamic response measured by a high-speed stereo-DIC system. The identification showed an increase of tensile and shear strengths with the strain rate, which matches well with the literature. Janin et al. [342] characterized adhesive joints under multiaxial and dynamic loading conditions. Displacement jumps at the adhesive center are measured by high-speed DIC. Spranghers [343] employed a high-speed stereo-DIC system to measure the dynamical deformation of aluminum plates subjected to a sudden blast load at a frame rate of 25,000 fps. Three rate-dependent plasticity models were calibrated on the basis of the discrepancy between the DIC-measured displacements and their numerical counterparts. Corallo et al. [344] developed a high-speed hydraulic bulge test for sheet metal. They highly suggest using advanced identification techniques, such as FEMU, to calibrate and validate complex, strain rate dependent plasticity models. A summary of high-speed DIC applications in FEMU is presented in Table 7.

5.1.5.2 High-Temperature DIC Ordinary DIC setups may progressively fail at elevated temperature (e.g., exceeding 600°) due to the decorrelation effect from image overexposure and heat flux [345]. A common way to deal with this issue is to combine a strong short-wavelength light source and a corresponding narrow band-pass filter [346, 347]. This significantly reduces the energy flux from the sample heat radiation to the camera sensor, allowing high-contrast imaging at a temperature of over 2600 °C [348]. The time-gated active imaging technique based bandpass filtering and gated single-photon imaging techniques is also a practical solution [349, 350].

Zhao et al. [129] took advantage of the high-temperature measurement to identify the thermo-mechanical parameters of Nickel-Based single crystal superalloys at up to 1000 °C. In their work, high-temperature deformation measurement is facilitated by a blue light source and a corresponding blue light filter. Five parameters were identified simultaneously, including the three isotropic elastic parameters and two anisotropic coefficients of thermal expansion.

In cases where the sample is heated directly via Joule effect by imposing a direct current, Gao et al. [231] measured the strain field without using an extra light source at

Table 8 High-temperature DIC and its applications in FEMU

Reference	Year	Models	Materials	Temperature (°C)
[229]	2017	Elastic + thermal expansion	Ni-based superalloy GH4169	300, 500, 700
[351]	2020	Temperature-dependent Bonora damage model	X12 ultra-super-critical rotor steel	1100
[231]	2022	Elastic + viscoplastic + Arrhenius law	Nickel-based superalloy In718	1000
[129]	2023	Elastic + thermal expansion	Single-crystal nickel-based superalloy	800 to 1100

temperatures from 800 to 1100 °C. The FEA model was built with the displacement boundary condition measured through DIC and temperature distribution obtained using IR field imaging. The parameters in a temperature-dependent elastic–viscoelastic behavior model were calibrated from the cost function based on force. Liu et al. [351] measured the displacement fields at up to 1100 °C using stereo-DIC with a blue light source and a corresponding narrow band-pass filter. Four damage parameters of ultra-super-critical rotor steel in the Bonora damage model were identified at elevated temperature.

Dong et al. [229] measured the deformation field of the Ni-based superalloy GH4169 at 300, 500, and 700 °C. They used a bi-telecentric lens and blue-light active imaging to get high quality images at elevated temperature. They used IDIC to identify multiple thermo-mechanical parameters, which were then used to decouple the thermo-mechanical deformation. A summary of the applications of high-temperature DIC in FEMU is presented in Table 8.

5.1.5.3 Micro DIC and Multi-scale DIC Feeding DIC with in-situ microscopic images can extract the deformation fields of microstructures. Serving as the input to FEMU, the measured displacement fields can assist with calibrating the micromechanical behavior of a material. Bertin et al. [352] manufactured a micro-specimen of IF-steel using the focused ion beam technique. The sample has a size of $12 \times 4 \mu\text{m}$ (with two distinct grains in the sample). The random pattern was applied by platinum deposition for image matching. The material parameters of a crystal plasticity model were then identified using IDIC. The boundary condition in FEA is determined by DIC measurement at micro-scale.

Gebhardt et al. [261] applied a micro-scale speckle pattern to ductile cast iron using a focused ion beam. DIC was used to measure the displacement fields at micro-scale using the scanning electron microscope (SEM) images from in-situ tensile tests. To reliably identify the plasticity parameters of ferrite in ductile cast iron, a micromechanical model was built based on the microstructure distribution. The boundary condition for FEA is obtained from a macroscopic finite element simulation (the model parameters were also determined using inverse identification by assuming a homogeneous and isotropic material).

Both FEA and DIC require achieving a tricky compromise between spatial resolution and uncertainty. Passieux [55] proposed using multi-scale DIC to measure the displacement fields on the sample surface using two cameras with different spatial resolutions. In the region with high strain heterogeneity, local images with higher magnification were captured. A lower-magnification camera captured the overall sample surface. The measured displacement fields can help determining the boundary condition for FEA. They proposed an automatic and accurate repositioning algorithm based on image registration. This algorithm can fuse the kinematic fields measured at two different scales. This results in a good balance between spatial resolution and uncertainty that allows more accurate parameter identification.

5.1.5.4 Discontinuous DIC One challenging task for FEMU is identifying the parameters in a fracture mechanics model. The general DIC algorithms are inherently continuous. They inevitably suffer significant measurement errors close to the discontinuous deformation region. Consequently, significant parameter identification errors will be introduced in FEMU. Several kinds of discontinuous DIC methods [353], e.g., subset-splitting local DIC [354], extended-DIC [355], element-removal global DIC [356], etc., have been developed to accurately measure the deformation fields in fracture mechanics scenarios. The subset-splitting algorithm separates the discontinuous element into two parts based on the matching error, where the deformation is continuous within each part. Extended-DIC enriches the regular global-DIC with more degrees of freedom for the element sampling discontinuities. The new shape function is then able to adequately describe the discontinuous deformation. In element-removal global DIC, good matching accuracy near the crack is achieved by iteratively finding and removing only the elements spanning the discontinuity.

5.1.6 Grid Method

The grid method is an advanced non-interferometric white-light technique for accurate in-plane displacement and strain field measurements. It involves processing the images of a sample surface that have regular markings applied. The major advantage of this method is the good compromise between spatial and measurement resolution. This advantage

is particularly important in case of small deformation measurements.

However, some inherent limitations make the grid method less popular than DIC. First and foremost, it requires the application of regular features to the sample surface using a specific instrument. This method is mainly suitable for in-plane deformation measurement of planar samples. Additionally, it is challenging to deal with very complicated deformation fields. More details on the grid method can be found in a review paper [85].

The grid method has been used for parameter identification in FEMU since 1996. Mahnken and Stein [86] used the grid method to measure the displacement fields at a set of grid points. The SSD between the simulated and measured displacement at several points served as the cost function for parameter identification. The strain fields can be easily differentiated from the displacement maps [268, 357], processed by a some smoothing operation.

5.1.7 Other Methods

In the era of the pioneering work by Meuwissen et al. [87], contemporary full-field measurement techniques were not that popular. The authors placed 120 retro-reflective markers onto the sample surface. A camera captured images of the sample surface at each loading step. The displacements of these markers were measured by an image processing algorithm. The difference between the measured and numerically simulated displacement fields enabled the iterative identification of the unknown parameters in elastoplastic models.

Moiré photography is a method used primarily to measure in-plane deformation. It is implemented by first applying a grating pattern onto the sample. Images of the sample before and after deformation are superimposed to generate the Moiré fringe pattern for full-field displacement measurement. The method precision is moderate compared with DIC. In 2005, Genovese et al. [179] employed this technique to assist in the calibration of a two-parameter Mooney–Rivlin (MR) hyperplastic model using FEMU.

Moiré Interferometry [358] and electronic speckle pattern interferometer [359] are two more deformation measurement techniques suitable for inverse parameter identification, thanks to their advantage of high accuracy. They are both interferometric techniques and they place high demands on the experimental environment. As a result, they are less popular in experimental mechanics, especially in non-laboratory environments.

5.2 Numerical Simulation

Numerical simulation of the mechanical response of a specimen is powerful and efficient. It provides part of the input information for the FEMU algorithm and is consequently

one of the most crucial steps in FEMU. Additionally, numerical simulation accounts for most of the computational resource usage during FEMU optimization. Numerical modeling requires careful preparation to ensure an accurate and efficient FEMU implementation. FEA involves several key choices when applying FEMU: the boundary conditions, the meshes and the solvers. Properly building the FE model therefore requires expertise.

5.2.1 Boundary Conditions

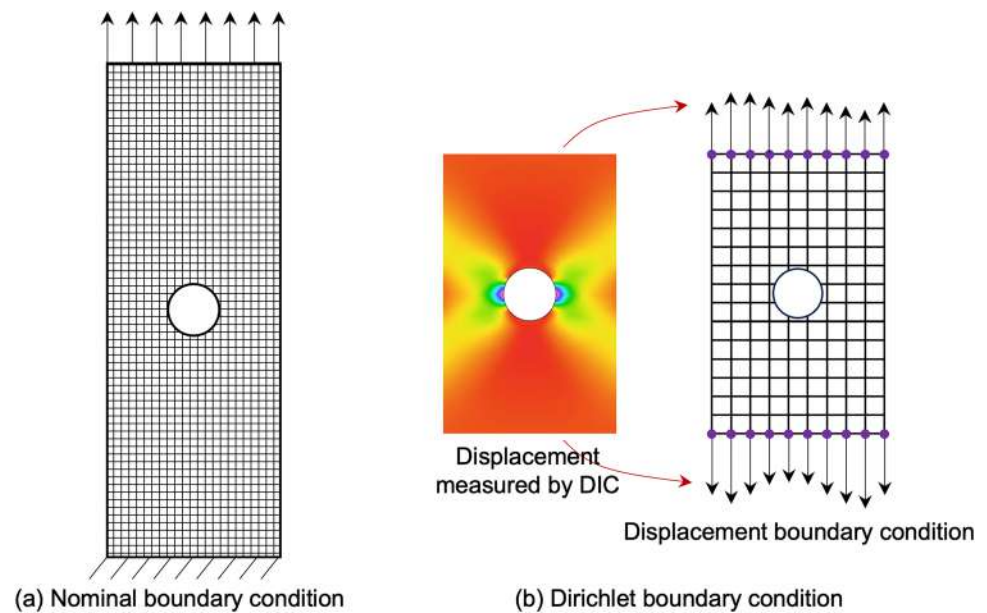
The boundary conditions (e.g., displacement, force, or temperature boundary condition) in FEA can dramatically affect the FEMU identification results. Both force and displacement boundary conditions are widely adopted in FEMU. The displacement boundary conditions can either follow the normal value from the experimental setting or be extracted from the displacement fields measured by DIC.

The force boundary condition applies the force output from the test machine to the FE model. The force boundary condition may lead to instability in Finite Element Analysis (FEA) if the initial estimate of the material parameters deviates significantly from the actual ones. Suppose, for instance, that the initial value for the Young's modulus is much lower than the actual one: the resulting deformation may be extremely large, leading to simulation instability. An additional caveat is that a force-driven simulation will necessarily always be only an approximation of the reality since the exact force distribution in the gripping area is unknown.

The displacement boundary condition can mitigate this issue by constraining the deformation. However, the identification must have force information, which could be included in the cost function. Likewise, a nominal displacement boundary condition (Fig. 18a) can hardly match the real experiments. An error in the displacement boundary condition may result in a substantial deterioration in the accuracy of the identified parameters [360], especially when the cost function is based on displacement fields.

We can resort to the displacement fields extracted using DIC or DVC to set the Dirichlet boundary conditions [19, 64, 133, 224, 307, 352, 361, 362] (Fig. 18b) for FEA. Zaplatić et al. [361] compared the influence of five types of Dirichlet boundary conditions on the calibrated material parameters using FEMU. A requirement of Dirichlet boundary condition is that the ROI measured by DIC should cover the FEM mesh [363]. This is a good solution to obtain a more accurate simulation [364] by mitigating the impact of experimental imperfections [47], such as rigid-body translation of the sample due to compliance of the test machine or imperfect gripping systems (slipping of the sample in the grips). This is an effective strategy to improve the accuracy and robustness of FEMU. It is also beneficial for improving the simulation efficiency, since only the measured ROI needs

Fig. 18 Boundary condition in FEMU, **a** the nominal boundary condition from the test machine, **b** the Dirichlet boundary condition obtained by the full-field displacement measurement technique



to be simulated with FEA. It must be noted that directly applying the Dirichlet boundary condition is inadvisable due to the measurement noise. The recommendation to improve the robustness of parameter identification is instead to apply a smoothing operation to the measured displacement boundary condition [68]. This Dirichlet boundary condition can eliminate the machine compliance in the tests. The final caveat when using DIC is that the approach of directly imposing the measured displacement boundary conditions is confined to thin specimens in which the through-thickness variation of the displacement field can be safely ignored.

The issue of inaccurate boundary condition can also be addressed through design of the test itself—for instance by ensuring that the material state in the ROI is not sensitive to the modelling approach used for the boundary conditions.

5.2.2 Mesh Quality

Mesh quality and density have a strong impact on the efficiency and accuracy of the modeling and are consequently also of major importance in FEMU [119, 336, 365]. A finer mesh ensures a more accurate simulation but comes at the cost of lower efficiency. Additionally, most of the specimens tested in the context of FEMU are sheet samples. These samples, if thin enough, could be efficiently simulated with a 2D mesh.

For thicker samples, a 2D mesh may yield a nonnegligible error. In that case, the use of 3D solid elements that can model through-thickness strain heterogeneity is mandatory. Using 3D elements leads to higher computational demands for FEMU, in which the FEA model needs to be evaluated multiple times in several iterations. Simulation efficiency must be taken into consideration. It is recommended to do

a mesh convergence evaluation prior to the simulation; a mesh with a good balance between efficiency and accuracy can then be built.

5.2.3 Numerical Simulation Solver

In material testing, a non-linear static analysis is generally adequate. For dynamic or modal testing, however, the solver is completely different. In ductile damage modelling, an explicit dynamic analysis is usually used, even for static problems. In FEMU, it is important that convergence problems in FEA are avoided to prevent premature termination of the identification.

FEA is undoubtedly the dominant numerical simulation approach in FEMU, due to the numerous available FEA solvers. Some other numerical simulation methods, such as the boundary element method (BEM) [57, 366], is still superior in some applications, however. BEM is accurate in problems where high displacement gradients occur. It is therefore suitable for identifying the fracture mechanics parameters. In light of the advantages of BEM, Ferreira et al. [58] used this numerical simulation method to inversely extract the Young's modulus and the CZM parameters.

6 FEMU Optimization

Once the experiments and simulations have been conducted, parameter optimization follows. There are several key factors to consider in parameter optimization, the most significant being the cost function, sensitivity analysis, data fusion, optimization algorithm, optimization strategy, initial parameter estimates, and convergence criteria.

The cost function is the mathematical cornerstone of the inverse identification problem and should be sensitive to changes in the material model parameters while being robust to data noise. Data fusion denotes the fusion of experimental and simulated data. The optimization algorithm and optimization strategy are designed to iteratively find the optimal parameters efficiently and accurately. A good initial estimate of the parameters can significantly speed up the optimization. The optimization should stop when certain stop criteria are satisfied. In this section, these aspects are reviewed in detail.

6.1 Cost Function

The cost function is at the very heart of FEMU, being the mathematical formulation of the inverse identification problem [367]. It can be the dominant factor in the identification performance (uncertainty, efficiency, etc.), since it is highly correlated with sensitivity. The cost function is typically constructed as the SSD between the measured and simulated results of one or multiple physical responses. A good cost function can be constructed by applying the following criteria:

- The cost function should have high sensitivity to every unknown material parameter. The parameters must not be highly correlated.
- Cost functions are generally constructed from the physical responses. A prerequisite for these physical responses is that they can be easily simulated and measured.
- More data (e.g., images at multiple load steps) with a high signal-to-noise ratio (SNR) can effectively reduce the uncertainty of the identified parameters. However, it will also increase the calculation time [70, 119].
- For a more robust parameter identification, full advantage should be taken of several physical responses in a single cost function.
- If the test is repeated for several times, all experiments should have equal opportunity to be optimized [368], emphasizing that the optimization should not depend on user preference on the tests.
- Different physical responses in the cost function may have different units, but the difference in the units should not have significant effects on parameter identification [369]. This can be achieved by scaling, weighting or normalizing each term in the cost function. In most cases, the mean value and uncertainty vary significantly among the different physical responses at different loading conditions. Scaling and normalization strategies can also help to balance the importance of the cost function at different states.
- The material model parameters should generally be constrained so that non-physical artefacts are avoided—see

for example the work of Abedini et al. [370]. Their range can be constrained by adding physical regularization terms into the cost function.

The cost functions mainly fall into the following categories: global cost functions, local cost functions, hybrid cost functions, parameter-regularization cost functions and the multi-physics cost functions. The global cost functions involve the global responses such as force, geometry quantities, etc. The local cost functions are constructed from the field responses, such as displacement or strain fields. The hybrid cost functions are the weight combination of local and global cost functions.

Beyond that, the parameter-regularization cost functions involve regularization terms related to the identified parameters. These terms could be priors, penalties, or parameter constraints. The aim of the regularization is to constrain the values of the identified parameters to keep them in the range of plausibility. There are some other cost functions used in the identification of some challenging mechanical models, such as thermomechanical models. Those cost functions should include multi-physics responses. The typical cost functions are summarized in Table 9 for comparison.

6.1.1 Global Cost Functions

6.1.1.1 Cost Function Based on Force Response As the name indicates, global cost functions are formulated from the global physical responses. The most common global response used in FEMU is force. The simplest global cost function is the difference [64] between the applied loads and the simulated counterparts, see Eq. (20). FEMU based on this cost function is denoted as FEMU-F and also called the force balance method, the input residual method, or the equilibrium method [239]. This cost function is particularly helpful in identification tasks where the displacement or strain maps are not measured. Giton [64], for example, proposed to identify the hyperelastic parameters from the cost function in Eq. (20).

$$\chi_{\text{FEMU-F}}(\mathbf{p}) = \frac{1}{N_S} \sum_t^{N_S} (F_t^{\text{EXP}} - F_t^{\text{FEA}}(\mathbf{p}))^2 \quad (20)$$

where N_S denotes the number of load steps and t the data acquisition step. F_t^{EXP} and F_t^{FEA} are the forces measured in the real experiment and FEA, respectively. \mathbf{p} the parameter vector needed to be identified. This cost function can be refined by adding normalization to each term, see Eq. (21). It allows equalizing the importance of the data at different acquisition steps [56, 224, 351, 371]:

Table 9 Comparison of different cost functions

Cost function	Unique features	Common features
<i>Global cost functions</i>		
FEMU-F	Equal importance of all points at all stages Sensitive to systematic error	Suitable for cases with strain concentrations Higher uncertainty due to lack of field information
FEMU-FN	Balances the importance of each load stage according to certain standard	
FEMU-FLN	Includes crack length feature	Higher uncertainty due to lack of field information
FEMU-FCN	Includes the notch opening displacement feature	Suitable for fracture mechanical model identification
<i>Local cost functions</i>		
FEMU-U	Sensitive to rigid-body motion Suitable for cases with strain concentrations	Robust identification of multiple parameters Force information is required for modulus identification
FEMU-ε	Low SNR Sensitive to strain concentrations	Equal importance of all points at all stages
FEMU-UN	Sensitive to rigid-body motion Suitable for cases with strain concentrations	Weights the importance of all points according to certain standard
FEMU-εN	Low SNR Sensitive to strain concentrations	Force information is required for modulus identification Robust identification of multiple parameters
<i>Hybrid cost functions</i>		
FEMU-UF	Sensitive to rigid-body motion	Robust identification of several parameters
FEMU-εF	Low SNR Sensitive to strain concentrations	Equal importance of all points at all stages
FEMU-UFN	Sensitive to rigid-body motion	Robust identification of multiple parameters
FEMU-εFN	Low SNR Sensitive to strain concentrations	Balances the importance of all points according to a certain standard
<i>Parameter-regularization cost functions</i>		
FEMU-FR	Suitable for cases with strain concentrations Higher uncertainty	Control parameters range Equal importance of all points at all stages
FEMU-UR	Robust identification of multiple parameters Sensitive to rigid-body motion Force information is required for modulus identification	
<i>Multi-physics cost functions</i>		
FEMU-UT	Includes the temperature field	Suitable for thermomechanical model identification
FEMU-UFT	Includes the temperature field and force Suitable for cases with strain concentrations	Sensitive to rigid-body motion

Note 1: Different FEMU methods are notated as “FEMU-*” according to their cost functions, where “*” is the combination of the following parts: U: displacement field information, ε: strain field information, F: force information, N: normalization to the physical response in the cost function, R: regression term for all examined parameters, T: temperature field information, L: crack length feature, C: notch opening displacement feature

Note 2: The normalization term could be either uncertainty-based (e.g., $\text{Std}(u_{r,i}^{\text{EXP}})$, $\text{Std}(\epsilon_{r,i}^{\text{EXP}})$) or value-based variables (e.g., $u_{r,i}^{\text{EXP}}$, $\epsilon_{r,i}^{\text{EXP}}$). The uncertainty-based normalization term is recommended when the systematic error is small. The value-based normalization term is suitable in cases where the systematic error in the measurement is more significant

$$\chi_{\text{FEMU-FN}}(\mathbf{p}) = \frac{1}{N_S} \sum_t^{N_S} \left(\frac{F_t^{\text{EXP}} - F_t^{\text{FEA}}(\mathbf{p})}{F_t^{\text{NORM}}} \right)^2 \quad (21)$$

where F_t^{NORM} is a normalization value. One of the most used normalization terms F_t^{NORM} is the load uncertainty, σ_F [56, 224], while the alternative could be $F_t^{\text{NORM}} = F_t^{\text{EXP}}$ [372]. FEMU based on this cost function is here referred to as FEMU-FN. This cost function makes more use of data with higher SNR. If the load cell has the same load uncertainty

during loading, FEMU-FN normalized by the load uncertainty σ_F is equivalent to FEMU-F. The FEMU-FN cost function proved its effectiveness by identifying the CZM parameters of mortar [56] and castable refractory [224].

The global cost function can also be formulated from the geometry quantities [365], termed as FEMU-G in this review. Touzeau et al. [365] first segmented the sample images into binary images. Then, they measured a geometry quantity as the n -order moment of the geometry centered to

a given point. The FEMU-G cost function is then defined as the SSD between the geometry quantities in experiments and simulation. Satošek et al. [263] defined the FEMU-G cost function as the difference between the measured and simulated pile-up heights in an indentation test and then identified the parameters related to the out-of-plane shear properties.

6.1.1.2 Cost Function Including Fracture Mechanics Information Doitrand et al. [72] proposed to identify the CZM parameters from a WST of refractories. The tortuous crack path on the sample is detected by thresholding the strain gradient measured by DIC. The experimentally measured kinematic fields are unlikely to match perfectly with the numerical simulation. This mismatch is especially significant near the crack tip, where the strain concentration exists. This is a challenge for robust parameter identification. Instead, the authors proposed a new cost function. This cost function is a combination of the normalized reaction force and the crack length and is referred to as FEMU-FLN:

$$\chi_{\text{FEMU-FLN}}(\mathbf{p}) = \frac{\omega}{\sigma_F^2 N_S} \sum_t^{N_S} (F_t^{\text{EXP}} - F_t^{\text{FEA}}(\mathbf{p}))^2 + \frac{(1-\omega)}{\sigma_{\text{NOD}}^2 N_L} \sum_m^{N_L} (L_m^{\text{EXP}} - L_m^{\text{FEA}}(\mathbf{p}))^2 \quad (22)$$

where σ_{NOD} is the standard deviation of displacement noise in the DIC measurement; N_L is the number of crack length data; L is the crack length; ω is the weight. An alternative cost function [70, 71] considers the difference between the numerically simulated and DIC measured notch opening displacement (NOD). The new cost function is referred to as FEMU-FCN. It is expressed as

$$\chi_{\text{FEMU-FCN}}(\mathbf{p}) = \frac{\omega}{\sigma_F^2 N_S} \sum_t^{N_S} (F_t^{\text{EXP}} - F_t^{\text{FEA}}(\mathbf{p}))^2 + \frac{(1-\omega)}{\sigma_{\text{NOD}}^2 N_{\text{NOD}}} \sum_t^{N_S} (\text{NOD}_t^{\text{EXP}} - \text{NOD}_t^{\text{FEA}}(\mathbf{p}))^2 \quad (23)$$

Both FEMU-FLN and FEMU-FCN are particularly effective for the identification of CZM parameters. There are two major reasons for that. First, since no field measurement is considered in the cost functions, they can avoid the large strain error near the crack region. Second, additional crack information (crack length, NOD) is included in the cost functions.

One advantage of the global cost functions is that they are less sensitive to local variation abnormality. This advantage is particularly meaningful when the samples have nonnegligible strain or stress concentrations. These global cost functions avoid using the displacement or strain maps from DIC. This is useful when applying the speckle pattern to the specimens is hard to accomplish. However, very

limited information is involved in the global cost functions. This limitation may lead to higher residual for the identified parameters [143]. Additionally, it can hardly be used to identify complicated material models with multiple constitutive parameters.

6.1.2 Local Cost Functions

The local cost functions are constructed from the field response that can be simulated and experimentally measured. They are generally defined based on the 3D shape [366], the strain fields or the displacement fields (measured by 2D-DIC, stereo-DIC, DVC, etc.). The local cost functions can provide much richer information than the global cost functions. The richer information is helpful for identification in complicated models with multiple parameters. It may also contribute to more accurate parameter identification [53]. Richer information increases the likelihood of achieving good sensitivity to all parameters. It must be noted that both the displacement and strain fields have multiple components (e.g., ϵ_{xx} , ϵ_{yy} , ϵ_{xy}). For simplicity, only one component is presented in the cost function in this review, but the combination of multiple components is preferable in most cases.

6.1.2.1 Cost Function Based on Displacement Fields The cost function based on the SSD of the displacement fields [19, 38, 42, 64, 165, 178, 261, 279, 365, 373], denoted as FEMU-U, is written as

$$\chi_{\text{FEMU-U}}(\mathbf{p}) = \sum_t^{N_S} \sum_{i \in \text{ROI}}^{N_D} (u_{t,i}^{\text{EXP}} - u_{t,i}^{\text{FEA}}(\mathbf{p}))^2 \quad (24)$$

where i denotes i -th point in the ROI; N_D is the number of data points in the ROI. Displacements $u_{t,i}^{\text{EXP}}$ and $u_{t,i}^{\text{FEA}}$ are obtained from experimental measurement and FEA, respectively. This cost function considers the influence of each calculation point to be equal.

This cost function can be normalized. The normalized cost functions are denoted as FEMU-UN (Eq. 25). One major aim of the normalization term is to balance the SNR for different samplings. Additionally, it can compensate for the scale differences for each term in the cost function.

$$\chi_{\text{FEMU-UN}}(\mathbf{p}) = \sum_t^{N_S} \sum_{i \in \text{ROI}}^{N_D} \left(\frac{u_{t,i}^{\text{EXP}} - u_{t,i}^{\text{FEA}}(\mathbf{p})}{u_{t,i}^{\text{NORM}}} \right)^2 \quad (25)$$

where $u_{t,i}^{\text{NORM}}$ is the normalization term. It can be different forms, such as $u_{t,i}^{\text{NORM}} = u_{t,i}^{\text{EXP}}$ [58, 60, 65, 374], $u_{t,i}^{\text{NORM}} = \max_i(u_{t,i}^{\text{EXP}}) - \min_i(u_{t,i}^{\text{EXP}})$, $u_{t,i}^{\text{NORM}} = \max_i(u_{t,i}^{\text{EXP}})$, $u_{t,i}^{\text{NORM}} = \text{Std}(u_{t,i}^{\text{EXP}})$, $u_{t,i}^{\text{NORM}} = \max_i(|u_{t,i}^{\text{EXP}}|) - \left| \text{Mean}(u_{t,i}^{\text{EXP}}) \right|$ [41],

209] $u_{t,i}^{\text{NORM}} = \text{RMS}(u_{t,i}^{\text{EXP}})$ (RMS: root mean square operator).

An alternative approach is to normalize the cost function with the covariance matrix. It propagates the measurement uncertainties from the kinematic fields to the sought parameters [157]. Both $\chi_{\text{FEMU-U}}$ and $\chi_{\text{FEMU-UN}}$ are sensitive to the inevitable rigid-body movement of the samples. The rigid-body motion may lead to nonnegligible errors in parameter identification.

6.1.2.2 Cost Function Based on Strain Fields The cost functions using strain fields can effectively avoid the rigid-body motion issue. Similarly as in FEMU-U, the SSD of strain maps can be directly regarded as the cost function [38, 39, 51, 255, 256, 261], which is denoted as FEMU- ϵ .

$$\chi(\mathbf{p}) = \sum_t^{N_S} \sum_{i \in \text{ROI}}^{N_D} \left(\epsilon_{t,i}^{\text{EXP}} - \epsilon_{t,i}^{\text{FEA}}(\mathbf{p}) \right)^2 \tag{26}$$

FEMU- ϵ , like FEMU-U, gives equal weight to all points at all stages. The normalization terms used in FEMU-UN can be seamlessly transferred to FEMU- ϵ , leading to FEMU- ϵN [51].

$$\chi_{\text{FEMU-}\epsilon\text{N}}(\mathbf{p}) = \sum_t^{N_S} \sum_{i \in \text{ROI}}^{N_D} \left(\frac{\epsilon_{t,i}^{\text{EXP}} - \epsilon_{t,i}^{\text{FEA}}(\mathbf{p})}{\epsilon_{t,i}^{\text{NORM}}} \right)^2 \tag{27}$$

One of the most significant limitations in FEMU- ϵ and FEMU- ϵN is the comparatively lower SNR for strain fields. The noise can be improved by a low-pass filter at the cost of more significant systematic error. This operation is more suited to strain fields with relatively low strain gradients. This limitation imposes significant challenges in calibrating the orthotropic elastic properties of some fiber-reinforced composites, such as wood-fiber composites. Material defects may be significant in these materials [59]. The strain fields in these materials may have obvious concentrations, which might make FEMU-U and FEMU-UN preferable to FEMU- ϵ and FEMU- ϵN in such cases. However, systematic errors can hardly be eliminated in real tests.

6.1.2.3 Normalization Strategies Normalization in the cost function may improve the identification stability and robustness. The primary goals are guaranteeing scale invariance, offering outliers robustness and controlling the relative importance of different measurements. Different normalization strategies in FEMU-UN and FEMU- ϵN suit different identification tasks. For the sake of simplicity, we will discuss only FEMU-UN. The discussion can be easily generalized to FEMU- ϵN . The normalization terms $u_{t,i}^{\text{NORM}} = u_{t,i}^{\text{EXP}}$,

$$u_{t,i}^{\text{NORM}} = \max_i(u_{t,i}^{\text{EXP}}) - \min_i(u_{t,i}^{\text{EXP}}) \tag{28}$$

$$u_{t,i}^{\text{NORM}} = \max_i(|u_{t,i}^{\text{EXP}}|) - \left| \text{Mean}_i(u_{t,i}^{\text{EXP}}) \right| \tag{29}$$

and

$u_{t,i}^{\text{NORM}} = \max_i(u_{t,i}^{\text{EXP}})$ (same as for the strain-based FEMU cost function) follow a very similar principle. They are suitable for cases with pronounced systematic errors, such as undermatched material models or imprecisely reproduced boundary conditions. In those cases, the systematic errors tend to increase with loading. These normalization strategies can balance the impact of the displacement or strain errors at different loading stages.

Regarding $u_{t,i}^{\text{NORM}} = u_{t,i}^{\text{EXP}}$, $u_{t,i}^{\text{EXP}}$ could be negligibly small at certain points due to the heterogeneity of the kinematic fields. The small value of $u_{t,i}^{\text{EXP}}$ may produce a singularity in the cost function. One solution is to replace the normalization term with its absolute value and add a small positive compensation. Alternatively, we can eliminate these data points from the cost function entirely due to their low SNR.

Assume that the numerical model matches the real tests perfectly and that only random noise exists in DIC measurement. In this case, a better normalization term $u_{t,i}^{\text{NORM}}$ is $\text{Std}(u_{t,i}^{\text{EXP}})$ at each load step. This strategy is more effective at balancing the cost function at different load steps. Compared with $\text{Std}(u_{t,i}^{\text{EXP}})$, the theoretical uncertainty of each point can be estimated by the covariance matrix. This provides more accurate weighting for each point in the cost function by taking into account the variation in the speckle pattern quality on the sample surface [300]. In some cases (with the same sample, same imaging setup and DIC settings, stable speckle, etc.), it is reasonable to assume a constant DIC measurement uncertainty throughout the experiment, in which case the cost function normalized by $\text{Std}(u_{t,i}^{\text{EXP}})$ is equivalent to the non-normalized one.

6.1.3 Hybrid Cost Function

It must be noted that the cost functions based solely on kinematic fields may result in an underdetermined parameter identification problem. This happens when a displacement boundary condition is applied to FEA. In such cases, the force information must also be included in the cost function.

Combining the aforementioned force-based and displacement- or strain-based cost functions results in hybrid cost functions, also known as weighted FEMU in the literature. In this review, to keep consistency, we denote them as FEMU-UF (non-normalized) [20] or FEMU-UFN (normalized) [40, 43, 143, 187, 250, 264, 375]. Since the displacement and strain fields have different units than force, the direct combination of these cost functions [20] in FEMU-UF does not have any physical meaning. Normalization terms are therefore necessary to balance the influence of different physical quantities.

Force-based cost functions are more robust to stress–strain concentrations, while kinematic-based cost functions facilitate more robust parameter identification of multiple parameters simultaneously. FEMU-UF and FEMU-UFN balance the strengths and weaknesses of both types of cost functions, significantly reducing the parameter identification uncertainty [143]. The FEMU-UFN cost function, which combines the influence of the normalized residual, is given by:

$$\chi_{\text{FEMU-UFN}}(\mathbf{p}) = \omega \chi_{\text{FEMU-FN}}(\mathbf{p}) + (1 - \omega) \chi_{\text{FEMU-UN}}(\mathbf{p}) \quad (28)$$

where $0 < \omega < 1$ is a dimensionless weight controlling the contribution of each part. By setting ω to 1 or 0, this cost function degenerates to $\chi_{\text{FEMU-FN}}$ or $\chi_{\text{FEMU-UN}}$, respectively. A natural and simple choice for ω is 0.5, which give equal weight to the normalized force and displacement residuals [70, 200]. If $\chi_{\text{FEMU-FN}}$ and $\chi_{\text{FEMU-UN}}$ are normalized by the corresponding measurement uncertainty, it is recommended to set the weight ω to $\omega = \frac{N_F}{N_U + N_F}$, based on Bayesian principles [143, 233, 376], where N_F and N_U are the calculation point number for force and displacement, respectively.

Replacing $\chi_{\text{FEMU-UN}}$ with $\chi_{\text{FEMU-eN}}$ leads to $\chi_{\text{FEMU-eFN}}$ [11, 41, 44, 68, 193, 206, 265, 270, 377, 378].

$$\chi_{\text{FEMU-eFN}}(\mathbf{p}) = \omega \chi_{\text{FEMU-FN}}(\mathbf{p}) + (1 - \omega) \chi_{\text{FEMU-eN}}(\mathbf{p}) \quad (29)$$

In comparison with $\chi_{\text{FEMU-UFN}}$, $\chi_{\text{FEMU-eFN}}$ is more robust to rigid-body translation. For clarity, the features of $\chi_{\text{FEMU-eFN}}$ are not discussed in detail here, since they can be easily generalized from $\chi_{\text{FEMU-UFN}}$.

6.1.4 Parameter-Regularization Cost Function

The unknown parameters in most of the cost functions are unconstrained. In the process of optimization, the parameters may converge to unrealistic values. The parameter values can be constrained to a reasonable range by adding a regularization term into the cost function [86]. These constrained terms can also introduce prior knowledge of the constitutive parameters to the cost function. The constrained cost function leads to a “regularized model updating” [379].

By adding regularization terms to FEMU-F, a new cost function, FEMU-FR [61], can be obtained. It is expressed as:

$$\chi_{\text{FEMU-FR}}(\mathbf{p}) = \omega_F \sum_t^{N_S} (F_t^{\text{EXP}} - F_t^{\text{FEA}}(\mathbf{p}))^2 + \sum_k^M \omega_{f_k} f_k(p_k) \quad (30)$$

where ω_F and ω_{f_k} are non-negative weights. $f_k(p_k)$ is a regularization term with respect to the k -th material model parameter p_k . $f_k(p_k)$ should be assumed to have a negligible value within the feasible region but an extremely large value

in the forbidden region for parameter p_k . The regularization terms can also be used with FEMU-U, yielding a constrained cost function FEMU-UR [379, 380].

6.1.5 Multi-physics Cost Functions

The previous cost functions are applicable to most parameter identification tasks. However, in some special identification tasks, such as those involving thermal mechanics, the cost functions need to incorporate additional physical responses beyond just kinematic and force information. Including this extra information can enhance the robustness of FEMU identification.

Rose et al. [105, 230] proposed two cost functions to be used when identifying thermomechanical parameters. The first one is called FEMU-UT. It includes both the displacement field and the temperature field in a weighted cost function [230, 381]. It is written as

$$\chi_{\text{FEMU-UT}}(\mathbf{p}) = \omega_T \sum_t^{N_S} \sum_{i \in \text{ROI}}^{N_T} \left(\Delta T_{t,i}^{\text{EXP}} - \Delta T_{t,i}^{\text{FEA}}(\mathbf{p}) \right)^2 + \omega_U \sum_t^{N_S} \sum_{i \in \text{ROI}}^{N_D} \left(\Delta u_{t,i}^{\text{EXP}} - \Delta u_{t,i}^{\text{FEA}}(\mathbf{p}) \right)^2 \quad (31)$$

where N_T is the number of measured temperature data points at each load step. The relative displacement Δu between neighboring points is used to eliminate the influence of rigid-body motion of the sample. The temperature increment field $\Delta T_{t,i}^{\text{EXP}}$ measured by an IR camera and its counterpart $\Delta T_{t,i}^{\text{FEA}}$ from FEA are also included. ω_T and ω_U are the corresponding weights. This cost function was further extended by adding force information [105]. The new cost function is denoted as FEMU-UFT in this review and is expressed as

$$\chi_{\text{FEMU-UFT}}(\mathbf{p}) = \omega_T \sum_t^{N_S} \sum_{i \in \text{ROI}}^{N_T} \left(\Delta T_{t,i}^{\text{EXP}} - \Delta T_{t,i}^{\text{FEA}}(\mathbf{p}) \right)^2 + \omega_U \sum_t^{N_S} \sum_{i \in \text{ROI}}^{N_D} \left(\Delta u_{t,i}^{\text{EXP}} - \Delta u_{t,i}^{\text{FEA}}(\mathbf{p}) \right)^2 + \omega_F \sum_t^{N_S} \left(F_t^{\text{EXP}} - F_t^{\text{FEA}}(\mathbf{p}) \right)^2 \quad (32)$$

The stress information can also be used to construct the cost function. Jiang et al. [382] measured the residual stress by a so-called contour method [383]. They identified a thermo-mechanical model by using both stress and temperature information using FEMU.

6.2 Sensitivity Analysis

A necessary condition for successful parameter identification in FEMU is that the calculated response must be sensitive to parameter changes. This is ensured by performing a sensitivity analysis [384] to evaluate the identifiability of the problem. By carefully analyzing the sensitivity of the calculated response, the spatial and temporal domains in which the parameters are activated can be determined. Since FEMU optimization involves iteratively updating the parameters to minimize the cost function, the latter should be sensitive to parameter changes. A small perturbation in a parameter should be reflected in an obvious change in the value of the cost function. Sensitivity analysis should be integrated into test design and cost function construction in order to activate the sensitivity of individual parameter. Tests and cost functions with low sensitivity should be refined.

We will review three methods for sensitivity evaluation. The most popular method is based on the sensitivity matrix. The sensitivity is expressed using the Jacobian matrix, formulated as the partial derivatives of the cost function at each point with respect to each parameter. However, this method does not take into account the correlation between different parameters, which can lead to poor convergence of the optimization algorithm and ultimately result in a non-unique solution. A collinearity analysis is highly recommended to better evaluate the identifiability. The third method is variance-based sensitivity analysis, which calculates the so-called Sobol indices in a probabilistic framework instead of using the Jacobian matrix. This method can evaluate both the sensitivity of individual parameters and interaction between two parameters.

6.2.1 Sensitivity Based on Jacobian Matrix

Sensitivity is expressed as the partial derivatives of the model response (e.g., displacement fields, strain fields, crack opening displacement, reaction forces, etc.) with respect to each unknown material model parameter [381]. Generally, a large sensitivity value indicates good identifiability, meaning that a small perturbation leads to a noticeable change in the measurands.

For derivation purposes, we first define the general formulation of FEMU cost function as:

$$\chi(\mathbf{p}) = \sum_{l=1}^{N_S \cdot N_D} (\chi_l(\mathbf{p}))^2 \tag{33}$$

where $\chi_l(\mathbf{p})$ is the individual contribution of the differences between the measured and the calculated response to the cost function. The index l represents each individual contribution. The sensitivity is expressed by the Jacobian matrix \mathbf{J} ,

defined as a partial derivative of individual cost function contribution $\chi_l(\mathbf{p})$ over each parameter:

$$\mathbf{J} = \begin{bmatrix} \frac{\partial \chi_1}{\partial p_1} & \frac{\partial \chi_1}{\partial p_2} & \dots & \frac{\partial \chi_1}{\partial p_M} \\ \frac{\partial \chi_2}{\partial p_1} & \frac{\partial \chi_2}{\partial p_2} & \dots & \frac{\partial \chi_2}{\partial p_M} \\ \vdots & \vdots & \ddots & \vdots \\ \frac{\partial \chi_{N_S \cdot N_D}}{\partial p_1} & \frac{\partial \chi_{N_S \cdot N_D}}{\partial p_2} & \dots & \frac{\partial \chi_{N_S \cdot N_D}}{\partial p_M} \end{bmatrix} \tag{34}$$

where M is the number of unknown parameters. In the case of FEMU- ϵ , where the cost function is given by Eq. (26), the sensitivity [107] is given by the modified Jacobian matrix of size $(N_S \cdot N_D \times M)$:

$$\mathbf{J} = \begin{bmatrix} \frac{\partial \epsilon_{1,1}^{FEA}}{\partial p_1} & \frac{\partial \epsilon_{1,1}^{FEA}}{\partial p_2} & \dots & \frac{\partial \epsilon_{1,1}^{FEA}}{\partial p_M} \\ \frac{\partial \epsilon_{1,2}^{FEA}}{\partial p_1} & \frac{\partial \epsilon_{1,2}^{FEA}}{\partial p_2} & \dots & \frac{\partial \epsilon_{1,2}^{FEA}}{\partial p_M} \\ \vdots & \vdots & \ddots & \vdots \\ \frac{\partial \epsilon_{1,N_D}^{FEA}}{\partial p_1} & \frac{\partial \epsilon_{1,N_D}^{FEA}}{\partial p_2} & \dots & \frac{\partial \epsilon_{1,N_D}^{FEA}}{\partial p_M} \\ \frac{\partial \epsilon_{2,1}^{FEA}}{\partial p_1} & \frac{\partial \epsilon_{2,1}^{FEA}}{\partial p_2} & \dots & \frac{\partial \epsilon_{2,1}^{FEA}}{\partial p_M} \\ \frac{\partial \epsilon_{2,2}^{FEA}}{\partial p_1} & \frac{\partial \epsilon_{2,2}^{FEA}}{\partial p_2} & \dots & \frac{\partial \epsilon_{2,2}^{FEA}}{\partial p_M} \\ \vdots & \vdots & \ddots & \vdots \\ \frac{\partial \epsilon_{N_S \cdot N_D}^{FEA}}{\partial p_1} & \frac{\partial \epsilon_{N_S \cdot N_D}^{FEA}}{\partial p_2} & \dots & \frac{\partial \epsilon_{N_S \cdot N_D}^{FEA}}{\partial p_M} \end{bmatrix} \tag{35}$$

This formulation is directly related to the structure of the cost function, including the different units of the physical responses (e.g. forces, displacements and strains). Note that only one strain component is included here, while in general it is preferable to consider all the three strain components. To do that, we can augment more rows corresponding to the sensitivity of the other strain components to the current Jacobian matrix. As the Jacobian matrix indicates, the sensitivities of these quantities to parameter changes can hardly be directly compared. One solution is to resort to parameter scaling and cost function normalization strategies to obtain dimension-free sensitivity. The columns of the matrix are multiplied by the normalization term $\xi_{i,k} = \frac{p_k}{\sqrt{\frac{1}{N_D} \sum_i (\epsilon_{i,i}^{FEA})^2}}$. The Jacobian matrix \mathbf{J} can be normalized into:

$$\bar{\mathbf{J}} = \begin{bmatrix} \xi_{1,1} \frac{\partial \varepsilon_{1,1}^{\text{FEA}}}{\partial p_1} & \xi_{1,2} \frac{\partial \varepsilon_{1,1}^{\text{FEA}}}{\partial p_2} & \cdots & \xi_{1,M} \frac{\partial \varepsilon_{1,1}^{\text{FEA}}}{\partial p_M} \\ \xi_{1,1} \frac{\partial \varepsilon_{1,2}^{\text{FEA}}}{\partial p_1} & \xi_{1,2} \frac{\partial \varepsilon_{1,2}^{\text{FEA}}}{\partial p_2} & \cdots & \xi_{1,M} \frac{\partial \varepsilon_{1,2}^{\text{FEA}}}{\partial p_M} \\ \vdots & \vdots & \ddots & \vdots \\ \xi_{1,1} \frac{\partial \varepsilon_{1,N_D}^{\text{FEA}}}{\partial p_1} & \xi_{1,2} \frac{\partial \varepsilon_{1,N_D}^{\text{FEA}}}{\partial p_2} & \cdots & \xi_{1,M} \frac{\partial \varepsilon_{1,N_D}^{\text{FEA}}}{\partial p_M} \\ \xi_{2,1} \frac{\partial \varepsilon_{2,1}^{\text{FEA}}}{\partial p_1} & \xi_{2,2} \frac{\partial \varepsilon_{2,1}^{\text{FEA}}}{\partial p_2} & \cdots & \xi_{2,M} \frac{\partial \varepsilon_{2,1}^{\text{FEA}}}{\partial p_M} \\ \xi_{2,1} \frac{\partial \varepsilon_{2,2}^{\text{FEA}}}{\partial p_1} & \xi_{2,2} \frac{\partial \varepsilon_{2,2}^{\text{FEA}}}{\partial p_2} & \cdots & \xi_{2,M} \frac{\partial \varepsilon_{2,2}^{\text{FEA}}}{\partial p_M} \\ \vdots & \vdots & \ddots & \vdots \\ \xi_{N_S,1} \frac{\partial \varepsilon_{N_S,N_D}^{\text{FEA}}}{\partial p_1} & \xi_{N_S,2} \frac{\partial \varepsilon_{N_S,N_D}^{\text{FEA}}}{\partial p_2} & \cdots & \xi_{N_S,M} \frac{\partial \varepsilon_{N_S,N_D}^{\text{FEA}}}{\partial p_M} \end{bmatrix} \quad (36)$$

The normalized Jacobian is related to a normalized cost function with the same normalization terms $\sqrt{\frac{1}{N_D} \sum_i \left(\varepsilon_{t,i}^{\text{FEA}} \right)^2}$. Sensitivity calculation requires the partial derivative of the strain components with respect to each parameter. A straightforward and practical approach is to use the finite difference approximation method with a small perturbation (e.g., 1% [50, 224], 0.5% [38, 107]) on each parameter. We should emphasize that a good value of relative parameter perturbation is governed by the tradeoff between the roundoff and the truncation error, which is driven by the machine precision: $\Delta p_k^{(j)} = p_k^{(j)} \sqrt{\delta}$, where δ is the machine precision ($\delta = 10^{-8}$ for single precision) [385]. For a given parameter $p_k^{(j)}$ perturbation at j -th iteration, the components of the modified Jacobian matrix are numerically calculated as

$$\frac{\partial \varepsilon_{t,i}^{\text{FEA}}(\mathbf{p}^{(j)})}{\partial p_k^{(j)}} = \frac{\varepsilon_{t,i}^{\text{FEA}}(\mathbf{p}^{(j)} + \Delta \mathbf{p}_k^{(j)}) - \varepsilon_{t,i}^{\text{FEA}}(\mathbf{p}^{(j)})}{\Delta p_k^{(j)}} \quad (37)$$

where $\Delta \mathbf{p}_k^{(j)}$ is the parameter perturbation vector written as

$$\Delta \mathbf{p}_k^{(j)} = [0, 0, \dots, 0, \Delta p_k^{(j)}, 0, \dots, 0]^T \quad (38)$$

Attention should be paid to the fact that in Eq. (37), the partial derivative of $\varepsilon_{t,i}^{\text{FEA}}(\mathbf{p}^{(j)})$ with respect to the k -th parameter $p_k^{(j)}$ requires two evaluations of the FEA model. The calculation of $\bar{\mathbf{J}}$ therefore requires at least $M + 1$ evaluations of the FEA model. This operation can be very time-consuming, especially when many parameters need to be identified in the material model.

Based on the sensitivity analysis, we can visualize the results in multiple ways. A straightforward method is to plot the heterogeneous sensitivity map at each load step, as shown in Fig. 19a. However, due to the complex sensitivity distribution, directly comparing the sensitivity maps is difficult. There is a special case involving global cost functions (e.g., FEMU-F), where the Jacobian matrix has a size of $1 \times M$ at each load step, in which case a scalar instead of a vector is obtained for the sensitivity to a single parameter.

The evolution curve of the sensitivity with respect to each parameter can be directly obtained during the loading process [56, 224]. This sensitivity evolution can also be used to determine the preferable load state for identification. To better evaluate the heterogeneous sensitivity with respect to each parameter, an indicator ζ_k defined as the Euclidean norm of the k -th column in the Jacobian [107] can be used.

$$\zeta_k = \sqrt{\frac{1}{N_S N_D} \sum_{l=1}^{N_S N_D} J_{l,k}^2} \quad (39)$$

The indicator ζ_k for k -th parameter can combine the influences from different load steps into a single scalar. It enables direct comparison of the sensitivity with respect to each parameter. The parameter whose sensitivity falls below a given threshold [237] can be considered as having poor identifiability. However, no standard exists to set this threshold in FEMU yet. The order of magnitude, that is the relative values of the sensitivity compared to each other, is a better indicator than the absolute sensitivity value of each material parameter [386, 387].

6.2.2 Conditioning and Collinearity Evaluation

Good sensitivity for every parameter is a necessary but not sufficient condition for good identifiability. It can directly influence the convergence of the optimization problem. One parameter with large sensitivity may be deeply coupled with some other parameters. As a result of such correlation issues, a parameter with large sensitivity may still be difficult to identify. To evaluate such cross-influences between different parameters, we can use the Hessian matrix defined by the second derivatives of the cost function:

$$\mathbf{H} = \begin{bmatrix} \frac{\partial^2 \chi}{\partial p_1^2} & \frac{\partial^2 \chi}{\partial p_1 \partial p_2} & \cdots & \frac{\partial^2 \chi}{\partial p_1 \partial p_M} \\ \frac{\partial^2 \chi}{\partial p_2 \partial p_1} & \frac{\partial^2 \chi}{\partial p_2^2} & \cdots & \frac{\partial^2 \chi}{\partial p_2 \partial p_M} \\ \vdots & \vdots & \ddots & \vdots \\ \frac{\partial^2 \chi}{\partial p_M \partial p_1} & \frac{\partial^2 \chi}{\partial p_M \partial p_2} & \cdots & \frac{\partial^2 \chi}{\partial p_M \partial p_M} \end{bmatrix} \quad (40)$$

From an implementation perspective, the formulation above is intricate and computationally time consuming. The second reason why such a formulation is rarely utilized in optimization algorithms is that the quadratic approximation of the cost function performs poorly near the extreme values of the cost function, which can lead to divergence. It is therefore more practical to use a linear approximation of the Hessian matrix, defined as:

$$\mathbf{H} \approx \mathbf{J}^T \mathbf{J} \quad (41)$$

In the Hessian matrix, the diagonal terms denote the sensitivity to each parameter, while the off-diagonal terms show the cross-influence between two parameters. The rate

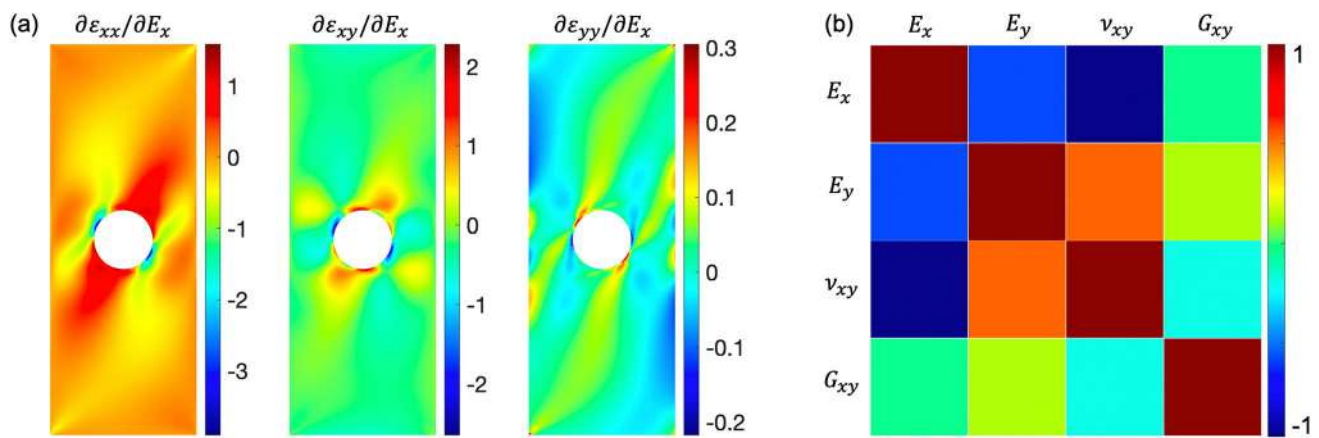


Fig. 19 **a** Normalized sensitivity map of ϵ_{xx} , ϵ_{xy} and ϵ_{yy} with respect to E_x for an orthotropic elastic material, **b** the correlation matrix for collinearity evaluation. The material model parameters E_x , E_y , G_{xy} , ν_{xy} are set to 10 GPa, 5 GPa, 0.3 and 3 GPa, respectively. The sample

size is 15 × 40 mm with an open-hole diameter of 6 mm. The off-axis loading orientation is at an angle of $\frac{\pi}{6}$ with respect to the fiber direction

of convergence of gradient-based methods depends on the condition number κ of the Hessian of the cost function at the optimum point. If the condition number is large, the method is slow to converge and identifiability is hindered due to the possibility of coupling between parameters. The condition number [388] is defined as the ratio between the largest and the smallest eigenvalue of the Hessian matrix:

$$\kappa = \frac{\lambda_{\max}}{\lambda_{\min}} \tag{42}$$

where λ_{\min} and λ_{\max} are the smallest and largest eigenvalue of Hessian matrix, respectively. If the problem is ill-conditioned, $\log_{10}\kappa$ digits should be expected in computing the solution [389]. A similar approach that involves calculating the decimal logarithm of the Hessian matrix was implemented by Vargas et al. [56, 224] to analyze the conditioning of the optimization problem. They considered a condition number below 10 for a good identifiability. The identifiability of the optimization problem can be improved by Hessian matrix regularization and scaling of the parameter design space [388]. This approach ensures that the conditioning of the problem is determined by the smallest eigenvalue of the Hessian matrix.

This is particularly important when there coupling exists between parameters. If there is coupling between two or more parameters, the condition number becomes large as λ_{\min} approaches 0. To evaluate the coupling of multiple parameters in identification, Zhang et al. [107] adopted the collinearity index proposed by Brun et al. [390]. The collinearity index is defined as

$$\gamma_Q = \frac{1}{\sqrt{\lambda_{\min}}} \tag{43}$$

where λ_{\min} is the smallest eigenvalue of $\tilde{\mathbf{J}}_q^T \tilde{\mathbf{J}}_q$ (size of $q \times q$). Q is a parameter subset with a size of q . For a small subset of the parameter vector, the corresponding columns in the full sensitivity matrix are selected from \mathbf{J} [Eq. (36)] and normalized by the l^2 -norm of each corresponding column, leading to the subset sensitivity matrix denoted as $\tilde{\mathbf{J}}_q$ [107]. An example of the correlation matrix in full parameter space is shown in Fig. 19b. The value in the correlation matrix ranges in $[-1, 1]$. The sensitivity matrix is symmetric with the main diagonal being one. Larger absolute value in this matrix denotes highly correlated parameter pair.

There are, in total, $2^M - M - 1$ possible combinations of the parameters, leading to $2^M - M - 1$ collinearity indexes. The response of one parameter is easier to compensate by a greater number of other parameters. For this reason, parameter collinearity is more significant when more parameters are considered in $\tilde{\mathbf{J}}_q$. In the case of normalized sensitivities, collinearity indexes γ_Q below 20 [107] can be regarded as indicating good identifiability. Such analysis can help to find the largest identifiable set of parameters for which the collinearity of the parameter subset is below a chosen collinearity threshold.

6.2.3 Variance-Based Sensitivity Analysis

The variance-based sensitivity analysis, also known as Sobol indices [391], is a global sensitivity analysis method that has also been used to analyze the sensitivity of FEMU [220, 392–394]. The Sobol indices are calculated within a probabilistic framework instead of relying on a Jacobian matrix. The variance of the cost function might be mainly affected by some parameters, which can be interpreted as the measure of sensitivity.

There are two typical types of Sobol indices, the first-order Sobol index, and the total Sobol index. The first-order indices are used to evaluate the sensitivity of an output (such as the cost function χ) with respect to each parameter. The total Sobol indices can quantify the interactions between these parameters.

The first-order sensitivity is written as

$$S_k = \frac{V_{p_k}(E_{\mathbf{p}_{\sim k}}(\chi|p_k))}{V(\chi)} \quad (44)$$

where $V_{p_k}(E_{\mathbf{p}_{\sim k}}(\chi|p_k))$ is the conditional variance of the expected value of the output χ when all parameters are fixed, except for p_k . $V(\chi)$ is the unconditional variance of the output. $V_{p_k}(E_{\mathbf{p}_{\sim k}}(\chi|p_k))$ varies between 0 and $V(\chi)$. The first-order sensitivity S_k , therefore, varies between 0 and 1. The total Sobol index is calculated as

$$S_{Tk} = 1 - \frac{V_{\mathbf{p}_{\sim k}}(E_{p_k}(\chi|\mathbf{p}_{\sim k}))}{V(\chi)} \quad (45)$$

where $V_{\mathbf{p}_{\sim k}}(E_{p_k}(\chi|\mathbf{p}_{\sim k}))$ denotes the conditional variance of the expected value of the output χ when only parameter p_k is fixed. The calculation of the sensitivity can be obtained through Monte Carlo integrals and quasi-random sampling. For more detail about the calculation of Sobol indices using Monte Carlo method see Ref. [394].

Pereira et al. [392] calculated Sobol indices to compare parameter identifiability. They investigated the influence of the Swift hardening law and the Hill48 anisotropic yield criterion on the forces, principal strains, strain path and thickness reduction. Alfano et al. [220] evaluated the first-order sensitivity of the cost function in FEMU with respect to each material model parameter in various CZMs, including bilinear, trapezoidal and potential based CZMs. Li and Lubineau [393] aimed to find the most informative and measurable metrics by global sensitivity analysis. The sensitivity analysis shows that properly selecting measurable metrics in space and time has a considerable influence on the sensitivity. They constructed the cost function based on the sensitivity analysis for better parameter identification in FEMU.

6.3 Data Fusion

In classical FEMU, experimental measurement and numerical simulation are implemented separately. To facilitate comparison between the FEA and DIC data, the data points from FEA and DIC need to be aligned. This is particularly important for strain fields with large gradients. Data point fusion includes two primary aspects: the alignment of the two coordinate systems and the interpolation of the data points.

The data fusion pipeline is schematically illustrated in Fig. 20. It involves fusing the data points from experiments

and simulations into the same mesh in the same coordinate system. This is accomplished by a sequence of steps, beginning with a rigid-body transformation, followed by scaling and finally data point interpolation. Transformation is used to align the coordinate systems. It can be implemented by imposing a rigid-body transformation (2D transformation for 2D-DIC and 3D transformation for stereo-DIC [38, 264]) onto the measured point cloud. Once the coordinate systems are matched, the data points from the real experiment (simulation) should be interpolated to the simulation (real experiment).

6.3.1 Coordinate System Alignment

A small misalignment of the coordinate system can have a surprisingly large effect [37] on the identification process. Beyond a certain level of misalignment, finding reliable parameters becomes impossible [395]. Ruybalid et al. [130] assessed the performance of FEMU and I-DIC when subjected to different error sources. They found that misalignment of the specimen can further increase errors in the identified material parameters. Despite the importance of aligning the DIC and FEM data, there is limited information on how researchers perform the alignment of the full-field measurements with FEM data. Here, we review two types of methods for coordinate system alignment. The first category is based on feature point detection and matching, while the second relies on specimen edge detection and matching.

The first type of method is straightforward and efficient. Bruno et al. [396] utilized a linear transformation matrix to map the location of three calculation points to their pixel positions on the image. A similar approach involves detecting some reference points on image. The coordinates of these points on the sample are known in advance, enabling the transformation of the model coordinate system. Both coordinate alignment methods rely on having some easy-to-detect feature points on the sample to serve as reference points. However, they become increasingly difficult to use and error-prone when the sample [190] has smooth shapes and lacks easy-to-detect feature points.

The second type of method involves specimen shape detection and alignment (point set registration). One of the best-known methods for point set registration is the iterative closest point (ICP) algorithm introduced by Besl and McKay [397]. The algorithm iteratively aligns two data sets by searching the closest points and minimizing the matching error. It is, however, impossible to guarantee the convergence robustness of this method in cases of initial misalignment [398]. The robustness of the registration process for FEMU was improved by Maček et al. [123], whose methodology involves first recognizing the contour. By matching the contour with the CAD model, the transformation between the two coordinate systems can be calibrated.

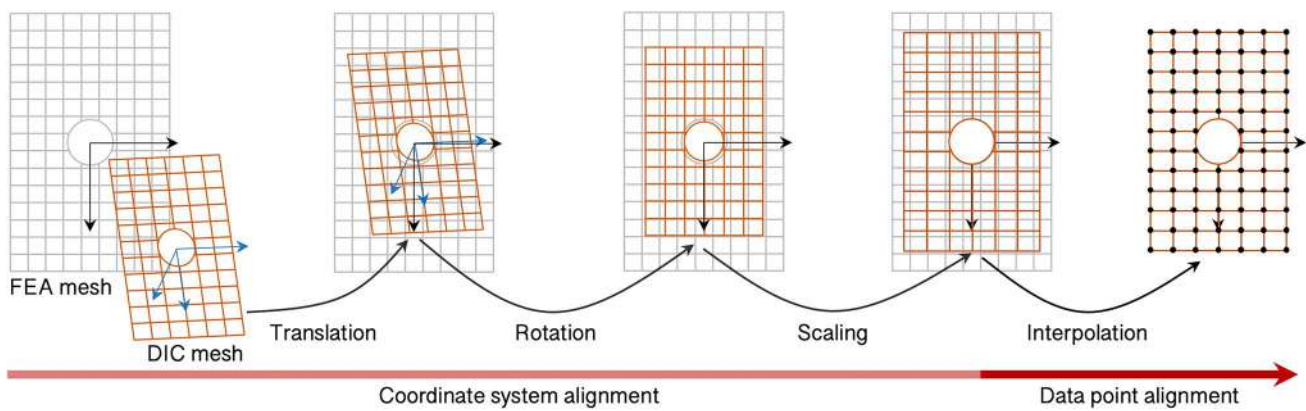


Fig. 20 Data fusion between the kinematic data from FEA and DIC

6.3.2 Data Point Alignment

Another problem to be solved in data fusion is that the data points in simulation and experiment do not coincide when transformed into the same coordinate system. To calculate the cost function, it is necessary to align the data points from experiments and simulations to the same locations. For simplicity, we focus only on the classical FEMU method. Additionally, we assume the cost function is constructed from the kinematic fields. Three typical data fusion methods are reviewed here. The one most widely used is the classical interpolation method. The mesh sharing strategy and the field decomposition method also each have unique advantages. The data fusion method discussed can be generalized to some other physical fields. It should be noted that dedicated algorithms are required when merging data from measuring systems that rely on the Lagrangian (DIC) and Eulerian (temperature fields from IR camera) viewpoint.

The classical interpolation methods, such as bilinear interpolation [38, 105, 337], natural neighbor interpolation [51] and cubic-spline interpolation method [11] can be directly used for this task. Interpolating the data points from a finer mesh to a coarser mesh [105] can reduce interpolation error. Conversely, interpolating from a coarser mesh to a finer mesh yields more data points in the cost function. Finally, the cost function can be easily calculated based on the aligned data points.

The mesh sharing strategy can eliminate the extra data point interpolation step [47, 60]. It involves first generating a mesh that will serve to provide the calculation points for both DIC (or FEA). The mesh is then exported to the FEA solver (or DIC software). Since DIC and FEA share the same nodes, no extra interpolation is required, which is beneficial for more accurate identification.

Finally, there is the so-called field decomposition method [48, 358, 399, 400]. This method can significantly reduce the data dimension. It projects the high-dimensional

displacement or strain field onto a set of orthogonal basis functions (such as Chebyshev polynomials [400] or modified Zernike polynomials [48, 399]). The measured physical fields are approximated by a small set of basis functions. A shape feature vector can then be obtained for each physical field. This method can significantly reduce redundant information in the physical fields. The gap between DIC and FEA is then evaluated as the distance between the two shape feature vectors. A benefit of this method is that there is no need to compute the data in DIC and FEA at the same nodes. The identification of the elastoplastic material properties demonstrated that the method is more accurate than the direct method that uses all the information from DIC measurement [48].

6.4 Optimization Algorithm

In principle, FEMU solves a non-linear least squares optimization problem. This optimization problem is in most cases highly non-convex, with potentially multiple local optima. A non-linear optimization algorithm [401] should be developed to inversely identify the unknown model parameters by iteratively minimizing the cost function.

For simplicity, consider a parameter identification task based on the FEMU- ϵ cost function [Eq. (26)]. An optimization algorithm should be used to iteratively find the parameter vector \mathbf{p} (with M dimensions). The algorithm iterates the parameters until the cost function value falls below a threshold or until the parameters stagnate [18].

A favorable algorithm should offer a good balance between the convergence radius and convergence speed. In the context of FEMU, optimization algorithms fall mainly into four categories: gradient-based methods, derivative-free methods, hybrids of gradient-based and derivative-free methods, and the trust region algorithm. The gradient-based methods converge quickly but at the cost of a limited convergence radius, which means they often converge to a local

Table 10 Summary of typical optimization algorithms

Optimization methods	Specific algorithms	Comments
Gradient-based methods	Gradient descent method [86, 122] Gauss–Newton algorithm [38, 71, 119, 130, 178, 207, 403] Levenberg–Marquart algorithm [11, 51, 65, 122, 270, 378] SQP algorithm [60, 64, 362] BFGS algorithm [86, 307]	High efficiency if a good initial guess is given. Otherwise, convergence is hard to obtain
Derivative-free algorithms	Nelder–Mead method [59, 61, 68, 226] Genetic algorithm [196, 262, 337, 351] Powell algorithm [362] Bisection method [365] Simulated annealing [409, 410] Particle swarm optimization [411]	Relatively low efficiency but better convergence capability
Hybrid methods	Evolutionary algorithm + Levenberg–Marquardt algorithm [174, 412] Particle swarm optimization + gradient-based algorithm [129]	A balance between convergence efficiency and convergence capability
Trust region algorithm	First-order and quadratic trust region algorithm [250, 373, 415]	A balance between convergence efficiency and convergence capability

optimum instead of the global optimum. The derivative-free methods generally have a larger convergence radius, but may require more iterations. A practical approach that balances identification efficiency and accuracy is to use a derivative-free method for the initial guess, followed by a gradient-based method for final iterative optimization. A comparison of the some typical FEMU optimization algorithms is offered in structural health monitoring community [402]. The typical optimization algorithms are summarized in Table 10.

6.4.1 Gradient-Based Algorithms

Gradient-based optimization algorithms are those that require gradient information of the cost function. The gradient of the cost function with respect to the constitutive parameters indicates the direction of the steepest increase or decrease of the cost function.

The first step in these algorithms is to designate a good initial guess. Then, the gradient of the cost function is either analytically or numerically calculated. Gradient calculation is one of the most time-consuming steps in the optimization process. Thereafter, the constitutive parameters can be iteratively optimized. Gradient-based algorithms are efficient when the cost function is convex; otherwise, convergence can be difficult to achieve.

Here, we review some of the most widely accepted gradient-based optimization algorithms, focusing in particular on the gradient descent method, the Gauss–Newton algorithm and the Levenberg–Marquart (LM) algorithm. Additionally, we briefly introduce some other algorithms,

such as Sequential Quadratic Programming and the Broyden–Fletcher–Goldfarb–Shanno (BFGS) algorithm.

6.4.1.1 Gradient Descent Method In the gradient descent method [86, 122], the local minimum is iteratively approached by moving towards the opposite direction along the gradient direction. It has a first-order convergence rate. The algorithm updates the parameter vector $\mathbf{p}^{(j+1)}$ at j -th iteration as

$$\mathbf{p}^{(j+1)} = \mathbf{p}^{(j)} - \gamma \nabla \chi(\mathbf{p}^{(j)}) = \mathbf{p}^{(j)} + \gamma \mathbf{J}^T \left\{ \varepsilon_{t,i}^{\text{EXP}} - \varepsilon_{t,i}^{\text{FEA}}(\mathbf{p}^{(j)}) \right\} \quad (46)$$

where \mathbf{J} is defined by Eq. (34); $\gamma > 0$ is a small step size that has significant impact on the algorithm performance.

6.4.1.2 Gauss–Newton Algorithm The Newton-type algorithms are iterative optimization algorithms with second-order convergence (assuming a good initial guess is provided). This algorithm requires calculating the second-order derivative matrix (Hessian matrix or its approximation) of the cost function with respect to the parameters. As a result, it is less robust than the gradient descent algorithm for non-convex optimization problems. They have been widely used in FEMU [38, 71, 119, 130, 207, 384, 403] when a good initial guess is available. The iteration of the algorithm can be express as

$$\mathbf{p}^{(j+1)} = \mathbf{p}^{(j)} + (\mathbf{J}^T \mathbf{J})^{-1} \mathbf{J}^T \left\{ \varepsilon_{t,i}^{\text{EXP}} - \varepsilon_{t,i}^{\text{FEA}}(\mathbf{p}^{(j)}) \right\} \quad (47)$$

The Newton-type algorithms normally also need to numerically calculate \mathbf{J} at each iteration, similar to

the gradient descent method. It must be noted that the Gauss–Newton (GN) algorithm is rather sensitive to the initial guess of the parameters and may easily converge to a local minimum instead of the global minimum if the initial guess is not good enough.

6.4.1.3 Levenberg–Marquardt Algorithm The Levenberg–Marquardt (LM) algorithm is a tradeoff between the GN algorithm and the gradient descent algorithm. In comparison with the GN algorithm, it can increase the convergence radius without sacrificing too much convergence speed. Thanks to this advantage, it is popular in FEMU [11, 51, 65, 122, 270, 373, 378]. The algorithm is expressed as

$$\mathbf{p}^{(j+1)} = \mathbf{p}^{(j)} + (\mathbf{J}^T \mathbf{J} + \lambda \mathbf{I})^{-1} \mathbf{J}^T \left\{ \varepsilon_{t,i}^{\text{EXP}} - \varepsilon_{t,i}^{\text{FEA}}(\mathbf{p}^{(j)}) \right\} \quad (48)$$

where λ is called the damping factor and \mathbf{I} is the identity matrix. This algorithm degenerates to a GN algorithm when $\lambda = 0$.

6.4.1.4 Other Gradient-Based Algorithms The previously discussed algorithms are primarily suitable for unconstrained nonlinear optimization problems. Sequential Quadratic Programming (SQP) [60, 64, 362] is a powerful optimization algorithm for solving nonlinearly constrained optimization problems. What makes this algorithm attractive in FEMU is that the unknown parameters are generally bounded.

The Broyden–Fletcher–Goldfarb–Shanno (BFGS) algorithm is one of the most popular Quasi-Newton methods. Its most appealing feature is that it updates the inverse of the Hessian matrix instead of calculating the matrix at every iteration. The BFGS algorithm and its variations (e.g., the Limited-memory BFGS [404]) have also been employed in FEMU optimization [86, 307].

In gradient-based algorithms, one of most computationally expensive tasks is the calculation of the Jacobian matrices (or sensitivity matrices) at each iteration. Neggers et al. [133] proposed using a secant method to reduce this computational burden. They proposed only updating the sensitivity matrices when the cumulative change in the parameters since the last sensitivity update exceeds 5%. This does not necessarily speed up the overall calculation, however. This is because less accurate sensitivity matrices calculation may demand more iterations despite each iteration being faster.

6.4.2 Derivative-Free Optimization Algorithms

The derivative-free optimization algorithms aim to efficiently find good solutions in non-convex optimization tasks. These algorithms rely solely on the cost function value, avoiding the cumbersome process of gradient calculation for the cost function. Generally, derivative-free algorithms

are more robust with respect to escaping local optima compared to gradient-based algorithms. However, they tend to converge more slowly when a good initial guess is provided, or when the problem is convex. These algorithms are more suitable for high-dimension optimization problem.

When testing a new material, very limited prior information is available related to the material model parameters. This makes it challenging to start the optimization algorithm from a good initial guess, necessitating the use of derivative-free optimization methods in FEMU. Several typical derivative-free optimization algorithms are introduced here, along with their applications in FEMU. The one in most common use is the Nelder–Mead method. Other good alternatives for use in FEMU include the Genetic Algorithm, the Powell’s algorithm, simulated annealing, particle swarm optimization, etc.

6.4.2.1 Nelder–Mead Method The Nelder–Mead method (NM method, or Nelder–Mead-simplex method) [405, 406], is a heuristic, simple, multidimensional and derivative-free optimization algorithm immensely popular in FEMU [59, 61, 68, 226]. The algorithm begins with $M + 1$ points, which are considered as the vertices of a simplex. The simplex is then sequentially reflected, contracted, and expanded to minimize the function value at its vertices.

The algorithm is fairly efficient, as it typically evaluates the function value only once or twice per iteration. Moreover, due to its derivative-free nature, it is simple to integrate extra constraints into optimization tasks. However, it is still less efficient than the gradient-based methods when a good initial guess is provided and may sometimes get stuck in sub-optimal solutions. The NM optimization algorithm has been used to identify the orthotropic elastic properties of wood [68, 69], the mode-I CZM parameters from a SENB test [58, 61, 226, 380], the viscoelastic parameters of a polymer [158], the anisotropy yield criteria of aluminum alloy [187], the modulus distribution in a bamboo specimen [256], etc.

6.4.2.2 Genetic Algorithm The Genetic Algorithm (GA) [407] is a meta-heuristic, evolutionary algorithm inspired by natural selection in biology. It begins with a randomly generated population of several individuals, or chromosomes. In the context of FEMU, each individual represents an unknown parameter vector. The gene in the algorithm is an identified parameter. The fitness (defined as the cost function value in the FEMU optimization problem) of each individual in the population is then calculated. Individuals with higher fitness scores are more likely to be selected for reproduction, mimicking the survival of the fittest in nature. Offspring for the next generation are produced from the selected individuals through genetic crossover and mutation. The offspring generation produced will replace the individuals with lower fitness in the parent generation. The

algorithm continues to iterate through this process until a given stop criterion is met, at which point the process terminates.

GA is also a derivative-free algorithm. It has decent efficiency and can be easily parallelized [262, 408]. Moreover, it is suitable for high-dimensional optimization. However, the FEA model needs to be evaluated multiple times in each generation, which can be quite time-consuming. The algorithm is likewise not a good option for simple problems, where the classical gradient-based algorithms are preferable. GA typically has a larger convergence radius than gradient-based algorithms.

GA has also been extensively used in FEMU [49, 196, 262, 337, 351]. Sun et al. [262] identified the mechanical parameters in different zones in a welded line via micro-indentation tests and GA optimization. Aguir et al. [196] calibrated the elastoplastic behavior of a stainless steel using GA. To reduce the FEA workload in GA optimization, the authors trained an artificial neural network to predict responses instead of relying on FEA. Liu et al. [351] identified four damage parameters in the Bonora damage model, which is sensitive to temperature and strain rate, using GA. The algorithm identified the parameters by minimizing the gap between experimental and numerically simulated force–displacement curves.

6.4.2.3 Other Derivative-Free Algorithms Several other derivative-free algorithms have also been considered in FEMU. The Powell algorithm was adopted in Ref. [362]. The authors compared the performance of several gradient-based and derivative-free algorithms, concluding that the Powell algorithm performs best for identifying plasticity parameters.

The bisection method is a simple and robust derivative-free algorithm. It works by repeatedly bisecting the region between two points and then selecting the subregion where the function changes sign. Touzeau et al. [365] used this method to calibrate the hyperelastic parameters in a dynamic framework. This algorithm, however, has poor efficiency, and is generally used as an initialization strategy for other, more efficient algorithms.

Simulated annealing is a meta-heuristic and a probabilistic algorithm inspired by the annealing process in material science. This algorithm has a high probability of finding the global optimum, which makes it attractive [409, 410]. Particle swarm optimization (PSO) [411] is another meta-heuristic algorithm; this one is inspired by social behavior. While attractive for detecting global optima, this algorithm is computationally expensive and sensitive to noise, so it is rarely employed on its own in FEMU. Instead, it is typically used to generate initial guesses [129, 374].

In addition to the above, the hill climbing algorithm, a meta-heuristic iterative local search algorithm, and the

random search algorithm, a simple heuristic optimization method, are also feasible for FEMU optimization [210].

6.4.3 Hybrids of the Gradient-Based and Derivative-Free Methods

The derivative-free algorithms are more robust in terms of detecting a good solution but lack efficiency. The gradient-based algorithms are, by contrast, much more efficient when the initial guess is reasonably close to the global optimum. A preferable approach to optimization is to combine both in order to exploit their individual advantages. A derivative-free algorithm can be used to get the initial guess, then the gradient-based methods are applied for more efficient parameter calibration. For instance, combining the genetic/evolutionary algorithm and the LM algorithm [174, 412], or hybridizing PSO with a gradient-based optimization algorithm [129], is a highly recommended approach that has proven effective in FEMU.

6.4.4 Trust Region Algorithm

The trust region algorithm begins by setting an initial estimation of the solution. A trust region is then defined in the vicinity of this initial solution. Within this region, we can safely assume (or “trust”, hence the name), that a constructed model (typically using a first-order [413] or a quadratic [414] model) can adequately approximate the cost function. By minimizing the constructed model within the trust region, we can arrive at a local solution. If this local solution performs better than the original one, the trust region is expanded, and the solution updated. If not, the trust region size is reduced.

The concept of the trust region algorithm is simple and effective. Such algorithms have seen widespread use in FEMU to optimize material model parameters, such as the orthotropic elastoplastic material model parameters for paper foils through biaxial tensile tests [250], the parameters in the Lubliner type material model for concrete [373], and the parameters in the von Mises yield criterion and power isotropic hardening law for thin-walled aluminum tubes [415].

6.5 Optimization Strategies

Currently, most algorithms optimize all parameters simultaneously in an iterative manner. The resulting high-dimensional parameter hyperspace may lead to instability and low efficiency in parameter updating. Such optimization is especially challenging when identifying advanced material models with a large set of unknown parameters.

An attractive and simple solution is to adopt a multi-step optimization strategy, i.e., identifying different sets of parameters sequentially [47] instead of simultaneously. Schowtjak et al. [120] used a two-step optimization process to identify viscoelastic material parameters and damage-related parameters. In the first step, they focused on identifying only the viscoelastic material parameters, i.e., the Yeoh and relaxation parameters, from homogeneous deformation states. In this step, the damage parameters are inactive. In the second step, they calibrated the damage-related parameters from the inhomogeneous deformation states, with the viscoelastic parameters identified in the first step fixed.

Schemmann et al. [416] calibrated the elastic material parameters in the first step, and the viscous material parameters in the second step. Affagard et al. [307] identified the normal and tangential cohesive parameters sequentially and separately, and then simultaneously optimized all parameters in a single analysis. Satošek et al. [263] used a two-stage calibration procedure to identify the out-of-plane plastic anisotropy behavior of sheet metal from an indentation test. In the first step, they calibrated the in-plane parameters of the YLD2004–18p yield function. Then, they identified the remaining out-of-plane shear parameters from a ball indentation test after fixing the calibrated in-plane parameters. This two-stage calibration procedure reduces the dimensionality of the parametric hyperspace to only four parameters in the second step, significantly simplifying the inverse identification procedure.

Data-assimilation is a process that integrates observational data with models to improve the accuracy of predictions. This process can employ various optimization methods, including both gradient-based and derivative-free algorithms. A recent study focused on using data assimilation for the inverse calibration of material model parameters through DIC measurements and finite element simulations, with the goal of predicting the deformation behavior of materials [110].

6.6 High Dimensional Parameter Space Optimization for Heterogeneous Material

Identification of a heterogeneous model through an ordinary optimization routine is computationally expensive and less robust [417] due to the inordinate number of material model parameters. Inverse identification therefore demands enhancements to the FEMU optimization, such as a double iterative optimization algorithm [257], new cost functions [404], and the application of a filter on the response field [299].

Considine et al. [418] identified the heterogeneous, orthotropic elastic parameters of a cellulose-fiber composite [419]. The heterogeneity is significant for cellulose-fiber composites due to material defects. In their work [418],

300 effective parameters are identified using the LM algorithm. The Jacobian matrix calculation in the LM algorithm requires 301 FEA evaluations per iteration. The LM algorithm is extremely time-consuming for such a large parameter hyperspace. Wu et al. [420] used GA and PSO algorithm to identify the spatially distribution of elastic modulus and Poisson's ratio of a rock material. Their method might also be very time consuming to identify varied parameters in 2000 elements. Borzeszkowski et al. [421] identified the heterogeneous material property distributions (up to 1089 unknown variables) using trust-region interior reflective approach. These works used ordinary optimization algorithms to calibrate the parameters in such a large parameter hyperspace, which is extremely time-consuming.

Gao et al. [256] identified the modulus gradient distribution of bamboo material by using a so-called double iterative technique, which is a combination of a fixed-point iteration method and the Nelder–Mead simplex algorithm. This optimization algorithm is the key to achieve reasonable efficiency with such a large number of parameters. This optimization approach has also been used to identify the modulus distribution of a graphite material [257] and the modulus field and Poisson's ratio field of a rock material [422]. Similar idea was also adopted by Kowalczyk [423] for identifying the orthotropic properties of composites. In this work, a heterogeneous parameter distribution is optimized during each iteration using the Gauss–Newton algorithm. The four orthotropic parameters are subsequently calculated as the average of the parameter fields. Witz et al. [424] used an image-based method to get the heterogeneous fiber orientation distribution of crimped mineral wool material. This prior knowledge enabled a significant reduction of the number of unknown elastic material parameters to four.

6.7 Initial Guess

In most cases, the parameter identification problem is highly non-convex. A good initial guess for the parameter set may therefore be the dominant factor influencing the parameter identification performance. This is particularly important for identifying complex material that involve a large number of material model parameters. Schulte et al. [425] summarized three typical strategies for parameter initialization:

- Randomly generating the initial guess for the optimization.
- Defining a physically meaningful range for each parameter and then randomly selecting each parameter within the defined range.
- Using the multi-step optimization strategy for parameter identification. The elastic parameters can be identified first and then fixed. The remaining parameters can then be identified more robustly.

In real-world applications, the first strategy is the worst choice, since it is costly and less robust. The second strategy is more effective, but requires extensive knowledge of the materials in question to constrain the parameters. This knowledge can come from experience or from literature; it can also be based on parameters for similar materials or theoretical calculation. The third strategy, as discussed in Sec. 6.4, permits more efficient and robust parameter identification.

In Ref. [425], a deep-learning-based method is proposed for parameter estimation. Initially, a dataset including a set of stress–strain curves is generated from numerical simulations based on constitutive parameters. This dataset is then used to train an artificial neural network (ANN). The trained ANN model can efficiently estimate the parameters from a given stress–strain curve. The estimated parameters are then used as the initial guess for optimization-based parameter identification using FEMU.

The accuracy requirement for the initial guess can be reduced to an extent by fine-tuning the optimization algorithm, optimization strategy and cost function. A hybrid approach that combines derivative-free and gradient-based algorithms can effectively balance convergence radius and convergence efficiency. A better cost function can enhance convexity, leading to better convergence.

6.8 Convergence Criteria

In most literature, the convergence criteria (also known as stop criteria) are routinely overlooked, as they are considered simple and highly user-dependent. However, convergence criteria are an essential aspect of any optimization algorithm, having a strong influence on the efficiency and accuracy of the algorithms. Here, we recommend several feasible criteria based on the literature.

- The algorithm stops when a preset iteration number threshold is reached [426, 427].
- The maximum increment of all parameters at current iteration falls below a threshold, e.g., 10^{-4} [143].
- The relative variation of the parameters (see below) falls below a threshold, such as 0.01% [336], 0.1% [257], 1% [258].

$$\max_k \left| \frac{p_k^{(j+1)} - p_k^{(j)}}{p_k^{(j)}} \right| < \text{Threshold} \quad (49)$$

- One other possible criterion [132, 428], taking the GN algorithm as an example, is that the Euclidean norm of the multiplication of the Jacobian matrix and the residual falls below a threshold (e.g., 10^{-5} for IDIC [132]).

7 Uncertainty Analysis

FEMU arrives at values for material model parameters through a complex and extended measurement process. A critical caveat is that these values are calibrated using a technique with a long measurement chain, where errors accumulate across three pillars: experimental, numerical and optimization. Once the parameters have been successfully identified, we are faced with the unavoidable question of how accurate and precise these material model parameters are. This question is challenging because FEMU relies on a material model that may not fully represent reality. MT1.0 also face these issues. What remains uncertain, however, is the level of accuracy in the calibrated material model parameters.

In this section, uncertainty analysis in FEMU is briefly reviewed. Uncertainty analysis is vital for evaluating the reliability of the identified results. There are two typical methods for evaluating identification uncertainty suggested in the literature: the Monte-Carlo method and the uncertainty propagation theory.

7.1 Monte-Carlo Method and Digital Twin

The Monte-Carlo method [429, 430] is an effective and versatile tool to determine the uncertainty of measurands [431]. It estimates identification uncertainty through repeated random sampling, which could be either from experiments or simulation. The most straightforward and accurate strategy is to repeat the identification on replicated real tests with the same configuration, assuming sufficient test repetition is feasible. This approach covers all possible sources of uncertainty in the characterization chain, with parameter uncertainty calculated as the standard deviation of each parameter. However, repeating experiments and parameter identification multiple times is often impractical due to inefficiency.

Integrating the Monte-Carlo method with the Digital Twin (DT) concept [281] is more practical. It can disentangle various error sources and investigate their impact on the identified parameters. DT has been widely used to evaluate the measurement uncertainty of optical measurement systems [432, 433]. DT can virtually mimic a real measurement system, considering various error contributors, such as the environment, the measurement device. Those contributors can then lead to the measurement uncertainty.

DT can also virtually simulate the real-world DIC test [434, 435] and FEMU identification. Figure 21a schematically illustrates the DT concept in FEMU. In DT, inputting the model parameters and the boundary condition into FEA allows us to numerically calculate the displacement fields. By applying the displacement fields to real speckle pattern images, the reference image and the deformed images can be

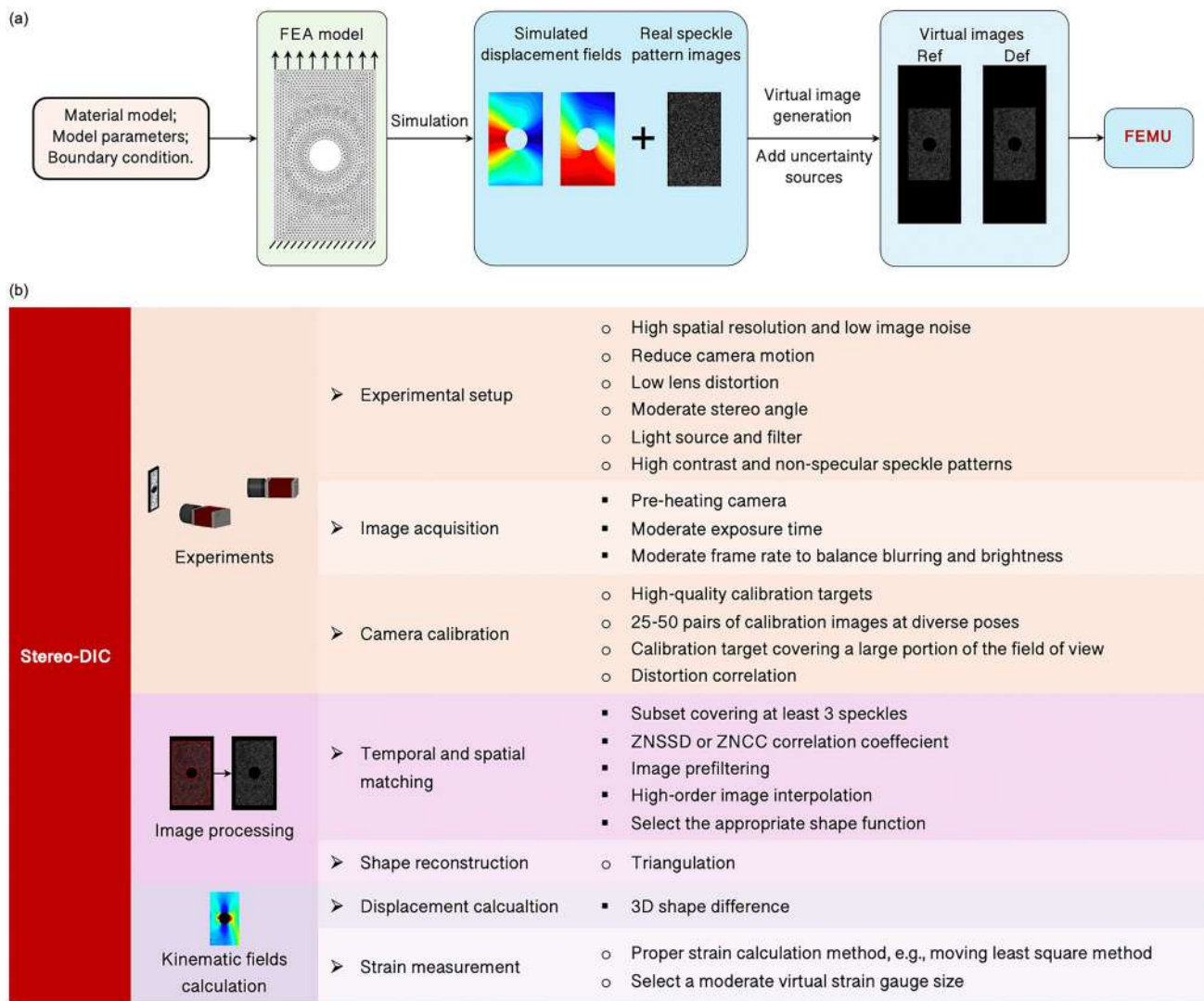


Fig. 21 Digital Twin for FEMU: **a** the schematic diagram for digital twin and **b** the error sources involved in the digital twin of stereo-DIC [121]

virtually generated. The uncertainty sources in DIC instruments can be added to the virtually generated images. FEMU can estimate the constitutive parameters from these virtual images. Running the virtual DIC test and FEMU identification several times in the DT can provide the distribution of the identified parameters. By comparing the identified parameters with the input material parameters, the parameter uncertainty in FEMU can be estimated.

DT is often employed to thoroughly examine error sources and their impact on identification. If all error sources can be quantified, DT can mimic the experiment, enabling the determination of uncertainty or confidence intervals for the identified parameters based on known material behavior. Various error sources in each step (Fig. 21b) in DIC, including shape function [436], lens distortion [437], subset size selection [438], speckle patterns [439], camera calibration [440], etc., may affect the predicted material parameters,

although it is challenging to quantify all these error sources in practice.

Some researchers employed the Monte-Carlo method to evaluate the uncertainty of FEMU. Gras et al. [164] evaluated the uncertainty of the identified out-of-plane shear modulus of a layer-to-layer interlocked woven composite. They numerically deformed a reference image using displacement fields from FEA with known material properties. To mimic real image uncertainty, they added random gray-scale noise, following a Gaussian distribution obtained from real tests. Two hundred simulated samples were identified by FEMU, with the uncertainty of each parameter calculated as the corresponding standard deviation. While this numerical approach requires less labor, it remains computationally expensive. Similar methods have also been used to evaluate the uncertainty of VFM [441].

In contrast to the bottom-up approach in DT, Maček et al. [442] developed guidelines for a two-stage error propagation model that produces more realistic confidence interval predictions based on a database of past DIC experiments. They measured the displacement error distribution of DIC from hundreds of real experiments that had taken place in a three-year span. The confidence intervals of inversely identified material parameters for several typical tests were determined from the displacement error using the Monte-Carlo method and sensitivity analysis. Furthermore, Sueki et al. [110] have suggested an FEMU method that utilizes Bayesian data assimilation and is capable of estimating material model parameters and their associated confidence intervals simultaneously.

Creating an accurate DT that replicates the entire measurement chain is a challenging task. Additionally, it does not account for material model errors. If the selected material model cannot perfectly describe the actual material behavior, the uncertainty predicted by the Monte-Carlo method might not be realistic. Another obstacle is the heavy computational burden involved in the Monte-Carlo method.

7.2 Uncertainty Propagation Theory

The other approach is based on the uncertainty propagation theory. This method can theoretically estimate the identification uncertainty from the measurement uncertainty. For GN algorithms, the uncertainty can be evaluated by the covariance matrix. The covariance matrix can be approximated as the inverse of the Hessian matrix at the converged state [52, 133, 233]. The covariance matrix can also be normalized to obtain the correlation matrix in order to evaluate the correlation between parameters. This is similar to the normalized Hessian matrix for sensitivity quantification.

Based on the covariance matrix, Neggers et al. [133] and Bertin et al. [40] derived the parameter uncertainty from the image noise and the applied force in FEMU-UFN. These works consider mainly the image noise, force noise, or displacement errors. However, they neglected other sources of uncertainty (e.g., the loading error, strain window selection, model selection, etc.), which might also be crucial for FEMU. The advantage of this method is the high efficiency, since it avoids the repeated FEMU optimization in Monte-Carlo method.

8 Open-Source FEMU Software: FEMU-DIC

We are accompanying the publication of this FEMU review paper by the release of FEMU-DIC,⁵ an open-source software package available on GitHub. The objective of this

software is to promote the use of FEMU by lowering the barrier of entry for new users. FEMU-DIC includes a standalone 2D-DIC software tool for kinematic field measurements, which can be seamlessly integrated with the FEMU code. Additionally, FEMU-OPEN is compatible with commercial DIC software such as that provided by MatchID and Correlated Solutions. FEMU-DIC is primarily written in MATLAB and is not intended to be a universal tool for all solid mechanics problems. Instead, it includes the basic functions necessary for FEMU. The default function of the software is to identify constitutive parameters in an orthotropic elastic model, which users can easily adapt it to other identification tasks. The default FEA platform is COMSOL, but the software can be extended to work with other FEA software.

We do not claim any novelty for the software, rather, it serves as a starting point for PhD researchers and new practitioners. We believe it will help readers to develop their own tools based on this review. This section provides insight into using FEMU-DIC, focusing on a case study of identifying orthotropic elasticity. The data used in this section can be downloaded from GitHub.

8.1 Software Description

To the best of the author's knowledge, FEMU-DIC is the first open-source project that includes both DIC software and FEMU components. The structure of FEMU-DIC is given in Fig. 22. The DIC software is a standalone tool that can be used on its own if the user is interested in the deformation fields that can be reliably measured using 2D-DIC. It is based on a local DIC algorithm and is limited to first-order shape functions. The users can manually designate polygonal ROIs with open holes or notches. Basic DIC settings such as subset size, step size, as well as strain window size can be easily set by the user. We carefully optimized the DIC software to ensure decent computational efficiency. The most time-consuming part of DIC, i.e., the image intensity interpolation, is implemented in C++ to enhance performance.

In FEMU-DIC, the FEA model is first built using commercial software COMSOL Multiphysics and then exported as a MATLAB script, which facilitates automatic parameter updating through the integration of COMSOL with MATLAB. FEMU- ϵ N was selected as the cost function in order to eliminate the impact of rigid-body motion. The optimization algorithms available in the software include the Gauss–Newton and Nelder–Mead algorithm. Users can select the appropriate algorithm based on their specific task. The Gauss–Newton algorithm is implemented using numerical differentiation, while the Nelder–Mead algorithm is sourced from the optimization toolbox in MATLAB. In our software, we first calculate the displacement difference between DIC and FEA. Strain calculation is then applied to

⁵ <https://github.com/BinChenOPEN/FEMU-DIC>.

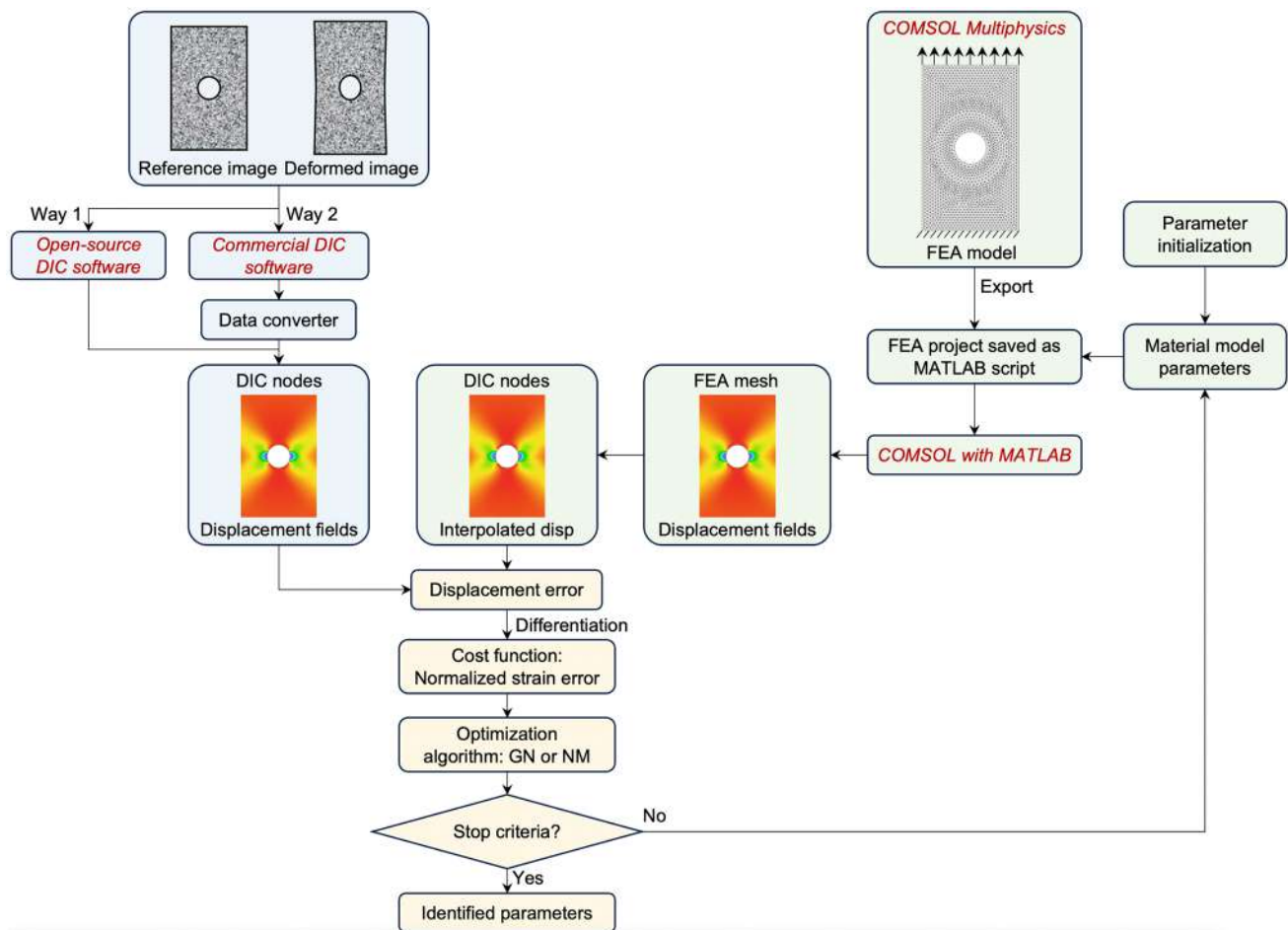


Fig. 22 Flowchart of FEMU-OPEN software

this displacement difference, allowing us to get the strain error directly. This method can level the strain tensor and VSG size. More information on the FEMU-OPEN software is found in Table 11. More details about the use of the software are available on GitHub. We may continue improving this open-source software in the future.

8.2 Case Study

We use the software to inversely identify the four orthotropic elastic parameters. The test is a uniaxial tensile test of a perforated strip sample. The sample has a thickness of 1 mm and an off-axis angle of 105° . The sample geometry information is given in Fig. 23a. A uniformly distributed force boundary condition with a value of 950 N is applied. Speckle pattern images are numerically generated to mimic the real test, as shown in Fig. 23b. Noise-free images are generated from the displacement fields simulated by FEA. The image size is 1501×601 pixels with a scale of 40 pixels/mm. The reference value of the constitutive parameters E_1 , E_2 , ν , G_{12} is 13.9 GPa, 5 GPa,

0.1, 2 GPa, respectively. In local DIC, the subset and step sizes are set as 21×21 and 5 pixels, respectively. The initial guess of these parameters is given as 0.9 times the ground truth values. The strain field in the images can be measured by DIC software. The strain fields measured by the open-source DIC software are shown in Fig. 23c with a strain window size of 21×21 points.

In the inverse parameter identification process, open-source or commercial DIC software (MatchID-2D or VIC-2D) is used to calculate the strain fields, while the GN and NM algorithms, respectively, are used for optimization. The identified parameters are given in Table 12, which shows the results obtained with different combinations of DIC software and optimization algorithms. All DIC software tools are capable of yielding decent parameters. Parameters E_2 and ν are identified with relatively large errors, indicating that the sensitivity of the strain fields with respect to these two parameters is low. This highlights the importance of test design in FEMU.

Overall, FEMU-OPEN provides an easy-to-use software for both method developers and users. The users can use it

Table 11 Summary of open-source software FEMU-OPEN

FEMU-OPEN components	Settings
<i>DIC</i>	
DIC platform	Open-source 2D-DIC software or commercial software (VIC-2D or MatchID-2D)
Method	Local DIC
Optimization algorithm	IC-GN
Shape function	First-order shape function
ROI selection	Rectangle and/or polygon
Strain calculation	Strain window method
<i>FEMU</i>	
FEMU framework	Direct-leveling method
Sample	Uniaxial tensile test of perforated strip sample
Boundary condition	Force boundary condition
Cost function	FEMU-eN
Optimization algorithm	Gauss–Newton or Nelder–Mead algorithm
Data fusion	Interpolate from FEA mesh to DIC nodes
Initial guess	Manually given
FEA solver	COMSOL Multiphysics
Converge criteria	A limited iteration number & the maximum relative parameter increment is larger than a threshold

directly to identify the four orthotropic elastic parameters. They can also easily modify the software to solve their own research problems.

9 Concluding Remarks and Future Goals

This section first emphasizes the value of FEMU, followed by a summary of the implementation steps. Subsequently, the challenges and future goals of FEMU are discussed.

9.1 Concluding Remarks

FEMU is a parameter identification technique which has been widely adopted to identify multiple constitutive material model parameters through one or a few tests. The technique has been attracting increasing attention from both academia and industry due to the widespread use of DIC techniques and the boom in computational power. The implementation of FEMU relies on the deep interconnection of the three pillars, experiments, simulation and optimization (see Fig. 24).

The major advantages of FEMU include its adaptability to different material models, its efficiency in reducing experimental efforts, and its potential for refining and selecting material models and straightforward calibration of complex material models. However, simultaneously identifying multiple parameters using FEMU is not an easy task. The identified parameters may have high uncertainty and may not

be unique for complex material models. Additionally, FEMU typically requires substantial experience for accurate calibration and the computational burden can also be an obstacle.

Several alternative approaches exist for each step of FEMU implementation. While the combination of different strategies for every step makes the FEMU technique highly flexible, it also complicates its use. In this review, we have examined the development and application of FEMU for calibrating material models. We have also reviewed the implementation details for the major steps in FEMU. The implementation details are summarized in Table 13, along with some remarks.

9.2 Challenges and Future Goals

FEMU is gradually transitioning into a mature technique but several challenges and disadvantages hinder its development. It is, however, continuously developing in terms of functionality. The technique would benefit from wider applicability, improved accuracy and enhanced robustness of the technique. The user experience is also important. There is a need for improvements in computational efficiency, standardization, user-friendly tools, etc.

9.2.1 Generic Test Design

The specimen geometry and loading path can significantly affect the accuracy and sensitivity of material parameter estimation. There is no universal test configuration for inverse parameter identification, but finding sample geometries that

Fig. 23 **a** Schematic diagram of the numerical test with the FEA mesh superimposed. **b** The numerically generated speckle pattern image. **c** The strain fields measured by the open-source DIC software

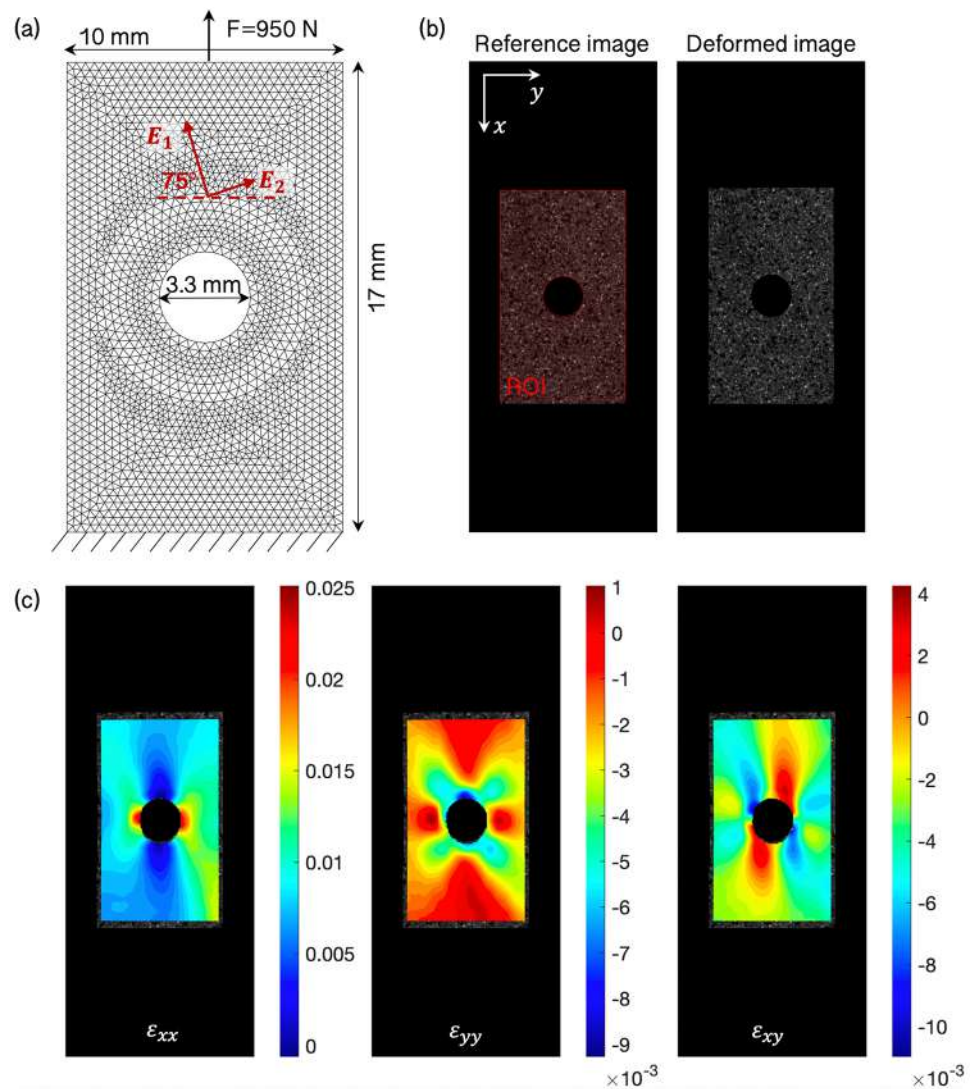


Table 12 The identified parameters and the FEMU-software running time with the combination of different DIC software and optimization algorithms

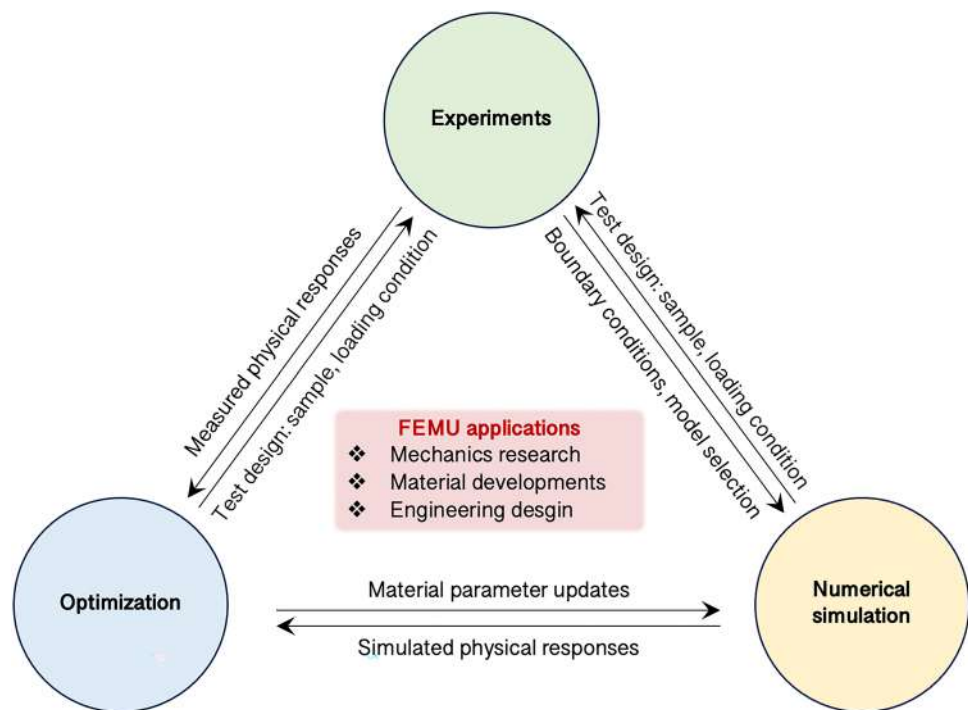
Parameters	E_1 (GPa)	E_2 (GPa)	ν	G_{12} (GPa)	Running time (s)
Reference value	13.9	5	0.1	2	–
GN + Open-source DIC	13.903	5.2991	0.1021	1.9999	76
GN + MatchID-2D	13.966	5.0489	0.0997	2.0024	76
GN + VIC-2D	13.917	5.0159	0.0987	1.9996	71
NM + Open-source DIC	13.863	5.3709	0.0980	1.9995	246
NM + MatchID-2D	13.913	5.2816	0.0873	2.0057	229
NM + VIC-2D	13.824	5.1887	0.0873	2.0069	202

work well for specific material models can simplify FEMU implementation and contribute to standardization.

9.2.2 Heterogeneous Material Characterization

Most studies focus on the calibration of average model parameters for homogeneous materials. However, materials such as wood and composites [443, 444] may have significant microstructural heterogeneity. It would be more

Fig. 24 Interdependence between the experiment, numerical simulation, and optimization in FEMU



accurate to model these materials using spatially distributed material parameters. For large structures, this would involve calibrating thousands of material parameters, which would necessitate the development of specific FEMU algorithms for this task. One promising approach is to use machine learning [445].

9.2.3 Multi-physics Model Calibration

FEMU is suitable not only for calibrating mechanical properties, but also for other physical properties, such as thermomechanical properties. By combining multiple physical responses, such as thermal, mechanical, electrical and hydrodynamical properties, FEMU can be used to identify different types of properties simultaneously. A basic requirement is that the physical responses of these properties can be experimentally measured and numerically simulated. In the scenario of multi-physics characterization, it is necessary to carefully evaluate the sensitivity and accuracy of material parameters, as the parameters may be strongly coupled.

9.2.4 High-Efficiency FEMU

A challenging issue in FEMU is the heavy computational burden from FEA, particularly for complex material models. The identification process can take hours or even days for a set of results. The most direct but costly solution is to invest in more powerful computational hardware. The other

possibility is to use parallel calculation. Efforts to develop new optimization algorithms, optimized cost functions and more accurate and simpler material models are also helpful. Integrating FEA and experimental measurement could eliminate some intermediate calculations and thus improve efficiency. However, this approach requires careful control of the core code in the FEA solver, as well as for speckle pattern image processing.

9.2.5 Deep Learning Aided Parameter Identification

The conventional inverse parameter identification methods, such as FEMU, involves multiple implementation procedures. The rapid development of deep learning or artificial intelligence (AI) provides a very promising and effective alternative to FEMU. The concept of a digital twin [446], which involves numerically mimicking real experiments, provides an efficient way to generate large datasets for training deep learning models [447].

In the scenario of FEMU, deep learning [20, 425, 445, 447–452] can contribute in several key steps such as cost function construction [453], strain measurement [454] and material model discovering [455], stress analysis [456, 457]. It can also identify the material parameters from experimental data using artificial neural networks (ANNs) [445, 449, 458–461], convolutional neural network (CNN) [447, 462, 463], and recurrent neural network (RNN) [464–466]. Andrade-Campos et al. [20] compared the deep-learning-based method with the VFM and FEMU methods. These

Table 13 Summary of the implementation details of FEMU based on kinematic field

FEMU implementation	Details and alternatives	Remarks
<i>Experiments</i>		
Test design	Heuristic-based design: uniaxial tensile/compression test, biaxial tensile test, other tests Optimization-based design: design based on stress and/or strain states, design based on sensitivity analysis, design based on simulated full identification	Test design includes specimen geometry and loading path design Design sample to get a highly heterogeneous strain state Aim for good identifiability of all parameters Consider manufacturing and measurement difficulty
Mechanical test	Sample manufacturing, sample alignment	A good mechanical test is a prerequisite for a good identification Compensate part of the mechanical test imperfection in simulation by using a Dirichlet boundary condition
Imaging setup selection	Imaging equipment: industrial camera, SEM, high-speed camera, etc. Imaging settings: image frame rate, exposure time, light source selection, etc.	High flexibility with respect to the imaging setup makes FEMU highly adaptable to different materials, scales, strain rates, etc
Kinematic field measurement techniques	General techniques: 2D-DIC, stereo-DIC, multi-view DIC, DVC, grid method, etc. Special DIC: high-speed DIC, high-temperature DIC, micro DIC and multi-scale DIC, discontinuous DIC	Balance between effective kinematic information, cost, and efficiency
DIC implementation details	Filtering, subset size, shape function, DIC algorithms, image prefiltering, virtual strain gauge size, image interpolation algorithms, etc.	Find a good balance between spatial resolution and measurement resolution for DIC
<i>Numerical simulation</i>		
Model selection	Plastic models, hyperelastic models, fracture models, elastic models, viscoelastic models, etc.	Adequately describe the real mechanical behavior Ensure good identifiability Consider efficiency and robustness by including reasonable number of parameters
Boundary condition	Dirichlet displacement boundary condition, nominal displacement boundary condition, force boundary condition, etc.	Select a suitable model for the studied material Match the boundary condition in the real test Attention should be paid to FEA robustness
Mesh	Element size, element type, etc.	Balance simulation accuracy and efficiency
FEA solver	Nonlinear static and explicit dynamic solver Simulation method includes FEM, BEM, etc.	Consider simulation efficiency Avoid convergence issues
<i>Iterative optimization</i>		
Cost function	Cost function based on force, displacement, strain, and/or other physical quantities Normalization or regularization terms in the cost function	Should have high sensitivity to all material parameters Significantly affects the identification uncertainty and efficiency Refine cost function is a good way to improve identification
Sensitivity analysis	Sensitivity based on Jacobian matrix, conditioning and collinearity evaluation, variance-based sensitivity analysis	Evaluate the identifiability of every parameter Facilitate test design
Data fusion	Coordinate system alignment: feature point detection and matching, specimen edge detection and matching Data point alignment: classical interpolation methods, mesh sharing strategy, field decomposition method	Small misalignment can have a surprisingly large effect

Table 13 (continued)

FEMU implementation	Details and alternatives	Remarks
Optimization	Algorithm: gradient-based algorithm, derivative-free algorithm, hybrid algorithm, trust-region algorithm Optimization strategy: one-step strategy, multi-step strategy Initial guess: random generation, selection from a physically meaningful range, multi-step optimization strategy Convergence criteria: maximum parameter increment, maximum iteration number	Balance efficiency, robustness, and accuracy. Accuracy and robustness should be the priority Appropriate algorithm and optimization strategy are especially important for complicated models
<i>Uncertainty analysis</i>	Monte-Carlo method, digital twin, uncertainty propagation theory	Evaluate the uncertainty of the identified parameters Critical but frequently neglected
Uncertainty evaluation		

methods show similar errors. The deep-learning-based method is independent of the initial guess but with disadvantage of high computational burden for database generation and model training.

9.2.6 Standardization

FEMU is primarily used in the academic world, despite its obvious benefits in engineering design. One reason for that is the lack of standardization for this technique. Even for experienced researchers, the identification results can vary significantly for the same material due to changes in specimen geometry, cost function, etc. It is also important to establish an accepted benchmark in terms of criteria and datasets to fairly evaluate the performance of different FEMU methods. Finally, the terminology used in FEMU needs to be clearly defined and standardized.

9.2.7 All-in-One User-Friendly Platform Development

FEMU is often implemented across multiple platforms: a commercial FEA solver for modeling, commercial or in-house DIC software for kinematic field measurement, and self-developed scripts for parameter identification. These separate platforms reduce convenience and introduce complexity, and potential data transfer errors. It is an obstacle that prevents more widespread use among engineers in the industry. An all-in-one user-friendly platform would be beneficial.

Acknowledgements The authors would like to acknowledge Dr. Yi Zhang from the department of Materials Engineering, KU Leuven, and Dr. Xiaole Li, postdoctoral researcher from King Abdullah University of Science and Technology, for the fruitful discussion. Dr. Erik Jungstedt from Mips AB, Sweden, is greatly acknowledged for his encouragement, careful review, and constructive comments to this work.

Author Contributions Bin Chen: conceptualization, software, investigation, formal analysis, data curation, writing—original draft & review & editing, visualization. Miroslav Halilović: writing—review & editing. Bojan Starman: writing—review & editing. Lars A. Berglund: supervision, writing—review & editing. Sam Coppieters: conceptualization, writing—original draft & review & editing.

Funding Open access funding provided by Royal Institute of Technology. BC and LB gratefully acknowledge the support from Knut and Alice Wallenberg foundation (KAW 2021.0311) and the HORIZON AI-TRANSPWOOD (AI-Driven Multiscale Methodology to Develop Transparent Wood as Sustainable Functional Material) project, Grant No. 101138191, co-funded by the European Union. SC and BS gratefully acknowledge the support from the Research Fund for Coal and Steel under grant agreement No 888153 (EU-RFCS 2019 project No. 888153 | vForm-xSteels). MH and BS acknowledge the financial support from the Slovenian Research Agency (research core funding No. P2-0263 and project funding No. L2-3172).

Data Availability No data was used for the research described in the article.

Declarations

Conflict of interest The authors have no conflict of interest to declare.

Open Access This article is licensed under a Creative Commons Attribution 4.0 International License, which permits use, sharing, adaptation, distribution and reproduction in any medium or format, as long as you give appropriate credit to the original author(s) and the source, provide a link to the Creative Commons licence, and indicate if changes were made. The images or other third party material in this article are included in the article's Creative Commons licence, unless indicated otherwise in a credit line to the material. If material is not included in the article's Creative Commons licence and your intended use is not permitted by statutory regulation or exceeds the permitted use, you will need to obtain permission directly from the copyright holder. To view a copy of this licence, visit <http://creativecommons.org/licenses/by/4.0/>.

References

- Rao SS (2018) Overview of finite element method. In: The finite element method in engineering. Elsevier, Amsterdam, pp 3–52. <https://doi.org/10.1016/B978-0-12-811768-2.00001-8>
- Conde M, Coppieters S, Andrade-Campos A (2024) Strategies for automatic constitutive model selection and recommendation. *Int J Mech Sci* 264:108813. <https://doi.org/10.1016/j.ijmecsci.2023.108813>
- Hou Y, Myung D, Park JK, Min J, Lee HR, El-Aty AA, Lee MG (2023) A review of characterization and modelling approaches for sheet metal forming of lightweight metallic materials. *Materials*. <https://doi.org/10.3390/ma16020836>
- Pierron F, Grédiac M (2021) Towards material testing 2.0. A review of test design for identification of constitutive parameters from full-field measurements. *Strain* 57:1–22. <https://doi.org/10.1111/str.12370>
- Yin Q (2014) Verfestigungs- und Schädigungsverhalten von Blechwerkstoffen im ebenen Torsionsversuch. http://d-nb.info/1051701430/04%0Ahttp://deposit.d-nb.de/cgi-bin/dokserv?id=4680179&prov=M&dok_var=1&dok_ext=htm
- Chen B, Chen W, Pan B (2020) High-precision video extensometer based on a simple dual field-of-view telecentric imaging system. *Measurement (Lond)* 166:108209. <https://doi.org/10.1016/j.measurement.2020.108209>
- Pierron F, Grédiac M (2012) The virtual fields method. Springer, New York. <https://doi.org/10.1007/978-1-4614-1824-5>
- Pierron F (2023) Material testing 2.0: a brief review. *Strain*. <https://doi.org/10.1111/str.12434>
- Coppieters S, Hakoyama T, Eyckens P, Nakano H, Van Bael A, Debruyne D, Kuwabara T (2018) On the synergy between physical and virtual sheet metal testing: calibration of anisotropic yield functions using a microstructure-based plasticity model. *Int J Mater Form*. <https://doi.org/10.1007/s12289-018-1444-1>
- Zhang Y, Yamanaka A, Cooreman S, Kuwabara T, Coppieters S (2023) Inverse identification of plastic anisotropy through multiple non-conventional mechanical experiments. *Int J Solids Struct* 285:112534. <https://doi.org/10.1016/j.ijsolstr.2023.112534>
- Andrade-Campos A, Thuillier S, Martins J, Carlone P, Tucci F, Valente R, Paulo RMF, Alves de Sousa RJ (2020) Integrated design in welding and incremental forming: material model calibration for friction stir welded blanks. *Procedia Manuf* 47:429–434. <https://doi.org/10.1016/j.promfg.2020.04.327>
- Toussaint E, Grédiac M, Pierron F (2006) The virtual fields method with piecewise virtual fields. *Int J Mech Sci* 48:256–264. <https://doi.org/10.1016/j.ijmecsci.2005.10.002>
- Grédiac M, Pierron F, Avril S, Toussaint E (2008) The virtual fields method for extracting constitutive parameters from full-field measurements: a review. *Strain* 42:233–253. <https://doi.org/10.1111/j.1475-1305.2006.tb01504.x>
- Florentin E, Lubineau G (2010) Identification of the parameters of an elastic material model using the constitutive equation gap method. *Comput Mech* 46:521–531. <https://doi.org/10.1007/s00466-010-0496-y>
- Claire D, Hild F, Roux S (2004) A finite element formulation to identify damage fields: the equilibrium gap method. *Int J Numer Methods Eng* 61:189–208. <https://doi.org/10.1002/nme.1057>
- Nguyen HN, Chamoin L, Ha Minh C (2022) mCRE-based parameter identification from full-field measurements: consistent framework, integrated version, and extension to nonlinear material behaviors. *Comput Methods Appl Mech Eng* 400:115461. <https://doi.org/10.1016/j.cma.2022.115461>
- Huang S, Feissel P, Villon P (2016) Modified constitutive relation error: an identification framework dealing with the reliability of information. *Comput Methods Appl Mech Eng* 311:1–17. <https://doi.org/10.1016/j.cma.2016.06.030>
- Martins JMP, Andrade-Campos A, Thuillier S (2018) Comparison of inverse identification strategies for constitutive mechanical models using full-field measurements. *Int J Mech Sci* 145:330–345. <https://doi.org/10.1016/j.ijmecsci.2018.07.013>
- Vargas R, Negggers J, Canto RB, Rodrigues JA, Hild F (2018) Comparison of two full-field identification methods for the wedge splitting test on a refractory. *J Eur Ceram Soc* 38:5569–5579. <https://doi.org/10.1016/j.jeurceramsoc.2018.07.039>
- Andrade-Campos A, Bastos N, Conde M, Gonçalves M, Henriques J, Lourenço R, Martins JMP, Oliveira MG, Prates P, Rumor L (2022) On the inverse identification methods for forming plasticity models using full-field measurements. *IOP Conf Ser Mater Sci Eng* 1238:012059. <https://doi.org/10.1088/1757-899x/1238/1/012059>
- Mašín D, Tamagnini C, Viggiani G, Costanzo D (2006) Directional response of a reconstituted fine-grained soil—Part II: performance of different constitutive models. *Int J Numer Anal Methods Geomech* 30:1303–1336. <https://doi.org/10.1002/nag>
- Gao W (2018) A comprehensive review on identification of the geomaterial constitutive model using the computational intelligence method. *Adv Eng Inform* 38:420–440. <https://doi.org/10.1016/j.aei.2018.08.021>
- Yin ZY, Jin YF, Shen SL, Huang HW (2017) An efficient optimization method for identifying parameters of soft structured clay by an enhanced genetic algorithm and elastic–viscoplastic model. *Acta Geotech* 12:849–867. <https://doi.org/10.1007/s11440-016-0486-0>
- Yin ZY, Jin YF, Shen JS, Hicher PY (2018) Optimization techniques for identifying soil parameters in geotechnical engineering: comparative study and enhancement. *Int J Numer Anal Methods Geomech* 42:70–94. <https://doi.org/10.1002/nag.2714>
- Kadlíček T, Janda T, Šejnoha M, Mašín D, Najser J, Beneš Š (2022) Automated calibration of advanced soil constitutive models. Part I: hypoplastic sand. *Acta Geotech* 17:3421–3438. <https://doi.org/10.1007/s11440-021-01441-0>
- Pal S, Wathugala GW, Kundu S (1996) Calibration of a constitutive model using genetic algorithms. *Comput Geotech* 19:325–348. [https://doi.org/10.1016/S0266-352X\(96\)00006-7](https://doi.org/10.1016/S0266-352X(96)00006-7)
- Ereiz S, Duvnjak I, Fernando Jiménez-Alonso J (2022) Review of finite element model updating methods for structural applications. *Structures* 41:684–723. <https://doi.org/10.1016/j.istruc.2022.05.041>

28. Blachowski B (2019) Modal sensitivity based sensor placement for damage identification under sparsity constraint. *Period Polytech Civ Eng* 63:432–445. <https://doi.org/10.3311/PPci.13888>
29. Vakil Baghmisheh MT, Peimani M, Sadeghi MH, Etefagh MM, Tabrizi AF (2012) A hybrid particle swarm-Nelder-Mead optimization method for crack detection in cantilever beams. *Appl Soft Comput J* 12:2217–2226. <https://doi.org/10.1016/j.asoc.2012.03.030>
30. Fang SE, Perera R (2011) Damage identification by response surface based model updating using D-optimal design. *Mech Syst Signal Process* 25:717–733. <https://doi.org/10.1016/j.ymssp.2010.07.007>
31. Li Z, Feng D, Feng MQ, Xu X (2017) System identification of the suspension tower of Runyang Bridge based on ambient vibration tests. *Smart Struct Syst* 19:523–538. <https://doi.org/10.12989/sss.2017.19.5.523>
32. Qin S, Zhou YL, Cao H, Wahab MA (2018) Model updating in complex bridge structures using kriging model ensemble with genetic algorithm. *KSCIE J Civ Eng* 22:3567–3578. <https://doi.org/10.1007/s12205-017-1107-7>
33. Wang FY, Xu YL, Zhan S (2017) Multi-scale model updating of a transmission tower structure using Kriging meta-method. *Struct Control Health Monit* 24:1–16. <https://doi.org/10.1002/stc.1952>
34. Cuadrado M, Pernas-Sánchez J, Artero-Guerrero JA, Varas D (2020) Model updating of uncertain parameters of carbon/epoxy composite plates using digital image correlation for full-field vibration measurement. *Measurement (Lond)* 159:107783. <https://doi.org/10.1016/j.measurement.2020.107783>
35. Flaschel M (2023). Automated discovery of material models in continuum solid mechanics Thesis. <https://doi.org/10.3929/ethz-b-000602750>
36. Neggers J, Mathieu F, Hild F, Roux S, Swiergiel N (2017) Improving full-field identification using progressive model enrichments. *Int J Solids Struct* 118–119:213–223. <https://doi.org/10.1016/j.ijsolstr.2017.03.013>
37. Lava P, Jones EMC, Wittevrongel L, Pierron F (2020) Validation of finite-element models using full-field experimental data: levelling finite-element analysis data through a digital image correlation engine. *Strain* 56:1–17. <https://doi.org/10.1111/str.12350>
38. Wang Y, Coppieters S, Lava P, Debruyne D (2016) Anisotropic yield surface identification of sheet metal through stereo finite element model updating. *J Strain Anal Eng Des* 51:598–611. <https://doi.org/10.1177/0309324716666437>
39. Fayad SS, Jones EMC, Seidl DT, Reu PL, Lambros J (2023) On the importance of direct-levelling for constitutive material model calibration using digital image correlation and finite element model updating. *Exp Mech* 63:467–484. <https://doi.org/10.1007/s11340-022-00926-7>
40. Bertin MBR, Hild F, Roux S (2016) Optimization of a cruciform specimen geometry for the identification of constitutive parameters based upon full-field measurements. *Strain* 52:307–323. <https://doi.org/10.1111/str.12178>
41. Denys K, Coppieters S, Cooreman S, Debruyne D (2017) Alternative method for the identification of the strain hardening behaviour along the rolling direction of coil. *Strain* 53:1–15. <https://doi.org/10.1111/str.12231>
42. Schmaltz S, Willner K (2014) Comparison of different biaxial tests for the inverse identification of sheet steel material parameters. *Strain* 50:389–403. <https://doi.org/10.1111/str.12080>
43. Guery A, Hild F, Latourte F, Roux S (2016) Identification of crystal plasticity parameters using DIC measurements and weighted FEMU. *Mech Mater* 100:55–71. <https://doi.org/10.1016/j.mechmat.2016.06.007>
44. Denys K, Coppieters S, Seefeldt M, Debruyne D (2016) Multi-DIC setup for the identification of a 3D anisotropic yield surface of thick high strength steel using a double perforated specimen. *Mech Mater* 100:96–108. <https://doi.org/10.1016/j.mechmat.2016.06.011>
45. Haddadi H, Belhabib S (2012) Improving the characterization of a hardening law using digital image correlation over an enhanced heterogeneous tensile test. *Int J Mech Sci* 62:47–56. <https://doi.org/10.1016/j.ijmecsci.2012.05.012>
46. Conde M, Zhang Y, Henriques J, Coppieters S, Andrade-Campos A (2023) Design and validation of a heterogeneous interior notched specimen for inverse material parameter identification. *Finite Elem Anal Des* 214:103866. <https://doi.org/10.1016/j.finel.2022.103866>
47. Tomičević Z, Kodvanj J, Hild F (2016) Characterization of the nonlinear behavior of nodular graphite cast iron via inverse identification-analysis of uniaxial tests. *Eur J Mech A* 59:140–154. <https://doi.org/10.1016/j.euromechsol.2016.02.010>
48. Wang W, Mottershead JE, Sebastian CM, Patterson EA (2011) Shape features and finite element model updating from full-field strain data. *Int J Solids Struct* 48:1644–1657. <https://doi.org/10.1016/j.ijsolstr.2011.02.010>
49. Zhang D, Zhang XM, Ding H (2018) Inverse identification of material plastic constitutive parameters based on the DIC determined workpiece deformation fields in orthogonal cutting. *Procedia CIRP* 71:134–139. <https://doi.org/10.1016/j.procir.2018.05.085>
50. Pottier T, Toussaint F, Vacher P (2011) Contribution of heterogeneous strain field measurements and boundary conditions modeling in inverse identification of material parameters. *Eur J Mech A* 30:373–382. <https://doi.org/10.1016/j.euromechsol.2010.10.001>
51. Seon G, Makeev A, Schaefer JD, Justusson B (2019) Measurement of interlaminar tensile strength and elastic properties of composites using open-hole compression testing and digital image correlation. *Appl Sci (Switzerland)*. <https://doi.org/10.3390/app9132647>
52. Gras R, Leclerc H, Hild F, Roux S, Schneider J (2015) Identification of a set of macroscopic elastic parameters in a 3D woven composite: uncertainty analysis and regularization. *Int J Solids Struct* 55:2–16. <https://doi.org/10.1016/j.ijsolstr.2013.12.023>
53. Hao Z, Ji X, Deng L, Ke H, Liu L (2021) Measurement of multiple mechanical properties for polymer composites using digital image correlation at elevated temperatures. *Mater Des* 198:109349. <https://doi.org/10.1016/j.matdes.2020.109349>
54. Avril S, Pierron F (2007) General framework for the identification of constitutive parameters from full-field measurements in linear elasticity. *Int J Solids Struct* 44:4978–5002. <https://doi.org/10.1016/j.ijsolstr.2006.12.018>
55. Passieux JC, Bugarin F, David C, Périé JN, Robert L (2015) Multiscale displacement field measurement using digital image correlation: application to the identification of elastic properties. *Exp Mech* 55:121–137. <https://doi.org/10.1007/s11340-014-9872-4>
56. Vargas R, Tsitova A, Bernachy-Barbe F, Bary B, Canto RB, Hild F (2020) On the identification of cohesive zone model for curved crack in mortar. *Strain* 56:1–22. <https://doi.org/10.1111/str.12364>
57. Ferreira MDC, Venturini WS, Hild F (2011) On the analysis of notched concrete beams: From measurement with digital image correlation to identification with boundary element method of a cohesive model. *Eng Fract Mech* 78:71–84. <https://doi.org/10.1016/j.engfracmech.2010.10.008>
58. Jungstedt E, Östlund S, Berglund LA (2022) Transverse fracture toughness of transparent wood biocomposites by FEM updating with cohesive zone fracture modeling. *Compos Sci Technol* 225:1–10. <https://doi.org/10.1016/j.compscitech.2022.109492>
59. Jungstedt E, Oliaei E, Li L, Östlund S, Berglund LA (2022) Mechanical behavior of all-lignocellulose composites—comparing micro- and nanoscale fibers using strain field data and FEM

- updating. *Composites A*. <https://doi.org/10.1016/j.compositesa.2022.107095>
60. Dastidar AG, Ayadi A, Lacrampe MF (2020) Reliability of hybrid inverse identification based on stereo-dic measurements to assess HIPS hyperelastic parameters: case of isothermal tensile loads. *Procedia Manuf* 47:933–939. <https://doi.org/10.1016/j.promfg.2020.04.287>
 61. Gain AL, Carroll J, Paulino GH, Lambros J (2011) A hybrid experimental/numerical technique to extract cohesive fracture properties for mode-I fracture of quasi-brittle materials. *Int J Fract* 169:113–131. <https://doi.org/10.1007/s10704-010-9578-2>
 62. Bastos G, Sales L, Di Cesare N, Tayeb A, Le Cam J-B (2021) Inverse-Pagerank-particle swarm optimisation for inverse identification of hyperelastic models: a feasibility study. *J Rubber Res* 24:447–460. <https://doi.org/10.1007/s42464-021-00113-8>
 63. Charlès S, Le Cam JB (2020) Inverse identification of constitutive parameters from heat source fields: a local approach applied to hyperelasticity. *Strain* 56:1–16. <https://doi.org/10.1111/str.12334>
 64. Giton M, Caro-Bretelle AS, Ienny P (2006) Hyperelastic behaviour identification by a forward problem resolution: application to a tear test of a silicone-rubber. *Strain* 42:291–297. <https://doi.org/10.1111/j.1475-1305.2006.00285.x>
 65. Boyer G, Molimard J, Ben Tkaya M, Zahouani H, Pericoi M, Avril S (2013) Assessment of the in-plane biomechanical properties of human skin using a finite element model updating approach combined with an optical full-field measurement on a new tensile device. *J Mech Behav Biomed Mater* 27:273–282. <https://doi.org/10.1016/j.jmbbm.2013.05.024>
 66. Affagard JS, Bensamoun SF, Feissel P (2014) Development of an inverse approach for the characterization of in vivo mechanical properties of the lower limb muscles. *J Biomech Eng* 136:1–8. <https://doi.org/10.1115/1.4028490>
 67. Affagard JS, Feissel P, Bensamoun SF (2015) Identification of hyperelastic properties of passive thigh muscle under compression with an inverse method from a displacement field measurement. *J Biomech* 48:4081–4086. <https://doi.org/10.1016/j.jbiomech.2015.10.007>
 68. Henriques J, Xavier J, Andrade-Campos A (2022) Identification of orthotropic elastic properties of wood by a synthetic image approach based on digital image correlation. *Materials* 15:1–24. <https://doi.org/10.3390/ma15020625>
 69. Henriques J, Xavier J, Andrade-Campos A (2021) Identification of orthotropic elastic properties of wood by digital image correlation and finite element model updating techniques. *Procedia Struct Integr* 37:25–32. <https://doi.org/10.1016/j.prostr.2022.02.047>
 70. Vargas R, Canto RB, Hild F (2021) On the calibration of cohesive parameters for refractories from notch opening displacements in wedge splitting tests. *J Eur Ceram Soc* 41:7348–7361. <https://doi.org/10.1016/j.jeurceramsoc.2021.07.011>
 71. Vargas R, Canto RB, Hild F (2022) Cohesive properties of refractory castable at 600 °C: effect of sintering and testing temperature. *J Eur Ceram Soc* 42:6733–6749. <https://doi.org/10.1016/j.jeurceramsoc.2022.06.070>
 72. Doitrand A, Estevez R, Thibault M, Leplay P (2020) Fracture and cohesive parameter identification of refractories by digital image correlation up to 1200°C. *Exp Mech* 60:577–590. <https://doi.org/10.1007/s11340-020-00584-7>
 73. Kavanagh KT, Clough RW (1971) Finite element applications in the characterization of elastic solids. *Int J Solids Struct* 7:11–23. [https://doi.org/10.1016/0020-7683\(71\)90015-1](https://doi.org/10.1016/0020-7683(71)90015-1)
 74. Iding RH, Pister KS, Taylor RL (1974) Identification of nonlinear elastic solids by a finite element method. *Comput Methods Appl Mech Eng* 4:121–142. [https://doi.org/10.1016/0045-7825\(74\)90030-9](https://doi.org/10.1016/0045-7825(74)90030-9)
 75. Kavanagh KT (1972) Extension of classical experimental techniques for characterizing composite-material behavior. *Exp Mech* 12:50–56. <https://doi.org/10.1007/bf02320791>
 76. Farhat C, Hemez FM (1993) Updating finite element dynamic models using an element-by-element sensitivity methodology. *AIAA J* 31:1702–1711. <https://doi.org/10.2514/3.11833>
 77. Peters WH, Ranson WF (1982) Digital imaging techniques in experimental stress analysis. *Opt Eng*. <https://doi.org/10.1117/12.7972925>
 78. Peters WH, Ranson WF, Sutton MA, Chu TC, Anderson J (1983) Application of digital correlation methods to rigid body mechanics. *Opt Eng*. <https://doi.org/10.1117/12.7973231>
 79. Chu TC, Ranson WF, Sutton MA (1985) Applications of digital-image-correlation techniques to experimental mechanics. *Exp Mech* 25:232–244. <https://doi.org/10.1007/BF02325092>
 80. Sutton M, Wolters W, Peters W, Ranson W, McNeill S (1983) Determination of displacements using an improved digital correlation method. *Image Vis Comput* 1:133–139. [https://doi.org/10.1016/0262-8856\(83\)90064-1](https://doi.org/10.1016/0262-8856(83)90064-1)
 81. Sutton M, Mingqi C, Peters W, Chao Y, McNeill S (1986) Application of an optimized digital correlation method to planar deformation analysis. *Image Vis Comput* 4:143–150. [https://doi.org/10.1016/0262-8856\(86\)90057-0](https://doi.org/10.1016/0262-8856(86)90057-0)
 82. Schreier H, Orteu J-J, Sutton MA (2009) *Image correlation for shape, motion and deformation measurements*. Springer, Boston. <https://doi.org/10.1007/978-0-387-78747-3>
 83. Pan B (2018) Digital image correlation for surface deformation measurement: historical developments, recent advances and future goals. *Meas Sci Technol* 29:082001. <https://doi.org/10.1088/1361-6501/aac55b>
 84. Huntley JM (1998) Automated fringe pattern analysis in experimental mechanics: a review. *J Strain Anal Eng Des* 33:105–125. <https://doi.org/10.1243/0309324981512850>
 85. Grédiac M, Sur F, Blaysat B (2016) The grid method for in-plane displacement and strain measurement: a review and analysis. *Strain* 52:205–243. <https://doi.org/10.1111/str.12182>
 86. Mahnken R, Stein E (1996) A unified approach for parameter identification of inelastic material models in the frame of the finite element method. *Comput Methods Appl Mech Eng* 136:225–258. [https://doi.org/10.1016/0045-7825\(96\)00991-7](https://doi.org/10.1016/0045-7825(96)00991-7)
 87. Meuwissen MHH, Oomens CWJ, Baaijens FPT, Petterson R, Janssen JD (1998) Determination of the elasto-plastic properties of aluminium using a mixed numerical-experimental method. *J Mater Process Technol* 75:204–211. [https://doi.org/10.1016/S0924-0136\(97\)00366-X](https://doi.org/10.1016/S0924-0136(97)00366-X)
 88. Grédiac M, Pierron F (1998) A T-shaped specimen for the direct characterization of orthotropic materials. *Int J Numer Methods Eng* 41:293–309. [https://doi.org/10.1002/\(SICI\)1097-0207\(19980130\)41:2%3c293::AID-NME284%3e3.0.CO;2-Y](https://doi.org/10.1002/(SICI)1097-0207(19980130)41:2%3c293::AID-NME284%3e3.0.CO;2-Y)
 89. Hild F, Roux S (2006) Measuring stress intensity factors with a camera: integrated digital image correlation (I-DIC). *Comptes Rendus Mécanique* 334:8–12. <https://doi.org/10.1016/j.crme.2005.11.002>
 90. Ephane ST, Roux S, Hild F (2006) Stress intensity factor measurements from digital image correlation: post-processing and integrated approaches. *Int J Fract* 140:141–157. <https://doi.org/10.1007/s10704-006-6631-2>
 91. Leclerc H, Périé JN, Roux S, Hild F (2009) Integrated digital image correlation for the identification of mechanical properties. In: *Lecture Notes in Computer Science (Including Subseries Lecture Notes in Artificial Intelligence and Lecture Notes in Bioinformatics)*, LNCS, vol 5496, pp 161–171. https://doi.org/10.1007/978-3-642-01811-4_15
 92. Lava P, Cooreman S, Coppeters S, De Strycker M, Debruyne D (2009) Assessment of measuring errors in DIC using deformation

- fields generated by plastic FEA. *Opt Lasers Eng* 47:747–753. <https://doi.org/10.1016/j.optlaseng.2009.03.007>
93. Avril S, Bonnet M, Bretelle AS, Grédiac M, Hild F, Lenny P, Latourte F, Lemosse D, Pagano S, Pagnacco E, Pierron F (2008) Overview of identification methods of mechanical parameters based on full-field measurements. *Exp Mech* 48:381–402. <https://doi.org/10.1007/s11340-008-9148-y>
 94. Lecompte D, Cooreman S, Coppieters S, Vantomme J, Sol H, Debruyne D (2009) Parameter identification for anisotropic plasticity model using digital image correlation: comparison between uni-axial and bi-axial tensile testing. *Eur J Comput Mech* 18:393–418. <https://doi.org/10.3166/ejcm.18.393-418>
 95. Markiewicz É, Langrand B, Notta-Cuvier D (2017) A review of characterisation and parameters identification of materials constitutive and damage models: From normalised direct approach to most advanced inverse problem resolution. *Int J Impact Eng* 110:371–381. <https://doi.org/10.1016/j.ijimpeng.2017.01.028>
 96. Hild F, Roux S (2006) Digital image correlation: from displacement measurement to identification of elastic properties—a review. *Strain* 42:69–80. <https://doi.org/10.1111/j.1475-1305.2006.00258.x>
 97. Prates PA, Pereira AFG, Sakharova NA, Oliveira MC, Fernandes JV (2016) Inverse strategies for identifying the parameters of constitutive laws of metal sheets. *Adv Mater Sci Eng*. <https://doi.org/10.1155/2016/4152963>
 98. Bruno L (2018) Mechanical characterization of composite materials by optical techniques: a review. *Opt Lasers Eng* 104:192–203. <https://doi.org/10.1016/j.optlaseng.2017.06.016>
 99. Neggers J, Allix O, Hild F, Roux S (2018) Big data in experimental mechanics and model order reduction: today’s challenges and tomorrow’s opportunities. *Arch Comput Methods Eng* 25:143–164. <https://doi.org/10.1007/s11831-017-9234-3>
 100. Mahnken R (2017) Identification of material parameters for constitutive equations. In: *Encyclopedia of computational mechanics*, 2nd edn. Wiley, Hoboken, pp 1–21. <https://doi.org/10.1002/9781119176817.ecm2043>
 101. Andrade-Campos A, Coppieters S, Strano M (2022) Optimization and inverse analysis in metal forming: scientific state-of-the-art and recent trends. *Int J Mater Form*. <https://doi.org/10.1007/s12289-022-01690-8>
 102. Römer U, Hartmann S, Tröger JA, Anton D, Wessels H, Flaschel M, De Lorenzis L (2024) Reduced and all-at-once approaches for model calibration and discovery in computational solid mechanics. <http://arxiv.org/abs/2404.16980>
 103. Güner A, Soyarslan C, Brosius A, Tekkaya AE (2012) Characterization of anisotropy of sheet metals employing inhomogeneous strain fields for Yld 2000–2D yield function. *Int J Solids Struct* 49:3517–3527. <https://doi.org/10.1016/j.ijsolstr.2012.05.001>
 104. Barlat F, Brem JC, Yoon JW, Chung K, Dick RE, Lege DJ, Pourboghrat F, Choi SH, Chu E (2003) Plane stress yield function for aluminum alloy sheets—Part 1: theory. *Int J Plast* 19:1297–1319. [https://doi.org/10.1016/S0749-6419\(02\)00019-0](https://doi.org/10.1016/S0749-6419(02)00019-0)
 105. Rose L, Menzel A (2020) Optimisation based material parameter identification using full field displacement and temperature measurements. *Mech Mater* 145:103292. <https://doi.org/10.1016/j.mechmat.2019.103292>
 106. Thoby JD, Fourest T, Langrand B, Notta-Cuvier D, Markiewicz E (2022) Robustness of specimen design criteria for identification of anisotropic mechanical behaviour from heterogeneous mechanical fields. *Comput Mater Sci* 207:111260. <https://doi.org/10.1016/j.commatsci.2022.111260>
 107. Zhang Y, Van Bael A, Andrade-Campos A, Coppieters S (2022) Parameter identifiability analysis: mitigating the non-uniqueness issue in the inverse identification of an anisotropic yield function. *Int J Solids Struct* 243:111543. <https://doi.org/10.1016/j.ijsolstr.2022.111543>
 108. Hartmann S, Gilbert RR (2018) Identifiability of material parameters in solid mechanics. *Arch Appl Mech* 88:3–26. <https://doi.org/10.1007/s00419-017-1259-4>
 109. Sewerin F (2020) On the local identifiability of constituent stress–strain laws for hyperelastic composite materials. *Comput Mech* 65:853–876. <https://doi.org/10.1007/s00466-019-01798-w>
 110. Sueki S, Ishii A, Coppieters S, Yamanaka A (2023) Inverse characterization of a material model using an ensemble-based four-dimensional variational method. *Int J Solids Struct* 279:112350. <https://doi.org/10.1016/j.ijsolstr.2023.112350>
 111. Maček A, Starman B, Mole N, Halilović M (2020) Calibration of advanced yield criteria using uniaxial and heterogeneous tensile test data. *Metals (Basel)*. <https://doi.org/10.3390/met10040542>
 112. Meuwissen MHH (1998) An inverse method for the mechanical characterisation of metals. Eindhoven University of Technology, Eindhoven
 113. Lecompte D (2007) Elasto-plastic material parameter identification by inverse modelling of static tests using digital image correlation. Free University of Brussels, Belgium
 114. Cooreman S (2008) Identification of the plastic material behaviour through full-field displacement measurements and inverse methods. Free University of Brussels, Belgium
 115. Wang Y (2015) Uncertainty quantification of digital image correlation and the impact on material identification. KU Leuven, Belgium
 116. Souto N (2015) Computational design of a technological mechanical test for material characterization by inverse analysis. Materials. Université de Bretagne Sud, Vannes
 117. Denys K (2017) Investigation into the plastic material behaviour up to fracture of thick HSS using multi-DIC and FEMU. KU Leuven, Belgium
 118. Odde Z, Solav D (2023) Identifiability of soft tissue constitutive parameters from in-vivo macro-indentation. *J Mech Behav Biomed Mater* 140:105708. <https://doi.org/10.1016/j.jmbbm.2023.105708>
 119. Elouneq A, Sutula D, Chambert J, Lejeune A, Bordas SPA, Jacquet E (2021) An open-source FEniCS-based framework for hyperelastic parameter estimation from noisy full-field data: application to heterogeneous soft tissues. *Comput Struct* 255:106620. <https://doi.org/10.1016/j.compstruc.2021.106620>
 120. Schowtjak A, Schulte R, Clausmeyer T, Ostwald R, Tekkaya AE, Menzel A (2022) ADAPT—a diversely applicable parameter identification tool: overview and full-field application examples. *Int J Mech Sci* 213:106840. <https://doi.org/10.1016/j.ijmecsci.2021.106840>
 121. Bigger R, Blaysat B, Boo C, Grever M, Hu J, Jones A, Klein M, Raghavan K, Reu P, Schmidt T, Siebert T, Simenson M, Turner D, Vieira A, Weikert T (2018) A good practices guide for digital image correlation. *Int Digit Image Correl Soc*. <https://doi.org/10.32720/idics/gpg.ed1>
 122. Louar MA, Belkacem B, Ousji H, Pyl L, Vantomme J (2022) Investigation of the strain rate hardening behaviour of glass fibre reinforced epoxy under blast loading. *Proc Inst Mech Eng C* 236:10667–10680. <https://doi.org/10.1177/0954406220936320>
 123. Maček A, Urevc J, Halilović M (2021) Flat specimen shape recognition based on full-field optical measurements and registration using mapping error minimization method. *Strojnicki Vestnik/J Mech Eng* 67:203–213. <https://doi.org/10.5545/sv-jme.2021.7111>
 124. Dong YL, Pan B (2017) A review of speckle pattern fabrication and assessment for digital image correlation. *Exp Mech* 57:1161–1181. <https://doi.org/10.1007/s11340-017-0283-1>
 125. Zhang Y (n.d.) Towards a practical engineering tool for inverse calibration of plastic behavior of sheet metals

126. Avril S, Feissel P, Pierron F, Villon P (2010) Comparison of two approaches for differentiating full-field data in solid mechanics. *Meas Sci Technol*. <https://doi.org/10.1088/0957-0233/21/1/015703>
127. Henriques J, Conde M, Andrade-Campos A, Xavier J (2022) Identification of swift law parameters using FEMU by a synthetic image DIC-based approach. *Key Eng Mater* 926:2211–2221. <https://doi.org/10.4028/p-33un7m>
128. Guildenbecher DR, Jones EMC, Hall EM, Reu PL, Miller TJ, Perez F, Thompson AD, Ball JP (2022) 3D optical diagnostics for explosively driven deformation and fragmentation. *Int J Impact Eng* 162:104142. <https://doi.org/10.1016/j.ijimpeng.2021.104142>
129. Zhao J, Li Y, Zhang H, Liu Z, Xie H, Liu S (2023) Characterization of thermo-mechanical parameters of nickel-based single crystal superalloys under high-temperature by modified I-DIC method. *Opt Laser Technol* 163:109371. <https://doi.org/10.1016/j.optlastec.2023.109371>
130. Ruybalid AP, Hoefnagels JPM, van der Sluis O, Geers MGD (2016) Comparison of the identification performance of conventional FEM updating and integrated DIC. *Int J Numer Methods Eng* 106:298–320. <https://doi.org/10.1002/nme.5127>
131. Ruybalid AP, Hoefnagels JPM, van der Sluis O, van Maris MPFHL, Geers MGD (2019) Mixed-mode cohesive zone parameters from integrated digital image correlation on micrographs only. *Int J Solids Struct* 156–157:179–193. <https://doi.org/10.1016/j.ijsolstr.2018.08.010>
132. Neggers J, Hoefnagels JPM, Geers MGD, Hild F, Roux S (2015) Time-resolved integrated digital image correlation. *Int J Numer Methods Eng* 103:157–182. <https://doi.org/10.1002/nme.4882>
133. Neggers J, Mathieu F, Hild F, Roux S (2019) Simultaneous full-field multi-experiment identification. *Mech Mater* 133:71–84. <https://doi.org/10.1016/j.mechmat.2019.03.001>
134. Réthoré J (2010) A fully integrated noise robust strategy for the identification of constitutive laws from digital images. *Int J Numer Methods Eng* 84:631–660. <https://doi.org/10.1002/nme.2908>
135. Réthoré J, Muhibullah T, Elguedj M, Coret P, Chaudet A (2013) Combescure, robust identification of elasto-plastic constitutive law parameters from digital images using 3D kinematics. *Int J Solids Struct* 50:73–85. <https://doi.org/10.1016/j.ijsolstr.2012.09.002>
136. Kleinendorst SM, Hoefnagels JPM, Geers MGD (2019) Mechanical Shape Correlation: a novel integrated digital image correlation approach. *Comput Methods Appl Mech Eng* 345:983–1006. <https://doi.org/10.1016/j.cma.2018.10.014>
137. Hild F, Bouterf A, Chamoin L, Leclerc H, Mathieu F, Neggers J, Pled F, Tomičević Z, Roux S (2016) Toward 4D mechanical correlation. *Adv Model Simul Eng Sci*. <https://doi.org/10.1186/s40323-016-0070-z>
138. Jaillin C, Bouterf A, Poncelet M, Roux S (2017) In situ μ CT-scan mechanical tests: fast 4D mechanical identification. *Exp Mech* 57:1327–1340. <https://doi.org/10.1007/s11340-017-0305-z>
139. Leclerc H, Roux S, Hild F (2015) Projection savings in CT-based digital volume correlation. *Exp Mech* 55:275–287. <https://doi.org/10.1007/s11340-014-9871-5>
140. Taillandier-Thomas T, Roux S, Hild F (2016) Soft route to 4D tomography. *Phys Rev Lett* 117:1–5. <https://doi.org/10.1103/PhysRevLett.117.025501>
141. Zhou M, Xie H (2019) An identification method of mechanical properties of materials based on the full-field measurement method based on the fringe pattern. *Strain* 55:1–15. <https://doi.org/10.1111/str.12326>
142. Lindström SB, Wemming H, Kapidžić Z, Loukil MS, Segersäll M (2023) Integrated digital image correlation for mechanical characterization of carbon fiber-reinforced polymer plates. *Compos Struct* 305:116501. <https://doi.org/10.1016/j.compsstruct.2022.116501>
143. Bertin M, Hild F, Roux S, Mathieu F, Leclerc H, Aïmedieu P (2016) Integrated digital image correlation applied to elasto-plastic identification in a biaxial experiment. *J Strain Anal Eng Des* 51:118–131. <https://doi.org/10.1177/0309324715614759>
144. Gaynutdinova L, Rokoš O, Havelka J, Pultarová I, Zeman J (2023) Bayesian approach to micromechanical parameter identification using integrated digital image correlation. *Int J Solids Struct* 280:112388. <https://doi.org/10.1016/j.ijsolstr.2023.112388>
145. Rokoš O, Peerlings RHJ, Hoefnagels JPM, Geers MGD (2023) Integrated digital image correlation for micro-mechanical parameter identification in multiscale experiments. *Int J Solids Struct* 267:112130. <https://doi.org/10.1016/j.ijsolstr.2023.112130>
146. Kosin V, Fau A, Jailin C, Hild F, Wick T (2024) Parameter identification of a phase-field fracture model using integrated digital image correlation. *Comput Methods Appl Mech Eng* 420:116689. <https://doi.org/10.1016/j.cma.2023.116689>
147. Baldi A (2014) Residual stress analysis of orthotropic materials using integrated digital image correlation. *Exp Mech* 54:1279–1292. <https://doi.org/10.1007/s11340-014-9859-1>
148. Baldi A (2019) On the implementation of the integral method for residual stress measurement by integrated digital image correlation. *Exp Mech* 59:1007–1020. <https://doi.org/10.1007/s11340-019-00503-5>
149. Zhao J, Hou Y, Liu Z, Xie H, Liu S (2019) Optical distortion evaluation based on the integrated colour CCD Moiré method. *Opt Express* 27:34626. <https://doi.org/10.1364/oe.27.034626>
150. Charbal A, Dufour JE, Guery A, Hild F, Roux S, Vincent L, Poncelet M (2016) Integrated digital image correlation considering gray level and blur variations: application to distortion measurements of IR camera. *Opt Lasers Eng* 78:75–85. <https://doi.org/10.1016/j.optlaseng.2015.09.011>
151. Dufour JE, Hild F, Roux S (2014) Integrated digital image correlation for the evaluation and correction of optical distortions. *Opt Lasers Eng* 56:121–133. <https://doi.org/10.1016/j.optlaseng.2013.12.015>
152. Vermeij T, Hoefnagels JPM (2018) A consistent full-field integrated DIC framework for HR-EBSD. *Ultramicroscopy* 191:44–50. <https://doi.org/10.1016/j.ultramic.2018.05.001>
153. Humphreys FJ (2001) Grain and subgrain characterisation by electron backscatter diffraction. *J Mater Sci* 36:3833–3854. <https://doi.org/10.1023/A:1017973432592>
154. Shi Q, Loïsnard D, Dan C, Zhang F, Zhong H, Li H, Li Y, Chen Z, Wang H, Roux S (2021) Calibration of crystal orientation and pattern center of EBSD using integrated digital image correlation. *Mater Charact*. <https://doi.org/10.1016/j.matchar.2021.111206>
155. Shi Q, Roux S, Latourte F, Hild F (2019) Estimation of elastic strain by integrated image correlation on electron diffraction patterns. *Ultramicroscopy* 199:16–33. <https://doi.org/10.1016/j.ultramic.2019.02.001>
156. Ruybalid AP, Hoefnagels JPM, Van Der Sluis O, Geers MGD (2016) Performance assessment of integrated digital image correlation versus FEM updating. Conference proceedings of the society for experimental mechanics series 9:11–15. https://doi.org/10.1007/978-3-319-21765-9_2
157. Mathieu F, Leclerc H, Hild F, Roux S (2015) Estimation of elasto-plastic parameters via weighted FEMU and integrated-DIC. *Exp Mech* 55:105–119. <https://doi.org/10.1007/s11340-014-9888-9>
158. Nsengiyumva G, Kim YR (2022) Field displacement-based inverse method for elastic and viscoelastic constitutive properties. *Exp Mech* 62:1553–1568. <https://doi.org/10.1007/s11340-022-00876-0>

159. Machaček J, Staubach P, Tavera CEG, Wichtmann T, Zachert H (2022) On the automatic parameter calibration of a hypoplastic soil model. *Acta Geotech* 17:5253–5273. <https://doi.org/10.1007/s11440-022-01669-4>
160. Jang TJ, Kim JB, Shin H (2021) Identification of plastic constitutive Johnson-Cook model parameters by optimization-based inverse method. *J Comput Des Eng* 8:1082–1097. <https://doi.org/10.1093/jcde/qwab033>
161. Yang X, Berglund LA (2021) Structural and ecofriendly holocellulose materials from wood: microscale fibers and nanoscale fibrils. *Adv Mater*. <https://doi.org/10.1002/adma.202001118>
162. Martins JMP, Andrade-Campos A, Thuillier S (2019) Calibration of anisotropic plasticity models using a biaxial test and the virtual fields method. *Int J Solids Struct* 172–173:21–37. <https://doi.org/10.1016/j.ijsolstr.2019.05.019>
163. Liu G, Zhang R, Yi Y, Sun L, Shi L, Jiang H, Ma S (2019) Experimental and simulation study on stress concentration of graphite components in tension. *Mech Mater* 130:88–94. <https://doi.org/10.1016/j.mechmat.2019.01.010>
164. Gras R, Leclerc H, Roux S, Otin S, Schneider J, Périé JN (2013) Identification of the out-of-plane shear modulus of a 3D woven composite. *Exp Mech* 53:719–730. <https://doi.org/10.1007/s11340-012-9683-4>
165. Siddiqui MZ, Khan SZ, Khan MA, Shahzad M, Khan KA, Nisar S (2018) A novel test configuration design method for inverse identification of in-plane moduli of a composite plate under the PFEUM framework. *Strain* 54:1–22. <https://doi.org/10.1111/str.12280>
166. Chen C, Kuang Y, Zhu S, Burgert I, Keplinger T, Gong A, Li T, Berglund L, Eichhorn SJ, Hu L (2020) Structure–property–function relationships of natural and engineered wood. *Nat Rev Mater* 5:642–666. <https://doi.org/10.1038/s41578-020-0195-z>
167. Sjöström E (1993) The structure of wood. In: *Wood chemistry*. Elsevier, Amsterdam, pp 1–20. <https://doi.org/10.1016/B978-0-08-092589-9.50005-X>
168. Li Y, Fu Q, Yu S, Yan M, Berglund L (2016) Optically transparent wood from a nanoporous cellulosic template: combining functional and structural performance. *Biomacromol* 17:1358–1364. <https://doi.org/10.1021/acs.biomac.6b00145>
169. Latourte F, Chrysochoos A, Pagano S, Wattrisse B (2008) Elastoplastic behavior identification for heterogeneous loadings and materials. *Exp Mech* 48:435–449. <https://doi.org/10.1007/s11340-007-9088-y>
170. Sutton MA, Yan JH, Avril S, Pierron F, Adee SM (2008) Identification of heterogeneous constitutive parameters in a welded specimen: uniform stress and virtual fields methods for material property estimation. *Exp Mech* 48:451–464. <https://doi.org/10.1007/s11340-008-9132-6>
171. Tucci F, Andrade Campos A, Thuillier S, Carlone P (2022) Calibration of the elasto-plastic properties of friction stir welded blanks in aluminum alloy AA6082. *Key Eng Mater* 926:2183–2192. <https://doi.org/10.4028/p-3a8e45>
172. Marckmann G, Verron E (2006) Comparison of hyperelastic models for rubber-like materials. *Rubber Chem Technol* 79:835–858. <https://doi.org/10.5254/1.3547969>
173. Hajhashemkhani M, Hematiyan MR, Goenezen S (2018) Inverse determination of elastic constants of a hyper-elastic member with inclusions using simple displacement/length measurements. *J Strain Anal Eng Des* 53:529–542. <https://doi.org/10.1177/0309324718792452>
174. De-Carvalho R, Valente RAF, Andrade-Campos A (2011) Optimization strategies for non-linear material parameters identification in metal forming problems. *Comput Struct* 89:246–255. <https://doi.org/10.1016/j.compstruc.2010.10.002>
175. Chen Z, Scheffer T, Seibert H, Diebels S (2013) Macroindentation of a soft polymer: identification of hyperelasticity and validation by uni/biaxial tensile tests. *Mech Mater* 64:111–127. <https://doi.org/10.1016/j.mechmat.2013.05.003>
176. Campos T, Araújo R, Xavier J, Nguyễn Q, Dourado N, Morais J, Pereira F (2024) Identification of apple fruit-skin constitutive laws by full-field methods using uniaxial tensile loading. *Materials*. <https://doi.org/10.3390/ma17030700>
177. Dusfour G, LeFloc'h S, Cañadas P, Ambard D (2020) Heterogeneous mechanical hyperelastic behavior in the porcine annulus fibrosus explained by fiber orientation: an experimental and numerical approach. *J Mech Behav Biomed Mater*. <https://doi.org/10.1016/j.jmbbm.2020.103672>
178. Zhao J, Dong J, Liu Z, Xie H (2019) Characterization method of mechanical properties of rubber materials based on in-situ stereo finite-element-model updating. *Polym Test* 79:106015. <https://doi.org/10.1016/j.polymertesting.2019.106015>
179. Genovese K, Lamberti L, Pappalettere C (2006) Mechanical characterization of hyperelastic materials with fringe projection and optimization techniques. *Opt Lasers Eng* 44:423–442. <https://doi.org/10.1016/j.optlaseng.2005.06.003>
180. Gent AN (1996) A new constitutive relation for rubber. *Rubber Chem Technol* 69:59–61. <https://doi.org/10.5254/1.3538357>
181. Horgan CO (2015) The remarkable Gent constitutive model for hyperelastic materials. *Int J Non Linear Mech* 68:9–16. <https://doi.org/10.1016/j.ijnonlinmec.2014.05.010>
182. Rossi M, Lattanzi A, Morichelli L, Martins JMP, Thuillier S, Andrade-Campos A, Coppieters S (2022) Testing methodologies for the calibration of advanced plasticity models for sheet metals: a review. *Strain* 58:1–28. <https://doi.org/10.1111/str.12426>
183. Hill R (1948) A theory of the yielding and plastic flow of anisotropic metals. *Proc R Soc Lond A* 193:281–297. <https://doi.org/10.1098/rspa.1948.0045>
184. Coppieters S, Cooreman S, Sol H, Van Houtte P, Debruyne D (2011) Identification of the post-necking hardening behaviour of sheet metal by comparison of the internal and external work in the necking zone. *J Mater Process Technol* 211:545–552. <https://doi.org/10.1016/j.jmatprotec.2010.11.015>
185. Martins JMP, Thuillier S, Andrade-Campos A (2020) Calibration of anisotropic plasticity models with an optimized heterogeneous test and the virtual fields method. In: *Conference proceedings of the society for experimental mechanics series*, pp 25–32. https://doi.org/10.1007/978-3-030-30098-2_5
186. Zhang Y, Gothivarekar S, Conde M, Van de Velde A, Paermenier B, Andrade-Campos A, Coppieters S (2022) Enhancing the information-richness of sheet metal specimens for inverse identification of plastic anisotropy through strain fields. *Int J Mech Sci* 214:106891. <https://doi.org/10.1016/j.ijmecsci.2021.106891>
187. Wang Z, Zang S, Chu X, Zhang S, Lionel L (2019) Identification of 7B04 aluminum alloy anisotropy yield criteria with conventional test and Pottier test at elevated temperature. *Results Phys* 15:102655. <https://doi.org/10.1016/j.rinp.2019.102655>
188. Oliveira MG, Thuillier S, Andrade-Campos A (2020) Analysis of heterogeneous tests for sheet metal mechanical behavior. *Procedia Manuf* 47:831–838. <https://doi.org/10.1016/j.promfg.2020.04.259>
189. Zhang S, Leotoing L, Guines D, Thuillier S, Zang SL (2014) Calibration of anisotropic yield criterion with conventional tests or biaxial test. *Int J Mech Sci* 85:142–151. <https://doi.org/10.1016/j.ijmecsci.2014.05.020>
190. Souto N, Andrade-Campos A, Thuillier S (2016) A numerical methodology to design heterogeneous mechanical tests. *Int J Mech Sci* 107:264–276. <https://doi.org/10.1016/j.ijmecsci.2016.01.021>
191. Andrade-Campos A, Aquino J, Martins JMP, Coelho B (2019) On the design of innovative heterogeneous sheet metal tests using a shape optimization approach. *Metals (Basel)*. <https://doi.org/10.3390/met9030371>

192. Souto N, Andrade-Campos A, Thuillier S (2015) Material parameter identification within an integrated methodology considering anisotropy, hardening and rupture. *J Mater Process Technol* 220:157–172. <https://doi.org/10.1016/j.jmatprotec.2015.01.017>
193. Aquino J, Andrade-Campos AG, Martins JMP, Thuillier S (2019) Design of heterogeneous mechanical tests: numerical methodology and experimental validation. *Strain* 55:1–18. <https://doi.org/10.1111/str.12313>
194. Swift HW (1952) Plastic instability under plane stress. *J Mech Phys Solids* 1:1–18. [https://doi.org/10.1016/0022-5096\(52\)90002-1](https://doi.org/10.1016/0022-5096(52)90002-1)
195. Prates PA, Oliveira MC, Fernandes JV (2016) Identification of material parameters for thin sheets from single biaxial tensile test using a sequential inverse identification strategy. *Int J Mater Form* 9:547–571. <https://doi.org/10.1007/s12289-015-1241-z>
196. Aguir H, BelHadjSalah H, Hambli R (2011) Parameter identification of an elasto-plastic behaviour using artificial neural networks-genetic algorithm method. *Mater Des* 32:48–53. <https://doi.org/10.1016/j.matdes.2010.06.039>
197. Voce E (1948) The relationship between stress and strain for homogeneous deformation. *J Inst Met* 74:537–562
198. Denys K, Coppieters S, Debruyne D (2018) On the identification of a high-resolution multi-linear post-necking strain hardening model. *Comptes Rendus—Mecanique* 346:712–723. <https://doi.org/10.1016/j.crme.2018.06.002>
199. Kleemola HJ, Nieminen MA (1974) On the Strain-hardening parameters of metals. *Metall Trans* 5:1863–1866. <https://doi.org/10.1007/BF02644152>
200. Robert L, Velay V, Decultot N, Ramde S (2012) Identification of hardening parameters using finite element models and full-field measurements: Some case studies. *J Strain Anal Eng Des* 47:3–17. <https://doi.org/10.1177/0309324711430022>
201. Zhang H, Coppieters S, Jiménez-Peña C, Debruyne D (2019) Inverse identification of the post-necking work hardening behaviour of thick HSS through full-field strain measurements during diffuse necking. *Mech Mater* 129:361–374. <https://doi.org/10.1016/j.mechmat.2018.12.014>
202. Coppieters S, Traphöner H, Stiebert F, Balan T, Kuwabara T, Tekkaya AE (2022) Large strain flow curve identification for sheet metal. *J Mater Process Technol*. <https://doi.org/10.1016/j.jmatprotec.2022.117725>
203. Coppieters S, Kuwabara T (2014) Identification of post-necking hardening phenomena in ductile sheet metal. *Exp Mech* 54:1355–1371. <https://doi.org/10.1007/s11340-014-9900-4>
204. Denys K, Coppieters S, Debruyne D (2017) Identification of a 3D anisotropic yield surface using a multi-DIC setup. In: Conference proceedings of the society for experimental mechanics series, pp 101–104. https://doi.org/10.1007/978-3-319-51439-0_24
205. Conde M, Henriques J, Coppieters S, Andrade-Campos A (2022) Parameter identification of swift law using a FEMU-based approach and an innovative heterogeneous mechanical test. *Key Eng Mater* 926:2238–2246. <https://doi.org/10.4028/p-1n7i0p>
206. Prates PA, Oliveira MC, Fernandes JV (2014) A new strategy for the simultaneous identification of constitutive laws parameters of metal sheets using a single test. *Comput Mater Sci* 85:102–120. <https://doi.org/10.1016/j.commatsci.2013.12.043>
207. Cooreman S, Lecompte D, Sol H, Vantomme J, Debruyne D (2008) Identification of mechanical material behavior through inverse modeling and DIC. *Exp Mech* 48:421–433. <https://doi.org/10.1007/s11340-007-9094-0>
208. Rossi M, Lattanzi A, Barlat F (2018) A general linear method to evaluate the hardening behaviour of metals at large strain with full-field measurements. *Strain* 54:1–17. <https://doi.org/10.1111/str.12265>
209. Kajberg J, Lindkvist G (2004) Characterisation of materials subjected to large strains by inverse modelling based on in-plane displacement fields. *Int J Solids Struct* 41:3439–3459. <https://doi.org/10.1016/j.ijsolstr.2004.02.021>
210. Rojčiček J, Čermák M, Halama R, Paška Z, Vaško M (2021) Material model identification from set of experiments and validation by DIC. *Math Comput Simul* 189:339–367. <https://doi.org/10.1016/j.matcom.2021.04.007>
211. Dugdale DS (1960) Yielding of steel sheets containing slits. *J Mech Phys Solids* 8:100–104. [https://doi.org/10.1016/0022-5096\(60\)90013-2](https://doi.org/10.1016/0022-5096(60)90013-2)
212. Barenblatt GI (1962) The mathematical theory of equilibrium cracks in brittle fracture (initial experiment for hydrogel as a medium for...). *Adv Appl Mech* 7:55–129
213. Wu JY, Nguyen VP, Nguyen CT, Sutula D, Sinaie S, Bordas SPA (2020) Phase-field modeling of fracture. *Adv Appl Mech* 53:1–183. <https://doi.org/10.1016/bs.aams.2019.08.001>
214. Moës N, Belytschko T (2002) Extended finite element method for cohesive crack growth. *Eng Fract Mech* 69:813–833. [https://doi.org/10.1016/S0013-7944\(01\)00128-X](https://doi.org/10.1016/S0013-7944(01)00128-X)
215. van den Bosch MJ, Schreurs PJG, Geers MGD (2006) An improved description of the exponential Xu and Needleman cohesive zone law for mixed-mode decohesion. *Eng Fract Mech* 73:1220–1234. <https://doi.org/10.1016/j.engfracmech.2005.12.006>
216. Fedele R, Ciani A, Galantucci L, Casalegno V, Ventrella A, Ferraris M (2014) Characterization of innovative CFC/Cu joints by full-field measurements and finite elements. *Mater Sci Eng A* 595:306–317. <https://doi.org/10.1016/j.msea.2013.12.015>
217. Shen B, Paulino GH (2011) Direct extraction of cohesive fracture properties from digital image correlation: a hybrid inverse technique. *Exp Mech* 51:143–163. <https://doi.org/10.1007/s11340-010-9342-6>
218. Bao G, Suo Z (1992) Remarks on crack-bridging concepts. *Appl Mech Rev* 45:355–366. <https://doi.org/10.1115/1.3119764>
219. Alfano M, Furgiuele F, Leonardi A, Maletta C, Paulino GH (2009) Mode I fracture of adhesive joints using tailored cohesive zone models. *Int J Fract* 157:193–204. <https://doi.org/10.1007/s10704-008-9293-4>
220. Alfano M, Lubineau G, Paulino GH (2015) Global sensitivity analysis in the identification of cohesive models using full-field kinematic data. *Int J Solids Struct* 55:66–78. <https://doi.org/10.1016/j.ijsolstr.2014.06.006>
221. Park K, Paulino GH, Roesler JR (2009) A unified potential-based cohesive model of mixed-mode fracture. *J Mech Phys Solids* 57:891–908. <https://doi.org/10.1016/j.jmps.2008.10.003>
222. Alloisio M, Gasser TC (2023) Fracture of the porcine aorta-Part 2: FEM modelling and inverse parameter identification. *Acta Biomater* 167:158–170. <https://doi.org/10.1016/j.actbio.2023.06.020>
223. Vargas R, Canto RB, Smaniotto B, Hild F (2023) Calibration of cohesive parameters for a castable refractory using 4D tomographic data and realistic crack path from in-situ wedge splitting test. *J Eur Ceram Soc* 43:676–691. <https://doi.org/10.1016/j.jeurceramsoc.2022.09.040>
224. Vargas R, Neggers J, Canto RB, Rodrigues JA, Hild F (2019) Analysis of a castable refractory using the wedge splitting test and cohesive zone model. *J Eur Ceram Soc* 39:3903–3914. <https://doi.org/10.1016/j.jeurceramsoc.2019.03.009>
225. Dai Y, Gruber D, Jin S, Harmuth H (2017) Modelling and inverse investigation of the fracture process for a magnesia spinel refractory using a heterogeneous continuum model. *Eng Fract Mech* 182:438–448. <https://doi.org/10.1016/j.engfracmech.2017.05.005>
226. Shen B, Stanciulescu I, Paulino GH (2010) Inverse computation of cohesive fracture properties from displacement fields. *Inverse Probl Sci Eng* 18:1103–1128. <https://doi.org/10.1080/17415977.2010.512661>

227. Jailin T, Tardif N, Desquines J, Chaudet P, Coret M, Baidetto MC, Georgenthum V (2022) FEMU based identification of the creep behavior of Zircaloy-4 claddings under simulated RIA thermo-mechanical conditions. *J Nucl Mater*. <https://doi.org/10.1016/j.jnucmat.2022.153542>
228. James JD, Spittle JA, Brown SGR, Evans RW (2001) A review of measurement techniques for the thermal expansion coefficient of metals and alloys at elevated temperatures. *Meas Sci Technol* 12:1–15. <https://doi.org/10.1088/0957-0233/12/3/201>
229. Dong J, Liu Z, Gao J (2017) Multi-parameter inversion and thermo-mechanical deformation decoupling using I-DIC. *Exp Mech* 57:31–39. <https://doi.org/10.1007/s11340-016-0203-9>
230. Rose L, Menzel A (2021) Identification of thermal material parameters for thermo-mechanically coupled material models: verification and model dependency. *Meccanica* 56:393–416. <https://doi.org/10.1007/s11012-020-01267-2>
231. Gao F, Macquaire B, Zhang Y, Bellet M (2022) A new localized inverse identification method for high temperature testing under resistive heating: application to the elastic-viscoplastic behaviour of L-PBF processed In718. *Strain* 58:1–25. <https://doi.org/10.1111/str.12409>
232. Campello D, Tardif N, Moula M, Baidetto MC, Coret M, Desquines J (2017) Identification of the steady-state creep behavior of Zircaloy-4 claddings under simulated loss-of-coolant accident conditions based on a coupled experimental/numerical approach. *Int J Solids Struct* 115–116:190–199. <https://doi.org/10.1016/j.ijsolstr.2017.03.016>
233. Archer T, Berny M, Beauchêne P, Hild F (2020) Creep behavior identification of an environmental barrier coating using full-field measurements. *J Eur Ceram Soc* 40:5704–5718. <https://doi.org/10.1016/j.jeurceramsoc.2020.06.009>
234. Kolymbas D (2000) The misery of constitutive modelling. In: *Constitutive modelling of granular materials*, pp 11–24. https://doi.org/10.1007/978-3-642-57018-6_1
235. Peshave A, Pierron F, Lava P, Moens D, Vandepitte D (2024) Metrics to evaluate constitutive model fitness based on DIC experiments. *Strain*. <https://doi.org/10.1111/str.12473>
236. Flaschel M, Kumar S, De Lorenzis L (2023) Automated discovery of generalized standard material models with EUCLID. *Comput Methods Appl Mech Eng* 405:115867. <https://doi.org/10.1016/j.cma.2022.115867>
237. Gábor A, Villaverde AF, Banga JR (2017) Parameter identifiability analysis and visualization in large-scale kinetic models of biosystems. *BMC Syst Biol* 11:1–16. <https://doi.org/10.1186/s12918-017-0428-y>
238. Robert L, Velay V, Decultot N, Ramde S (2012) Identification of hardening parameters using finite element models and full-field measurements: some case studies. *J Strain Anal Eng Des* 47:3–17. <https://doi.org/10.1177/0309324711430022>
239. Jenny P, Caro-Bretelle A-S, Pagnacco E (2009) Identification from measurements of mechanical fields by finite element model updating strategies. *Eur J Comput Mech*. <https://doi.org/10.13052/ejcm.18.353-376>
240. Belhabib S, Haddadi H, Gaspérini M, Vacher P (2008) Heterogeneous tensile test on elastoplastic metallic sheets: comparison between FEM simulations and full-field strain measurements. *Int J Mech Sci* 50:14–21. <https://doi.org/10.1016/j.jimecsci.2007.05.009>
241. Jacquet N, Tardif N, Elguedj T, Garnier C (2020) Elasto-viscoplastic buckling of thick anisotropic shells: numerical buckling predictions and experiments, American Society of Mechanical Engineers, Pressure Vessels and Piping Division (Publication) PVP 3, pp 1–10. <https://doi.org/10.1115/PVP2020-21491>.
242. Gajewski M, Kowalewski L (2016) Inverse analysis and DIC as tools to determine material parameters in isotropic metal plasticity models with isotropic strain hardening. *Materialpruefung/Mater Test* 58:818–825. <https://doi.org/10.3139/120.110925>
243. Grédiac M, Pierron F (2006) Applying the virtual fields method to the identification of elasto-plastic constitutive parameters. *Int J Plast* 22:602–627. <https://doi.org/10.1016/j.ijplas.2005.04.007>
244. Meraghni F, Nouri H, Bourgeois N, Czarnota C, Lory P (2011) Parameters identification of fatigue damage model for short glass fiber reinforced polyamide (PA6-GF30) using digital image correlation. *Procedia Eng* 10:2110–2116. <https://doi.org/10.1016/j.proeng.2011.04.349>
245. Rossi M, Fabrice P (2012) Identification of the plastic behaviour in the post-necking regime using a three dimensional reconstruction technique. *Key Eng Mater* 504–506:703–708. <https://doi.org/10.4028/www.scientific.net/KEM.504-506.703>
246. Kim JH, Barlat F, Pierron F, Lee MG (2014) Determination of anisotropic plastic constitutive parameters using the virtual fields method. *Exp Mech* 54:1189–1204. <https://doi.org/10.1007/s11340-014-9879-x>
247. Starman B, Vrh M, Koc P, Halilović M (2019) Shear test-based identification of hardening behaviour of stainless steel sheet after onset of necking. *J Mater Process Technol* 270:335–344. <https://doi.org/10.1016/j.jmatprotec.2019.03.010>
248. Zhang S, Léotoing L, Guines D, Thuillier S (2015) Potential of the cross biaxial test for anisotropy characterization based on heterogeneous strain field. *Exp Mech* 55:817–835. <https://doi.org/10.1007/s11340-014-9983-y>
249. Coppieters S, Hakoyama T, Debruyne D, Takahashi S, Kuwabara T (2018) Inverse Yield Locus Identification using a biaxial tension apparatus with link mechanism and displacement fields. *J Phys Conf Ser*. <https://doi.org/10.1088/1742-6596/1063/1/012039>
250. Garbowski T, Maier G, Novati G (2012) On calibration of orthotropic elastic-plastic constitutive models for paper foils by biaxial tests and inverse analyses. *Struct Multidiscip Optim* 46:111–128. <https://doi.org/10.1007/s00158-011-0747-3>
251. Teaca MĂ, Charpentier I, Martiny M, Ferron G (2010) Identification of sheet metal plastic anisotropy using heterogeneous biaxial tensile tests. *Int J Mech Sci* 52:572–580. <https://doi.org/10.1016/j.jimecsci.2009.12.003>
252. Ferron G, Makkouk R, Morreale J (1994) A parametric description of orthotropic plasticity in metal sheets. *Int J Plast* 10:431–449. [https://doi.org/10.1016/0749-6419\(94\)90008-6](https://doi.org/10.1016/0749-6419(94)90008-6)
253. Guélon T, Toussaint E, Le Cam JB, Promma N, Grédiac M (2009) A new characterisation method for rubber. *Polym Test* 28:715–723. <https://doi.org/10.1016/j.polymertesting.2009.06.001>
254. Mooney M (1940) A theory of large elastic deformation. *J Appl Phys* 11:582–592. <https://doi.org/10.1063/1.1712836>
255. He T, Liu L, Makeev A (2018) Uncertainty analysis in composite material properties characterization using digital image correlation and finite element model updating. *Compos Struct* 184:337–351. <https://doi.org/10.1016/j.compstruct.2017.10.009>
256. Gao X, Liu G, Wang L, Yi Y, Lin G, Ma S (2021) Inverse characterisation of gradient distribution of the modulus of bamboo using a four-point bending test. *Holzforschung* 75:626–634. <https://doi.org/10.1515/hf-2020-0155>
257. Liu G, Wang L, Yi Y, Sun L, Shi L, Jiang H, Ma S (2018) Inverse identification of tensile and compressive damage properties of graphite material based on a single four-point bending test. *J Nucl Mater* 509:445–453. <https://doi.org/10.1016/j.jnucmat.2018.07.022>
258. Liu G, Wang L, Yi Y, Sun L, Shi L, Ma S (2019) Inverse identification of graphite damage properties under complex stress states. *Mater Des* 183:108135. <https://doi.org/10.1016/j.matdes.2019.108135>

259. Nigamaa N, Subramanian SJ (2014) Identification of orthotropic elastic constants using the Eigenfunction virtual fields method. *Int J Solids Struct* 51:295–304. <https://doi.org/10.1016/j.ijsolstr.2013.09.021>
260. Barick MC, Gaillard Y, Lejeune A, Amiot F, Richard F (2020) On the uniqueness of intrinsic viscoelastic properties of materials extracted from nanoindentation using FEMU. *Int J Solids Struct* 202:929–946. <https://doi.org/10.1016/j.ijsolstr.2020.03.015>
261. Gebhardt C, Sedlatschek T, Bezold A, Broeckmann C (2021) Full-field inverse identification of elasto-plastic model parameters for ductile cast iron. *Mech Mater* 162:104056. <https://doi.org/10.1016/j.mechmat.2021.104056>
262. Sun G, Xu F, Li G, Huang X, Li Q (2014) Determination of mechanical properties of the weld line by combining micro-indentation with inverse modeling. *Comput Mater Sci* 85:347–362. <https://doi.org/10.1016/j.commatsci.2014.01.006>
263. Satošek R, Pepelnjak T, Starman B (2023) Characterisation of out-of-plane shear behaviour of anisotropic sheet materials based on indentation plastometry. *Int J Mech Sci*. <https://doi.org/10.1016/j.ijmecsci.2023.108403>
264. Pottier T, Vacher P, Toussaint F, Louche H, Coudert T (2012) Out-of-plane testing procedure for inverse identification purpose: application in sheet metal plasticity. *Exp Mech* 52:951–963. <https://doi.org/10.1007/s11340-011-9555-3>
265. Souto N, Thuillier S, Andrade-Campos A (2015) Design of an indicator to characterize and classify mechanical tests for sheet metals. *Int J Mech Sci* 101–102:252–271. <https://doi.org/10.1016/j.ijmecsci.2015.07.026>
266. Jones EMC, Carroll JD, Karlson KN, Kramer SLB, Lehouc RB, Reu PL, Turner DZ (2018) Parameter covariance and non-uniqueness in material model calibration using the virtual fields method. *Comput Mater Sci* 152:268–290. <https://doi.org/10.1016/j.commatsci.2018.05.037>
267. Jones EMC, Carroll JD, Karlson KN, Kramer SLB, Lehouc RB, Reu PL, Turner DZ (2017) Combining full-field measurements and inverse techniques for smart material testing. In: Conference proceedings of the society for experimental mechanics series, pp 37–39. https://doi.org/10.1007/978-3-319-51439-0_9
268. Grédiac M, Pierron F, Surrel Y (1999) Novel procedure for complete in-plane composite characterization using a single T-shaped specimen. *Exp Mech* 39:142–149. <https://doi.org/10.1007/BF02331118>
269. Souto N, Andrade-Campos A, Thuillier S (2017) Mechanical design of a heterogeneous test for material parameters identification. *Int J Mater Form* 10:353–367. <https://doi.org/10.1007/s12289-016-1284-9>
270. Aquino J, Campos AA, Souto N, Thuillier S (2018) Experimental validation of a new heterogeneous mechanical test design. *AIP Conf Proc* 1960. <https://doi.org/10.1063/1.5034928>
271. Conde M, Andrade-Campos A, Oliveira MG, Martins JMP (2021) Design of heterogeneous interior notched specimens for material mechanical characterization. In: ESAFORM 2021—24th international conference on material forming, vol 11, pp 1–13. <https://doi.org/10.25518/esaform21.2502>
272. Sigmund O, Maute K (2013) Topology optimization approaches: a comparative review. *Struct Multidiscip Optim* 48:1031–1055. <https://doi.org/10.1007/s00158-013-0978-6>
273. Almeida F, Barroqueiro B, Dias-De-Oliveira J, Andrade-Campos AG (2020) On the development of a heterogeneous mechanical test specimen using topology optimization. *Procedia Manuf* 47:816–823. <https://doi.org/10.1016/j.promfg.2020.04.256>
274. Barroqueiro B, Andrade-Campos A, Dias-de-Oliveira J, Valente RAF (2020) Design of mechanical heterogeneous specimens using topology optimization. *Int J Mech Sci* 181:105764. <https://doi.org/10.1016/j.ijmecsci.2020.105764>
275. Gonçalves M, Andrade-Campos A, Thuillier S (2022) On the topology design of a mechanical heterogeneous specimen using geometric and material nonlinearities. *IOP Conf Ser Mater Sci Eng* 1238:012055. <https://doi.org/10.1088/1757-899x/1238/1/012055>
276. Gonçalves M, Andrade-Campos A, Thuillier S (2022) On the design of a heterogeneous mechanical test using a nonlinear topology optimization approach. *Key Eng Mater* 926:2228–2237. <https://doi.org/10.4028/p-6rou28>
277. Affagard JS, Wijanto F, Allain JM (2017) Improving the experimental protocol for a more accurate identification of a given mechanical behaviour in a single assay: application to skin. *Strain* 53:1–13. <https://doi.org/10.1111/str.12236>
278. Bos F, Le Magorou L, Rouger F (2005) An approach to viscoelastic behaviour analysis of wood-based panels by an inverse method of characterisation. *Holzforschung* 59:546–551. <https://doi.org/10.1515/HF.2005.090>
279. Le Magorou L, Bos F, Rouger F (2002) Identification of constitutive laws for wood-based panels by means of an inverse method. *Compos Sci Technol* 62:591–596. [https://doi.org/10.1016/S0266-3538\(01\)00149-X](https://doi.org/10.1016/S0266-3538(01)00149-X)
280. Chapelier M, Bouclier R, Passieux JC (2022) Spline-based specimen shape optimization for robust material model calibration. *Adv Model Simul Eng Sci*. <https://doi.org/10.1186/s40323-022-00217-9>
281. Rossi M, Pierron F (2012) On the use of simulated experiments in designing tests for material characterization from full-field measurements. *Int J Solids Struct* 49:420–435. <https://doi.org/10.1016/j.ijsolstr.2011.09.025>
282. Gu X, Pierron F (2016) Towards the design of a new standard for composite stiffness identification. *Composites A* 91:448–460. <https://doi.org/10.1016/j.compositesa.2016.03.026>
283. Comellas E, Valdez SI, Oller S, Botello S (2015) Optimization method for the determination of material parameters in damaged composite structures. *Compos Struct* 122:417–424. <https://doi.org/10.1016/j.compstruct.2014.12.014>
284. Pan B, Qian K, Xie H, Asundi A (2009) Two-dimensional digital image correlation for in-plane displacement and strain measurement: a review. *Meas Sci Technol* 20:062001. <https://doi.org/10.1088/0957-0233/20/6/062001>
285. Yang L, Xie X, Zhu L, Wu S, Wang Y (2014) Review of electronic speckle pattern interferometry (ESPI) for three dimensional displacement measurement. *Chin J Mech Eng (English Edition)* 27:1–13. <https://doi.org/10.3901/CJME.2014.01.001>
286. Ncorr—open source 2D digital image correlation MATLAB software, (n.d.). <http://www.ncorr.com/>
287. dicengine/dice: digital image correlation engine (DICe): a stereo DIC application that runs on Mac, Windows, and Linux, (n.d.). <https://github.com/dicengine/dice>
288. Geod-Geom/py2DIC (n.d.). <https://github.com/Geod-Geom/py2DIC/>
289. Olufsen SN, Andersen ME, Fagerholt E (2020) μ DIC: an open-source toolkit for digital image correlation. *SoftwareX*. <https://doi.org/10.1016/j.softx.2019.100391>
290. vincentjzy/OpenCorr: an open source C++ library for development of digital image correlation and digital volume correlation (n.d.). <https://github.com/vincentjzy/OpenCorr>
291. MultiDIC: an open-source toolbox for multi-view 3D digital image correlation—MIT Media Lab (n.d.). <https://www.media.mit.edu/publications/mul/>
292. Correlated Solutions Digital Image Correlation (n.d.). <https://www.correlatedsolutions.com/>
293. Metrology beyond colors | MatchID | Make metrology count (n.d.). <https://www.matchid.eu/>
294. DIC Software (n.d.). <https://www.lavision.de/en/applications/materials-testing/system-components/dic-software/index.php>

295. ARAMIS 3D testing (n.d.). <https://www.trilion.com/aramis>
296. DIC Elite—3D deformation analysis—image systems (n.d.). <https://imagesystems.se/dic-elite/>
297. Digital Image Correlation (DIC) | 3D Full-Field Measurement (n.d.). <https://www.dantecdynamics.com/solutions/digital-image-correlation-dic/>. Accessed 23 May 2024
298. Digital image correlation Correli STC (n.d.). <https://www.correli-stc.com/>
299. Ben Azzouna M, Feissel P, Villon P (2013) Identification of elastic properties from full-field measurements: a numerical study of the effect of filtering on the identification results. *Meas Sci Technol*. <https://doi.org/10.1088/0957-0233/24/5/055603>
300. Hild F, Roux S (2012) Comparison of local and global approaches to digital image correlation. *Exp Mech* 52:1503–1519. <https://doi.org/10.1007/s11340-012-9603-7>
301. Pierré JE, Passieux JC, Périé JN (2017) Finite element stereo digital image correlation: framework and mechanical regularization. *Exp Mech* 57:443–456. <https://doi.org/10.1007/s11340-016-0246-y>
302. Chen B, Coppieters S (2022) Meshfree digital image correlation using element free galerkin method: theory, algorithm and validation. *Exp Mech*. <https://doi.org/10.1007/s11340-022-00930-x>
303. Chen B, Coppieters S (2023) Unified digital image correlation under meshfree framework. *Strain*. <https://doi.org/10.1111/str.12461>
304. Chen J-S, Hillman M, Chi S-W (2017) Meshfree methods: progress made after 20 years. *J Eng Mech* 143:04017001. [https://doi.org/10.1061/\(asce\)em.1943-7889.0001176](https://doi.org/10.1061/(asce)em.1943-7889.0001176)
305. Reu PL, Blaysat B, Andó E, Bhattacharya K, Couture C, Couty V, Deb D, Fayad SS, Iadicola MA, Jaminion S, Klein M, Landauer AK, Lava P, Liu M, Luan LK, Olufsen SN, Réthoré J, Roubin E, Seidl DT, Siebert T, Stamati O, Toussaint E, Turner D, Vemulapati CSR, Weikert T, Witz JF, Witzel O, Yang J (2022) DIC challenge 2.0: developing images and guidelines for evaluating accuracy and resolution of 2D analyses. *Exp Mech* 62:639–654. <https://doi.org/10.1007/s11340-021-00806-6>
306. de Melo CC, Furlan M, Hild F, Schmitt N, Canto RB (2020) Uniaxial compression test on ceramic green compact with bending consideration using digital image correlation. *Powder Technol* 376:136–148. <https://doi.org/10.1016/j.powtec.2020.08.002>
307. Affagard JS, Mathieu F, Guimard JM, Hild F (2016) Identification method for the mixed mode interlaminar behavior of a thermoset composite using displacement field measurements and load data. *Composites A* 91:238–249. <https://doi.org/10.1016/j.compositesa.2016.10.007>
308. Sutton MA, Yan JH, Tiwari V, Schreier HW, Orteu JJ (2008) The effect of out-of-plane motion on 2D and 3D digital image correlation measurements. *Opt Lasers Eng* 46:746–757. <https://doi.org/10.1016/j.optlaseng.2008.05.005>
309. Tomičević Z, Kodvanj J, Hild F (2016) Characterization of the nonlinear behavior of nodular graphite cast iron via inverse identification: analysis of biaxial tests. *Eur J Mech A* 59:195–209. <https://doi.org/10.1016/j.euromechsol.2016.03.006>
310. Siddiqui MZ, Ahmed MF (2014) An out-of-plane motion compensation strategy for improving material parameter estimation accuracy with 2D field measurements. *Exp Mech* 54:1259–1268. <https://doi.org/10.1007/s11340-014-9880-4>
311. Luo PF, Chao YJ, Sutton MA, Peters WH (1993) Accurate measurement of three-dimensional deformations in deformable and rigid bodies using computer vision. *Exp Mech* 33:123–132. <https://doi.org/10.1007/BF02322488>
312. Yu L, Pan B (2017) Single-camera high-speed stereo-digital image correlation for full-field vibration measurement. *Mech Syst Signal Process* 94:374–383. <https://doi.org/10.1016/j.ymssp.2017.03.008>
313. Richard Hartley AZ (n.d.) Multiple view geometry in computer vision second edition
314. Hartley RI, Sturm P (1997) Triangulation. *Comput Vis Image Underst* 68:146–157. <https://doi.org/10.1006/cviu.1997.0547>
315. Chen B, Pan B (2020) Camera calibration using synthetic random speckle pattern and digital image correlation. *Opt Lasers Eng* 126:105919. <https://doi.org/10.1016/j.optlaseng.2019.105919>
316. Zhang Z (1999) Flexible camera calibration by viewing a plane from unknown orientations. In: Proceedings of the IEEE international conference on computer vision, vol 1, pp 666–673. <https://doi.org/10.1109/iccv.1999.791289>
317. Orteu JJ (2009) 3-D computer vision in experimental mechanics. *Opt Lasers Eng* 47:282–291. <https://doi.org/10.1016/j.optlaseng.2007.11.009>
318. Pan B, Yu LP, Zhang QB (2018) Review of single-camera stereo-digital image correlation techniques for full-field 3D shape and deformation measurement. *Sci China Technol Sci* 61:2–20. <https://doi.org/10.1007/s11431-017-9090-x>
319. Yu L, Pan B (2016) Single-camera stereo-digital image correlation with a four-mirror adapter: optimized design and validation. *Opt Lasers Eng* 87:120–128. <https://doi.org/10.1016/j.optlaseng.2016.03.014>
320. Chen B, Pan B (2019) Calibration-free single camera stereo-digital image correlation for small-scale underwater deformation measurement. *Opt Express* 27:10509. <https://doi.org/10.1364/oe.27.010509>
321. Siebert T (2007) High-speed digital image correlation: error estimations and applications. *Opt Eng* 46:051004. <https://doi.org/10.1117/1.2741217>
322. Orteu JJ, Bugarin F, Harvent J, Robert L, Velay V (2011) Multiple-camera instrumentation of a single point incremental forming process pilot for shape and 3D displacement measurements: methodology and results. *Exp Mech* 51:625–639. <https://doi.org/10.1007/s11340-010-9436-1>
323. Wang Y, Lava P, Coppieters S, Houtte PV, Debruyne D (2013) Application of a multi-camera stereo DIC set-up to assess strain fields in an Erichsen test: Methodology and validation. *Strain* 49:190–198. <https://doi.org/10.1111/str.12027>
324. Chen B, Pan B (2022) Mirror-assisted multi-view digital image correlation: principles, applications and implementations. *Opt Lasers Eng* 149:106786. <https://doi.org/10.1016/j.optlaseng.2021.106786>
325. Chen B, Pan B (2019) Mirror-assisted panoramic-digital image correlation for full-surface 360-deg deformation measurement. *Measurement (Lond)* 132:350–358. <https://doi.org/10.1016/j.measurement.2018.09.046>
326. Chen B, Pan B (2021) Measuring true stress–strain curves of cylindrical bar samples with mirror-assisted multi-view digital image correlation. *Strain*. <https://doi.org/10.1111/str.12403>
327. Chen B, Genovese K, Pan B (2020) In vivo panoramic human skin shape and deformation measurement using mirror-assisted multi-view digital image correlation. *J Mech Behav Biomed Mater* 110:103936. <https://doi.org/10.1016/j.jmbbm.2020.103936>
328. Garemark J, Perea-Buceta JE, Felhofer M, Chen B, Cortes Ruiz MF, Sapouna I, Gierlinger N, Kilpeläinen IA, Berglund LA, Li Y (2023) Strong shape-memory lignocellulosic aerogel via wood cell wall nanoscale reassembly. *ACS Nano* 17:4775–4789. <https://doi.org/10.1021/acsnano.2c11220>
329. Pan B, Chen B (2019) A novel mirror-assisted multi-view digital image correlation for dual-surface shape and deformation measurements of sheet samples. *Opt Lasers Eng* 121:512–520. <https://doi.org/10.1016/j.optlaseng.2019.05.016>
330. Chen B, Pan B (2019) Through-thickness strain field measurement using the mirror-assisted multi-view digital image

- correlation. *Mech Mater* 137:103104. <https://doi.org/10.1016/j.mechmat.2019.103104>
331. Bay BK, Smith TS, Fyhrie DP, Saad M (1999) Digital volume correlation: three-dimensional strain mapping using X-ray tomography. *Exp Mech* 39:217–226. <https://doi.org/10.1007/BF02323555>
 332. Benoit A, Guérard S, Gillet B, Guillot G, Hild F, Mitton D, Périé JN, Roux S (2009) 3D analysis from micro-MRI during in situ compression on cancellous bone. *J Biomech* 42:2381–2386. <https://doi.org/10.1016/j.jbiomech.2009.06.034>
 333. Wang T, Jiang Z, Kemao Q, Lin F, Soon SH (2016) GPU accelerated digital volume correlation. *Exp Mech* 56:297–309. <https://doi.org/10.1007/s11340-015-0091-4>
 334. El Hachem C, Abahri K, Bennacer R (2019) Original experimental and numerical approach for prediction of the microscopic hygro-mechanical behavior of spruce wood. *Constr Build Mater* 203:258–266. <https://doi.org/10.1016/j.conbuildmat.2019.01.107>
 335. Chen H, Shen J, Scotson D, Jin X, Wu H, Marrow TJ (2023) Fracture toughness evaluation of a nuclear graphite with non-linear elastic properties by 3D imaging and inverse finite element analysis. *Eng Fract Mech* 293:109719. <https://doi.org/10.1016/j.engfracmech.2023.109719>
 336. Buljac A, Trejo Navas VM, Shakoov M, Bouterf A, Neggers J, Bernacki M, Bouchard PO, Morgeneyer TF, Hild F (2018) On the calibration of elastoplastic parameters at the microscale via X-ray microtomography and digital volume correlation for the simulation of ductile damage. *Eur J Mech A* 72:287–297. <https://doi.org/10.1016/j.euromechsol.2018.04.010>
 337. Shafiei Dizaji M, Alipour M, Harris DK (2018) Leveraging full-field measurement from 3D digital image correlation for structural identification. *Exp Mech* 58:1049–1066. <https://doi.org/10.1007/s11340-018-0401-8>
 338. Yu L, Pan B (2017) Full-frame, high-speed 3D shape and deformation measurements using stereo-digital image correlation and a single color high-speed camera. *Opt Lasers Eng* 95:17–25. <https://doi.org/10.1016/j.optlaseng.2017.03.009>
 339. Bebernis TJ, Ehrhardt DA (2017) High-speed 3D digital image correlation vibration measurement: recent advancements and noted limitations. *Mech Syst Signal Process* 86:35–48. <https://doi.org/10.1016/j.ymsp.2016.04.014>
 340. Chang YH, Wang W, Siebert T, Chang JY, Mottershead JE (2019) Basis-updating for data compression of displacement maps from dynamic DIC measurements. *Mech Syst Signal Process* 115:405–417. <https://doi.org/10.1016/j.ymsp.2018.05.058>
 341. Kajberg J, Wikman B (2007) Viscoplastic parameter estimation by high strain-rate experiments and inverse modelling—Speckle measurements and high-speed photography. *Int J Solids Struct* 44:145–164. <https://doi.org/10.1016/j.ijsolstr.2006.04.018>
 342. Janin A, Constantinescu A, Weisz-Patrault D, Nevieré R, Stackler M, Albouy W (2019) Identification of the material behavior of adhesive joints under dynamic multiaxial loadings. *Int J Impact Eng* 133:103355. <https://doi.org/10.1016/j.ijimpeng.2019.103355>
 343. Spranghers K, Vasilakos I, Lecompte D, Sol H, Vantomme J (2014) Identification of the plastic behavior of aluminum plates under free air explosions using inverse methods and full-field measurements. *Int J Solids Struct* 51:210–226. <https://doi.org/10.1016/j.ijsolstr.2013.09.027>
 344. Corallo L, Mirone G, Verleysen P (2023) A novel high-speed bulge test to identify the large deformation behavior of sheet metals. *Exp Mech* 63:593–607. <https://doi.org/10.1007/s11340-022-00936-5>
 345. Bing P, Xia DWY (2012) Incremental calculation for large deformation measurement using reliability-guided digital image correlation. *Opt Lasers Eng* 50:586–592. <https://doi.org/10.1016/j.optlaseng.2011.05.005>
 346. Dong Y, Kakisawa H, Kagawa Y (2014) Optical system for microscopic observation and strain measurement at high temperature. *Meas Sci Technol*. <https://doi.org/10.1088/0957-0233/25/2/025002>
 347. Pan B, Wu D, Wang Z, Xia Y (2011) High-temperature digital image correlation method for full-field deformation measurement at 1200 °C. *Meas Sci Technol* 22:015701. <https://doi.org/10.1088/0957-0233/22/1/015701>
 348. Guo X, Liang J, Tang Z, Cao B, Yu M (2014) High-temperature digital image correlation method for full-field deformation measurement captured with filters at 2600°C using spraying to form speckle patterns. *Opt Eng* 53:063101. <https://doi.org/10.1117/1.oe.53.6.063101>
 349. Yu L, Pan B (2023) Image-based deformation measurement of aerodynamic heating surfaces using time-gated active imaging digital image correlation. *Exp Mech* 63:655–663. <https://doi.org/10.1007/s11340-023-00943-0>
 350. Yu L, Pan B (2022) Time-gated active imaging digital image correlation for deformation measurement at high temperatures. *Extreme Mech Lett* 54:101767. <https://doi.org/10.1016/j.eml.2022.101767>
 351. Liu J, Chen X, Du K, Zhou X, Xiang N, Osaka A (2020) A modified Bonora damage model for temperature and strain rate-dependent materials in hot forging process. *Eng Fract Mech* 235:107107. <https://doi.org/10.1016/j.engfracmech.2020.107107>
 352. Bertin M, Du C, Hoefnagels JPM, Hild F (2016) Crystal plasticity parameter identification with 3D measurements and integrated digital image correlation. *Acta Mater* 116:321–331. <https://doi.org/10.1016/j.actamat.2016.06.039>
 353. Hassan GM (2021) Deformation measurement in the presence of discontinuities with digital image correlation: a review. *Opt Lasers Eng*. <https://doi.org/10.1016/j.optlaseng.2020.106394>
 354. Poissant J, Barthelat F (2010) A novel “subset splitting” procedure for digital image correlation on discontinuous displacement fields. *Exp Mech* 50:353–364. <https://doi.org/10.1007/s11340-009-9220-2>
 355. Réthoré J, Hild F, Roux S (2007) Shear-band capturing using a multiscale extended digital image correlation technique. *Comput Methods Appl Mech Eng* 196:5016–5030. <https://doi.org/10.1016/j.cma.2007.06.019>
 356. Chen B, Coppieters S, Jungstedt E (2023) Element-removal global digital image correlation for accurate discontinuous deformation field measurement in fracture mechanics. *Eng Fract Mech* 290:109493. <https://doi.org/10.1016/j.engfracmech.2023.109493>
 357. Avril S, Pierron F, Pannier Y, Rotinat R (2008) Stress reconstruction and constitutive parameter identification in plane-stress elasto-plastic problems using surface measurements of deformation fields. *Exp Mech* 48:403–419. <https://doi.org/10.1007/s11340-007-9084-2>
 358. Gogu C, Yin W, Haftka R, Ifju P, Molimard J, Le Riche R, Vautrin A (2013) Bayesian identification of elastic constants in multi-directional laminate from moiré interferometry displacement fields. *Exp Mech* 53:635–648. <https://doi.org/10.1007/s11340-012-9671-8>
 359. Lecompte D, Sol H, Vantomme J, Habraken AM (2005) Identification of elastic orthotropic material parameters based on ESPI measurements. In: Proceedings of the 2005 SEM annual conference and exposition on experimental and applied mechanics, pp 1055–1062
 360. Rokoš O, Hoefnagels JPM, Peerlings RHJ, Geers MGD (2018) On micromechanical parameter identification with integrated DIC and the role of accuracy in kinematic boundary conditions. *Int J Solids Struct* 146:241–259. <https://doi.org/10.1016/j.ijsolstr.2018.04.004>
 361. Zaplatić A, Vrgoč A, Tomičević Z, Hild F (2023) Boundary condition effect on the evaluation of stress triaxiality fields.

- Int J Mech Sci 246:108127. <https://doi.org/10.1016/j.ijmecsci.2023.108127>
362. Kowalewski M (2019) Gajewski, assessment of optimization methods used to determine plasticity parameters based on DIC and back calculation methods. *Exp Tech* 43:385–396. <https://doi.org/10.1007/s40799-018-00298-5>
363. Gerbig D, Bower A, Savic V, Hector LG (2016) Coupling digital image correlation and finite element analysis to determine constitutive parameters in necking tensile specimens. *Int J Solids Struct* 97–98:496–509. <https://doi.org/10.1016/j.ijsolstr.2016.06.038>
364. Holmes J, Sommacal S, Das R, Stachurski Z, Compston P (2023) Digital image and volume correlation for deformation and damage characterisation of fibre-reinforced composites: a review. *Compos Struct* 315:116994. <https://doi.org/10.1016/j.composit.2023.116994>
365. Touzeau C, Magnain B, Emile B, Laurent H, Florentin E (2016) Identification in transient dynamics using a geometry-based cost function in finite element model updating method. *Finite Elem Anal Des* 122:49–60. <https://doi.org/10.1016/j.finel.2016.09.003>
366. Lin Q, Sun C, Chen J (2022) Inverse method for the reconstruction of contact stress in point contact with surface profile measurement. *Meas Sci Technol*. <https://doi.org/10.1088/1361-6501/ac6b18>
367. Roux S, Hild F (2020) Optimal procedure for the identification of constitutive parameters from experimentally measured displacement fields. *Int J Solids Struct* 184:14–23. <https://doi.org/10.1016/j.ijsolstr.2018.11.008>
368. Cao J, Lin J (2008) A study on formulation of objective functions for determining material models. *Int J Mech Sci* 50:193–204. <https://doi.org/10.1016/j.ijmecsci.2007.07.003>
369. Andrade-Campos A, De-Carvalho R, Valente RAF (2012) Novel criteria for determination of material model parameters. *Int J Mech Sci* 54:294–305. <https://doi.org/10.1016/j.ijmecsci.2011.11.010>
370. Abedini A, Butcher C, Rahmaan T, Worswick MJ (2018) Evaluation and calibration of anisotropic yield criteria in shear loading: constraints to eliminate numerical artefacts. *Int J Solids Struct* 151:118–134. <https://doi.org/10.1016/j.ijsolstr.2017.06.029>
371. Yue ZM, Soyarslan C, Badreddine H, Saanouni K, Tekkaya AE (2013) Inverse identification of CDM model parameters for DP1000 steel sheets using a hybrid experimental-numerical methodology spanning various stress triaxiality ratios. *Key Eng Mater* 554–557:2103–2110. <https://doi.org/10.4028/www.scientific.net/KEM.554-557.2103>
372. Lisiecka-Graca P, Majta J, Muszka K (2020) Full-field strain measurement and numerical analysis of a microalloyed steel subjected to deformation with strain path change. *Materials* 13:1–10. <https://doi.org/10.3390/ma13235543>
373. Gajewski T, Garbowski T (2014) Calibration of concrete parameters based on digital image correlation and inverse analysis. *Arch Civ Mech Eng* 14:170–180. <https://doi.org/10.1016/j.acme.2013.05.012>
374. Khaloo A, Amirahmadi A (2023) Performance assessment of steel cantilever beams based on connection behaviour using DIC technique and improved hybrid PSO algorithm. *Struct Health Monit*. <https://doi.org/10.1177/14759217231163257>
375. Robert L, Passieux JC, Bugarin F, David C, Périé JN (2015) Multiscale FE-based DIC for enhanced measurements and constitutive parameter identification. In: Conference proceedings of the society for experimental mechanics series 3B, pp 265–275. https://doi.org/10.1007/978-3-319-06986-9_30
376. Simoncelli E (1999) Bayesian multi-scale differential optical flow. In: Jahne B, Haussecker H, Geissler P (eds) *Handbook of computer vision and applications*. Academic Press, Cambridge, pp 397–422
377. Oliveira MG, Martins JMP, Coelho B, Thuillier S, Andrade-Campos A (2021) On the optimisation efficiency for the inverse identification of constitutive model parameters. In: ESAFORM 2021—24th international conference on material forming, vol 11, pp 1–13. <https://doi.org/10.25518/esaform21.1486>
378. Martins JMP, Thuillier S, Andrade-Campos A (2018) Identification of material parameters for plasticity models: a comparative study on the finite element model updating and the virtual fields method. *AIP Conf Proc*. <https://doi.org/10.1063/1.5034964>
379. Rahmani B, Mortazavi F, Villemure I, Levesque M (2013) A new approach to inverse identification of mechanical properties of composite materials: regularized model updating. *Compos Struct* 105:116–1125. <https://doi.org/10.1016/j.compstruct.2013.04.025>
380. Shen B, Paulino GH (2011) Identification of cohesive zone model and elastic parameters of fiber-reinforced cementitious composites using digital image correlation and a hybrid inverse technique. *Cem Concr Compos* 33:572–585. <https://doi.org/10.1016/j.cemconcomp.2011.01.005>
381. Cooreman S, Lecompte D, Sol H, Vantomme J, Debruyne D (2007) Elasto-plastic material parameter identification by inverse methods: calculation of the sensitivity matrix. *Int J Solids Struct* 44:4329–4341. <https://doi.org/10.1016/j.ijsolstr.2006.11.024>
382. Jiang H, Man Z, Guo Z, Feng W, Yang Z, Lei Z, Bai R, Yan S, Cheng B (2024) Determination of residual stress field in laser cladding using finite element updating method driven by contour deformation. *Opt Laser Technol* 179:111371. <https://doi.org/10.1016/j.optlastec.2024.111371>
383. Prime MB (2001) Cross-sectional mapping of residual stresses by measuring the surface contour after a cut. *J Eng Mater Technol* 123:162–168. <https://doi.org/10.1115/1.1345526>
384. Mahnen R, Stein E (1996) Parameter identification for viscoplastic models based on analytical derivatives of a least-squares functional and stability investigations. *Int J Plast* 12:451–479. [https://doi.org/10.1016/S0749-6419\(95\)00016-X](https://doi.org/10.1016/S0749-6419(95)00016-X)
385. Miehe C (1996) Numerical computation of algorithmic (consistent) tangent moduli in large-strain computational inelasticity. *Comput Methods Appl Mech Eng* 134:223–240. [https://doi.org/10.1016/0045-7825\(96\)01019-5](https://doi.org/10.1016/0045-7825(96)01019-5)
386. Tayeb A, Di Cesare N, Lu Y, Sales L, Bastos G, Le Cam JB (2023) Identifying simultaneously hyper-viscoelastic parameters from a unique heterogenous relaxation test: application to engineering elastomeric materials. *Meccanica* 58:1983–2002. <https://doi.org/10.1007/s11012-023-01706-w>
387. Morris MD (1991) Factorial sampling plans for preliminary computational experiments. *Technometrics* 33:161–174. <https://doi.org/10.1080/00401706.1991.10484804>
388. Arora J (2012) *Introduction to optimum design*. Elsevier, Oxford. <https://doi.org/10.1016/C2009-0-61700-1>
389. Trefethen LN, Bau D (2022) *Numerical linear algebra*. SIAM
390. Brun R, Reichert P, Künsch HR (2001) Practical identifiability analysis of large environmental simulation models. *Water Resour Res* 37:1015–1030. <https://doi.org/10.1029/2000WR900350>
391. Sobol' IM (2001) Global sensitivity indices for nonlinear mathematical models and their Monte Carlo estimates. *Math Comput Simul* 55:271–280. [https://doi.org/10.1016/S0378-4754\(00\)00270-6](https://doi.org/10.1016/S0378-4754(00)00270-6)
392. Pereira AFG, Oliveira MC, Fernandes JV, Prates PA (2022) Variance-based sensitivity analysis of the biaxial test on a cruciform specimen. *Key Eng Mater* 926:2154–2161. <https://doi.org/10.4028/p-8med4s>
393. Li X, Lubineau G (2022) Learning from global sensitivity analysis about identification of adhesion properties between an elastoplastic film and a rigid substrate. *Int J Solids Struct* 254–255:111845. <https://doi.org/10.1016/j.ijsolstr.2022.111845>

394. Saltelli A, Annoni P, Azzini I, Campolongo F, Ratto M, Tarantola S (2010) Variance based sensitivity analysis of model output. Design and estimator for the total sensitivity index. *Comput Phys Commun* 181:259–270. <https://doi.org/10.1016/j.cpc.2009.09.018>
395. Fehervary H, Vastmans J, Vander Sloten J, Famaey N (2018) How important is sample alignment in planar biaxial testing of anisotropic soft biological tissues? A finite element study. *J Mech Behav Biomed Mater* 88:201–216. <https://doi.org/10.1016/j.jmbbm.2018.06.024>
396. Bruno L, Furguele FM, Pagnotta L, Poggialini A (2002) A full-field approach for the elastic characterization of anisotropic materials. *Opt Lasers Eng* 37:417–431. [https://doi.org/10.1016/S0143-8166\(01\)00120-8](https://doi.org/10.1016/S0143-8166(01)00120-8)
397. Besl PJ, McKay ND (1992) A method for registration of 3-D shapes. *IEEE Trans Pattern Anal Mach Intell* 14:239–256. <https://doi.org/10.1109/34.121791>
398. Eggert DW, Lorusso A, Fisher RB (1997) Estimating 3-D rigid body transformations: a comparison of four major algorithms. *Mach Vis Appl* 9:272–290. <https://doi.org/10.1007/s001380050048>
399. Wang W, Mottershead JE, Sebastian CM, Patterson EA, Siebert T, Ihle A, Pipino A (2011) Image analysis for full-field displacement/strain data: method and applications. *Appl Mech Mater* 70:39–44. <https://doi.org/10.4028/www.scientific.net/AMM.70.39>
400. Sebastian C, Hack E, Patterson E (2013) An approach to the validation of computational solid mechanics models for strain analysis. *J Strain Anal Eng Des* 48:36–47. <https://doi.org/10.1177/0309324712453409>
401. Chong EKP, Žak SH (2008) An introduction to optimization. Wiley, Hoboken. <https://doi.org/10.1002/9781118033340>
402. Raviolo D, Civera M, Zanotti Fragonara L (2023) A comparative analysis of optimization algorithms for finite element model updating on numerical and experimental benchmarks. *Buildings* 13:3010. <https://doi.org/10.3390/buildings13123010>
403. Negggers J, Mathieu F, Roux S, Hild F (2017) Reducing full-field identification cost by using quasi-newton methods. Conference proceedings of the society for experimental mechanics series 9:135–140. https://doi.org/10.1007/978-3-319-42255-8_18
404. Zhao X, Sun Y, Mei Y (2019) A size-dependent cost function to solve the inverse elasticity problem. *Appl Sci (Switzerland)*. <https://doi.org/10.3390/app9091799>
405. Barton RR, Ivey JS (1996) Nelder-Mead simplex modifications for simulation optimization. *Manage Sci* 42:954–973. <https://doi.org/10.1287/mnsc.42.7.954>
406. Nelder JA, Mead R (1965) A simplex method for function minimization. *Comput J* 7:308–313. <https://doi.org/10.1093/comjnl/7.4.308>
407. Holland JH (1992) Genetic algorithms. *Sci Am* 267:66–72. <https://doi.org/10.1038/scientificamerican0792-66>
408. Vijayanand VD, Mokhtarishirazabad M, Peng J, Wang Y, Gorley M, Knowles DM, Mostafavi M (2020) A novel methodology for estimating tensile properties in a small punch test employing in-situ DIC based deflection mapping. *J Nucl Mater* 538:152260. <https://doi.org/10.1016/j.jnucmat.2020.152260>
409. Genovese K, Lamberti L, Pappalettere C (2004) A new hybrid technique for in-plane characterization of orthotropic materials. *Exp Mech* 44:584–592. <https://doi.org/10.1177/0014485104048907>
410. Cosola E, Genovese K, Lamberti L, Pappalettere C (2008) A general framework for identification of hyper-elastic membranes with moiré techniques and multi-point simulated annealing. *Int J Solids Struct* 45:6074–6099. <https://doi.org/10.1016/j.ijsolstr.2008.07.019>
411. Kennedy J, Eberhart R (2023) Particle swarm optimization. In: *Proceedings of ICNN'95—international conference on neural networks*, IEEE, pp 1942–1948. <https://doi.org/10.1109/ICNN.1995.488968>
412. Bresolin FL, Vassoler JM (2020) A numerical study of the constitutive characterization of thermoplastic materials submitted to finite strain. *Int J Solids Struct* 206:456–471. <https://doi.org/10.1016/j.ijsolstr.2020.09.018>
413. Cocchetti G, Mahini MR, Maier G (2014) Mechanical characterization of foils with compression in their planes. *Mech Adv Mater Struct* 21:853–870. <https://doi.org/10.1080/15376494.2012.726398>
414. Endelt B, Nielsen KB (2004) Inverse modeling based on an analytical definition of the Jacobian matrix associated with Hill's 48 yield criterion, pp 1–4
415. Zhang B, Endelt B, Lang L, Nielsen KB (2021) Identification of constitutive parameters for thin-walled aluminium tubes using a hybrid strategy. *Mater Today Commun* 28:102670. <https://doi.org/10.1016/j.mtcomm.2021.102670>
416. Schemmann M, Brylka B, Miller V, Kehrer ML, Bhlke T (2015) Mean field homogenization of discontinuous fiber reinforced polymers and parameter identification of biaxial tensile tests through inverse modeling. In: *ICCM international conferences on composite materials 2015-July*, pp 19–24
417. Oberai AA, Gokhale NH, Feijóo GR (2003) Solution of inverse problems in elasticity imaging using the adjoint method. *Inverse Probl* 19:297–313. <https://doi.org/10.1088/0266-5611/19/2/304>
418. Considine JM, Vahey DW, Matthys D, Rowlands RE, Turner KT (2012) An inverse method for analyzing defects in heterogeneous materials. In: *Conference proceedings of the society for experimental mechanics series 4*, pp 339–346. https://doi.org/10.1007/978-1-4419-9796-8_44
419. Meng Q, Wang TJ (2019) Mechanics of strong and tough cellulose nanopaper. *Appl Mech Rev* 71:1–30. <https://doi.org/10.1115/1.4044018>
420. Wu J, Yang X, Song Y, Sun Q, Pei Y (2022) Study on a new inversion method for non-uniform distribution of rock material parameters. *Bull Eng Geol Environ*. <https://doi.org/10.1007/s10064-022-02760-6>
421. Borzeszkowski B, Lubowiecka I, Sauer RA (2022) Nonlinear material identification of heterogeneous isogeometric Kirchhoff-Love shells. *Comput Methods Appl Mech Eng* 390:114442. <https://doi.org/10.1016/j.cma.2021.114442>
422. Yin Y, Liu G, Zhao T, Ma Q, Wang L, Zhang Y (2022) Inversion method of the young's modulus field and Poisson's ratio field for rock and its test application. *Materials*. <https://doi.org/10.3390/ma15155463>
423. Kowalczyk P (2019) Identification of mechanical parameters of composites in tensile tests using mixed numerical-experimental method. *Measurement (Lond)* 135:131–137. <https://doi.org/10.1016/j.measurement.2018.11.027>
424. Witz JF, Roux S, Hild F, Rieunier JB (2008) Mechanical properties of crimped mineral wools: identification from digital image correlation. *J Eng Mater Technol* 130:0210161–0210167. <https://doi.org/10.1115/1.2884575>
425. Schulte R, Karca C, Ostwald R, Menzel A (2023) Machine learning-assisted parameter identification for constitutive models based on concatenated loading path sequences. *Eur J Mech A* 98:104854. <https://doi.org/10.1016/j.euromechsol.2022.104854>
426. Andrade-Campos A, Thuillier S, Pilvin P, Teixeira-Dias F (2007) On the determination of material parameters for internal variable thermoelastic-viscoplastic constitutive models. *Int J Plast* 23:1349–1379. <https://doi.org/10.1016/j.ijplas.2006.09.002>
427. Sun C, Lin QL, Chen JB (2022) An inverse identification method for the characterization of elastic conforming contact behavior

- during flat punch indentation. *Exp Mech* 62:745–759. <https://doi.org/10.1007/s11340-021-00811-9>
428. Ruybalid AP, Hoefnagels JPM, van der Sluis O, Geers MGD (2018) Image-based interface characterization with a restricted microscopic field of view. *Int J Solids Struct* 132–133:218–231. <https://doi.org/10.1016/j.ijsolstr.2017.08.020>
429. Cox MG, Siebert BRL (2006) The use of a Monte Carlo method for evaluating uncertainty and expanded uncertainty. *Metrologia*. <https://doi.org/10.1088/0026-1394/43/4/S03>
430. Kroese DP, Brereton T, Taimre T, Botev ZI (2014) Why the Monte Carlo method is so important today. *Wiley Interdiscip Rev Comput Stat* 6:386–392. <https://doi.org/10.1002/wics.1314>
431. Zhao J, Pan B (2023) Uncertainty quantification for 3D digital image correlation displacement measurements using Monte Carlo method. *Opt Lasers Eng* 170:107777. <https://doi.org/10.1016/j.optlaseng.2023.107777>
432. Vlaeyen M, Haitjema H, Dewulf W (2021) Digital twin of an optical measurement system. *Sensors*. <https://doi.org/10.3390/s21196638>
433. Hu Y, Yang Q, Sun X (2012) Design, implementation, and testing of advanced virtual coordinate-measuring machines. *IEEE Trans Instrum Meas* 61:1368–1376. <https://doi.org/10.1109/TIM.2011.2175828>
434. Fouque R, Bouclier R, Passieux J-C, Périé J-N (2022) Photometric DIC: a unified framework for global Stereo digital image correlation based on the construction of textured digital twins. *J Theor Comput Appl Mech*. <https://doi.org/10.46298/jtcam.7467>
435. Wang B, Ke X, Song Z, Du K, Bi X, Hao P, Zhou C (2024) An improved strain field reconstruction method based on digital twin for test monitoring. *Exp Mech* 64:519–537. <https://doi.org/10.1007/s11340-024-01035-3>
436. Schreier HW, Sutton MA (2002) Systematic errors in digital image correlation due to undermatched subset shape functions. *Exp Mech* 42:303–310. <https://doi.org/10.1177/001448502321548391>
437. Pan B, Yu L, Wu D (2013) High-accuracy 2D digital image correlation measurements with bilateral telecentric lenses: error analysis and experimental verification. *Proc Soc Exp Mech*. <https://doi.org/10.1007/s11340-013-9774-x>
438. Pan B, Xie H, Wang Z, Qian K, Wang Z (2008) Study on subset size selection in digital image correlation for speckle patterns. *Opt Express* 16:7037. <https://doi.org/10.1364/oe.16.007037>
439. Park J, Yoon S, Kwon TH, Park K (2017) Assessment of speckle-pattern quality in digital image correlation based on gray intensity and speckle morphology. *Opt Lasers Eng* 91:62–72. <https://doi.org/10.1016/j.optlaseng.2016.11.001>
440. Reu PL (2013) A study of the influence of calibration uncertainty on the global uncertainty for digital image correlation using a Monte Carlo approach. *Exp Mech* 53:1661–1680. <https://doi.org/10.1007/s11340-013-9746-1>
441. Marek A, Davis FM, Pierron F (2017) Sensitivity-based virtual fields for the non-linear virtual fields method. *Comput Mech* 60:409–431. <https://doi.org/10.1007/s00466-017-1411-6>
442. Maček A, Starman B, Coppieters S, Urevc J, Halilović M (2024) Confidence intervals of inversely identified material model parameters: a novel two-stage error propagation model based on stereo DIC system uncertainty. *Opt Lasers Eng*. <https://doi.org/10.1016/j.optlaseng.2023.107958>
443. Li Y, Vasileva E, Sychugov I, Popov S, Berglund L (2018) Optically transparent wood: recent progress, opportunities, and challenges. *Adv Opt Mater*. <https://doi.org/10.1002/adom.201800059>
444. Lahti J, Dauer M, Keller DS, Hirn U (2020) Identifying the weak spots in packaging paper: local variations in grammage, fiber orientation and density and the resulting local strain and failure under load. *Cellulose* 27:10327–10343. <https://doi.org/10.1007/s10570-020-03493-z>
445. Zhang Y, Guo L, Brousse CJA, Lee CH, Azoug A, Lu H, Wang S (2022) Machine learning based inverse modeling of full-field strain distribution for mechanical characterization of a linear elastic and heterogeneous membrane. *Mech Mater* 165:104134. <https://doi.org/10.1016/j.mechmat.2021.104134>
446. Tao F, Zhang H, Liu A, Nee AYC (2019) Digital twin in industry: state-of-the-art. *IEEE Trans Ind Inform* 15:2405–2415. <https://doi.org/10.1109/TII.2018.2873186>
447. Guo Z, Bai R, Lei Z, Jiang H, Liu D, Zou J, Yan C (2021) CPINet: parameter identification of path-dependent constitutive model with automatic denoising based on CNN-LSTM. *Eur J Mech A* 90:104327. <https://doi.org/10.1016/j.euromechsol.2021.104327>
448. Karadogan C, Cyron P, Liewald M (2021) Potential use of machine learning to determine yield locus parameters. *IOP Conf Ser Mater Sci Eng* 1157:012064. <https://doi.org/10.1088/1757-899x/1157/1/012064>
449. Lourenço R, Andrade-Campos A, Georgieva P (2022) The use of machine-learning techniques in material constitutive modelling for metal forming processes. *Metals (Basel)* 12:427. <https://doi.org/10.3390/met12030427>
450. Hamel CM, Long KN, Kramer SLB (2023) Calibrating constitutive models with full-field data via physics informed neural networks. *Strain* 59:1–31. <https://doi.org/10.1111/str.12431>
451. Meißner P, Hoppe T, Vietor T (2022) Comparative study of various neural network types for direct inverse material parameter identification in numerical simulations. *Appl Sci*. <https://doi.org/10.3390/app122412793>
452. Wei Y, Serra Q, Lubineau G, Florentin E (2023) Coupling physics-informed neural networks and constitutive relation error concept to solve a parameter identification problem. *Comput Struct* 283:107054. <https://doi.org/10.1016/j.compstruc.2023.107054>
453. Wang L, Liu G, Sun L, Shi L, Ma S (2023) A novel deep-learning-based objective function for inverse identification of material properties. *J Nucl Mater* 584:154579. <https://doi.org/10.1016/j.jnucmat.2023.154579>
454. Jin H, Zhang E, Espinosa HD (2023) Recent advances and applications of machine learning in experimental solid mechanics: a review. *Appl Mech Rev* 75:1–24. <https://doi.org/10.1115/1.4062966>
455. Liu X, Tian S, Tao F, Yu W (2021) A review of artificial neural networks in the constitutive modeling of composite materials. *Composites B* 224:109152. <https://doi.org/10.1016/j.compositesb.2021.109152>
456. Liang L, Liu M, Martin C, Sun W (2018) A deep learning approach to estimate stress distribution: a fast and accurate surrogate of finite-element analysis. *J R Soc Interface*. <https://doi.org/10.1098/rsif.2017.0844>
457. Nath D, Ankit R, Neog DR, Gautam SS (2024) Application of machine learning and deep learning in finite element analysis: a comprehensive review. *Arch Comput Methods Eng*. <https://doi.org/10.1007/s11831-024-10063-0>
458. Khalfallah A, Khalfallah A, Benzarti Z (2024) Identification of elastoplastic constitutive model of gan thin films using instrumented nanoindentation and machine learning technique. *Coatings* 14:683. <https://doi.org/10.3390/coatings14060683>
459. Munoz-Sánchez A, González-Farías IM, Soldani X, Miguélez MH (2011) Hybrid FE/ANN and LPR approach for the inverse identification of material parameters from cutting tests. *Int J Adv Manuf Technol* 54:21–33. <https://doi.org/10.1007/s00170-010-2922-x>
460. Wang M, Zhang G, Liu T, Wang W (2023) Determination of elastoplastic properties of 2024 aluminum alloy using deep learning and instrumented nanoindentation experiment. *Acta Mech Solida Sin* 36:327–339. <https://doi.org/10.1007/s10338-023-00382-3>

461. Halamka J, Bartošák M (2024) Use of machine learning in determining the parameters of viscoplastic models. *Eng Comput* (Swansea). <https://doi.org/10.1108/EC-02-2024-0166>
462. Liu Y, Chen Y, Ding B (2022) Deep learning in frequency domain for inverse identification of nonhomogeneous material properties. *J Mech Phys Solids* 168:105043. <https://doi.org/10.1016/j.jmps.2022.105043>
463. Liu Y, Mei Y, Chen Y, Ding B (2024) Resolving engineering challenges: deep learning in frequency domain for 3D inverse identification of heterogeneous composite properties. *Composites B* 276:111353. <https://doi.org/10.1016/j.compositesb.2024.111353>
464. Cruz DJ, Barbosa MR, Santos AD, Amaral RL, de Sa JC, Fernandes JV (2024) Recurrent neural networks and three-point bending test on the identification of material hardening parameters. *Metals (Basel)* 14:1–33. <https://doi.org/10.3390/met14010084>
465. Hou J, Lu X, Zhang K, Jing Y, Zhang Z, You J, Li Q (2022) Parameters identification of rubber-like hyperelastic material based on general regression neural network. *Materials* 15:1–15. <https://doi.org/10.3390/ma15113776>
466. Shen JJ, Zhou JM, Lu S, Hou YY, Xu RQ (2023) Extraction of hyper-elastic material parameters using BLSTM neural network from instrumented indentation. *J Mech Sci Technol* 37:6589–6599. <https://doi.org/10.1007/s12206-023-1130-1>

Publisher's Note Springer Nature remains neutral with regard to jurisdictional claims in published maps and institutional affiliations.